CONF-9305134

Proceedings of the

ELEVENTH SYMPOSIUM ON ENERGY ENGINEERING SCIENCES

Solid Mechanics and Processing: Analysis, Measurement and Characterization

May 3-5, 1993

at

ARGONNE NATIONAL LABORATORY

Argonne, Illinois

Cosponsored by

Office of Basic Energy Sciences
U. S. DEPARTMENT OF ENERGY

and

Energy Technology Division
ARGONNE NATIONAL LABORATORY

Coordinated by

Argonne National Laboratory
9700 South Cass Avenue
Argonne, Illinois 60439

ELEVENTH SYMPOSIUM ON ENERGY ENGINEERING SCIENCES
Solid Mechanics and Processing: Analysis, Measurement and Characterization

FOREWORD

The Eleventh Symposium on Energy Engineering Sciences was held on May 3-5, 1993, at the Argonne National Laboratory, Argonne, Illinois. These proceedings include the program, list of participants, and the papers that were presented during the eight technical sessions held at this meeting.

This was eleventh annual symposium sponsored by the Engineering Research Program of the Office of Basic Energy Sciences of the U. S. Department of Energy. As the title indicates, the central theme of this year's meeting was solid mechanics and processing emphasizing modeling and experiments. Each year a group of selected researchers in the DOE/BES Engineering Research Program are invited to present their research findings in such an open forum. By organizing around a central theme, principal investigators, their associates, and other interested parties are able to engage in discussions and share thoughts on subjects of common interests. This format has been used in the Engineering Research Program instead of annual contractors' meetings and has been extremely successful since its inception in 1983.

This symposium was organized into eight technical sessions: surfaces and interfaces; thermophysical properties and processes; inelastic behavior; nondestructive characterization; multiphase flow and thermal processes; optical and other measurement systems; stochastic processes; and large systems and control.

It is appropriate to restate here the goals and mission of the Engineering Research Program. The DOE Office of Basic Energy Sciences, of which Engineering Research is a component program, is responsible for the long-term mission-oriented research in the Department. It has the prime responsibility for establishing the basic scientific foundation upon which the Nation's future energy options will have to be identified, developed, and built; it is committed to the generation of new knowledge necessary for the solution of present and future problems of energy exploration, production, conversion, and utilization, consistent with respect for the environment.

Consistent with the DOE/BES mission, the Engineering Research Program is charged with the identification, initiation, and management of fundamental research on broad, generic topics addressing energy-related engineering problems. Its stated goals are: 1) to improve and extend the body of knowledge underlying current engineering practice so as to create new options for enhancing energy savings and production, for prolonging useful life of energy related structures and equipments, and for developing advanced manufacturing technologies and materials processing with emphasis on reducing costs with improved industrial production and performance quality; and 2) to expand the store of fundamental concepts for solving anticipated and unforeseen engineering problems in the energy technologies.

To achieve these goals, the Engineering Research Program supports about 125 research projects covering a wide spectrum of topics that cut across traditional engineering disciplines with a focus on the following three areas: 1) mechanical sciences; 2) control systems and instrumentation; and 3) engineering data and analysis. The Eleventh Symposium on Energy Engineering Sciences covered the review of approximately one-third of the total activities sponsored by the DOE/BES Engineering Research Program.

The Eleventh Symposium was held under the joint sponsorship of the DOE Office of Basic Energy Sciences and Argonne National Laboratory. The success of the meeting was directly attributable to the active participation of the researchers involved in the program. Several of the participants also served as session chairpersons. Local arrangements for the Symposium were ably handled by Ms. Jacquie Habenicht of the Conference Services Office of ANL. Ms. Mary Hale of the Technical Information Services Department assembled these proceedings and attended to their publication. I am grateful to all those who contributed to the success of the program, particularly to the participants who instilled an atmosphere of intellectual inquiry and excitement. Interactions with such a group made this Symposium a stimulating and thoroughly rewarding experience.

Subhendu K. Datta, ER-15
Division of Engineering
and Geosciences
Office of Basic Energy Sciences

ELEVENTH SYMPOSIUM ON ENERGY ENGINEERING SCIENCES

May 3-5, 1993

Argonne National Laboratory

Argonne, IL

FINAL PROGRAM

Monday, May 3

12:00 noon	Registration
1:00 p.m.	Welcome James S. Coleman, U.S. Department of Energy
1:05 p.m.	General Remarks Oscar P. Manley, U.S. Department of Energy
1:10 p.m.	Introductory Comments Subhendu K. Datta, U.S. Department of Energy

TECHNICAL SESSION 1 - Surfaces and Interfaces

Chair: C. Surko, Univ. of California, San Diego

1:15 p.m.	"Cryotribological Applications in Superconducting Magnets" P. Michael, Y. Iwasa and E. Rabinowicz, MIT
1:40 p.m.	"One Component Surface Waves in Anisotropic Linear Elastic Media" D. Barnett, Stanford University
2:05 p.m.	"Stress-Induced Roughening Instabilities Along Surfaces of Piezoelectric Materials" N. Chien and H. Gao, Stanford University
2:30 p.m.	"Effects of Capillarity on Microscopic Flow in Porous Media" M.J. Miksis and T.-M. Tsai, Northwestern University
2:55 p.m.	"Evolution of Long Wave Disturbances in Horizontal Gas-Liquid Flows" W. Kuru, E. Montalbano, J. Brennecke and M. McCready University of Notre Dame
3:20 p.m.	BREAK

TECHNICAL SESSION 2 - Thermophysical Properties and Processes

Chair: L. Keer, Northwestern University

3:35 p.m. "Fundamental Aspects of Brittle Damage Processes - Discrete Systems"
D. Krajcinovic and V. Lubarda, Arizona State Univ.

4:00 p.m. "Fluidization and Segregation in Bi-Disperse Solid-Liquid Particulate Systems"
H. Kytomaa, C. Peterson, F. McClintock and S. Schiaffino
Massachusetts Institute of Technology

4:25 p.m. "Effect of Carrier Gas Pressure on Condensation in a Supersonic Nozzle"
G. Wilemski, B. Wyslouzil, M. Gauthier and M. Frish
Physical Sciences Inc.

4:50 p.m. "Development of Dual-Sinker Densimeter for High-Accuracy Fluid P-V-T Measurements"
M. McLinden and N. Frederick, NIST

5:15 p.m. "Effective Elastic Properties of Cracked Solids"
M. Kachanov, Tufts University

Tuesday, May 4

TECHNICAL SESSION 3 - Inelastic Behavior

Chair: D. Frederick, VPI & State University

8:00 a.m. "Potential Drop Crack Growth Monitoring in High Temperature Biaxial Fatigue Tests"
B. Fitzgerald and E. Krempl, RPI

8:25 a.m. "The Preisach Model with Stochastic Input as a Model for Aftereffect"
I. Mayergoyz and C.E. Korman, University of Maryland

8:50 a.m. "Small Strain Heterogeneous Deformation in Polycrystals"
S. Shi and E. Jordan, University of Connecticut
K. Walker, Engineering Science Software Inc.

9:15 a.m. "Fully Plastic Fracture Mechanics for Plane Strain Crack Growth"
F. McClintock, Y. Kim and D. Parks, MIT

9:40 a.m. "Fracture Toughness as a Function of Constraint for Simulated Weldments"
W.G. Reuter, W.L. Lloyd and J.S. Epstein, INEL

10:05 a.m BREAK

TECHNICAL SESSION 4 - Nondestructive Characterization

Chair: E. Krempl, Rensselaer Polytechnic Institute

10:20 a.m. "Measurements of the Elastic Constants of Superlattice Films by Line-Focus Acoustic Microscopy"
J. Achenbach, J. Kim and Y.-C. Lee
Northwestern University

10:45 a.m. "Superconducting Property Measurements in Tape Geometry"
K. Telschow, INEL

11:05 a.m. "Photothermal Measurements of Superconductors"
G. Kino, X. Wu, A. Kapitulnik and I. Fishman
Stanford University

11:30 a.m. "Dielectric Studies of Fluids with Reentrant Resonators"
A. Goodwin and M. Moldover
National Institute of Standards & Technology

12:00 noon LUNCH

TECHNICAL SESSION 5 - Multiphase Flow and Thermal Processes

Chair: H. Yuen, Northwestern University

1:00 p.m. "Particle Velocities in Concentrated Suspensions Undergoing Shear"
B. Kapoor and A. Acrivos
City College of the City University of New York

1:25 p.m. "Coupling Effects in Multiphase Free Shear Flows"
T. Troutt, C. Crowe and J. Chung
Washington State University

1:50 p.m. "Wavelength Selection in Traveling-Wave Convection in a Fluid Mixture"
C. Surko, K. Eaton, G. Baxter and K. Iwata
University of California, San Diego

2:15 p.m. "Radiative Transfer through Arrays of Discrete Surfaces"
J. Welty and J. Zaworski, Oregon State University
M. Drost, Battelle Pacific Northwest Laboratories

2:40 p.m. "Aspects of Radiation Heat Transfer in Arrays of Fixed Discrete Surfaces"
M. Drost and B. Palmer, Battelle Pacific Northwest Lab
J.R. Welty, Oregon State University

3:05 p.m. BREAK

TECHNICAL SESSION 6 - Optical and Other Measurement Systems

Chair: J.D. Achenbach, Northwestern University

3:20 p.m. "Nonimaging Reflectors as Functionals of the Desired Irradiance"
R. Winston and H. Ries, University of Chicago

3:45 p.m. "Microscopic Image Processing System for Measuring Nonuniform Film Thickness Profiles: Image Scanning Ellipsometry"
A.-H. Liu, J. Plawsky, and P. Wayner, RPI

4:10 p.m. "Characterization of Thermal Plasmas by Laser Light Scattering"
S. Snyder, G. Lassahn, L. Reynolds and J. Fincke, INEL

4:35 p.m. "Application of Hysteresis Modeling to Magnetic Techniques for Monitoring Biaxial Stress"
M. Sablik G. Burkhardt and H. Kwun
Southwest Research Institute

5:15 p.m. RECEPTION

6:15 p.m. SYMPOSIUM DINNER

Wednesday, May 5

TECHNICAL SESSION 7 - Stochastic Processes

Chair: A. Acrivos, City College of CUNY

8:00 a.m. "Mixing and Settling in Continuous Metal Production"
H. Richter, J. Laaspere and J. Fitzpatrick
Dartmouth College

8:25 a.m. "Experiments on Scalar Mixing and Transport"
Z. Warhaft, Cornell University

8:50 a.m. "Particle Interactions in Concentrated Suspensions"
L. Mondy, Sandia National Laboratories
A. Graham and J. Abbott, Los Alamos National Laboratory
H. Brenner, Massachusetts Institute of Technology

9:15 a.m. "Molecular Mixing in Turbulent Flow"
A. Kerstein, Sandia National Laboratories

9:40 a.m. "Ensemble Phase Averaging for Disperse Two-Phase Flows"
A. Prosperetti and D. Zhang
Johns Hopkins University

10:05 a.m. BREAK

TECHNICAL SESSION 8 - Large Systems and Control

Chair: A. Kerstein, Sandia National Laboratories

10:20 a.m. "Partial Control of Complex Chemical Processes I. Control of Fluidized Catalytic Cracker
R. Shinnar and I. Rinard
City College of the City University of New York

10:45 a.m. "Modeling Aspects of Wave Kinematics in Offshore Structures Dynamics"
P. Spanos, Rice University
R. Ghanem, State University of New York
S. Bhattacharjee, Mobil Research and Development Corp

11:10 a.m. "Intelligent Sensing and Control of Gas Metal Arc Welding"
H. Smartt and J. Johnson
Idaho National Engineering Laboratory

11.35 a.m. "Welding Process Decoupling for Improved Control"
D. Hardt, T. Eagar, J. Lang, and L. Jones
Massachusetts Institute of Technology

12:00 noon Closing Remarks
Oscar P. Manley, U.S. Department of Energy

Table of Contents

CRYOTRIBOLOGICAL APPLICATIONS IN SUPERCONDUCTING MAGNETS

P.C. Michael and Y. Iwasa
Francis Bitter National Magnet Laboratory
Massachusetts Institute of Technology, Cambridge, MA 02139

E. Rabinowicz
Department of Mechanical Engineering
Massachusetts Institute of Technology, Cambridge, MA 02139

ABSTRACT

We have previously advocated the development of materials selection guidelines for high-performance superconducting magnets on the basis of steady-state sliding stability. Theoretical and experimental evidence suggests that inherently stable friction materials may be physically impossible at cryogenic temperatures. We propose an alternate strategy for improving low-temperature sliding stability within the framework of available material behaviors.

INTRODUCTION

The crucial role friction plays in the operation of high-performance superconducting magnets has been recognized for the past 15 to 20 years. Compact, high-current-density, high-performance superconducting magnets are used in such applications as laboratory research magnets, nuclear magnetic resonance (NMR) spectroscopy, magnetic resonance imaging (MRI), and magnetically levitated (maglev) vehicles. Unlike motors, superconducting electromagnets have no intentionally moving parts; the extent of motion that occurs within the magnets is extremely limited except when the magnet is being charged.

The superconducting state is finite; it is bounded by a phase surface consisting of magnetic field, current, and temperature. Of the three, the temperature is neither completely controllable nor predictable. The heat capacity of a superconducting winding at 4.2 K, its usual operating temperature is $\sim 1/4000$ of its room temperature value, hence only a small amount of frictional energy can quench the winding, that is, to drive it into its nonsuperconducting state. High-performance magnets are designed without internal cooling to reduce their overall size and weight, consequently, if a resistive zone does form, it will grow rapidly under the influence of its own ohmic heating, further increasing the magnet temperature. It then becomes necessary to discharge the current and allow the magnet to return to its operating temperature before any further attempts can be made to use it.

A principal source of thermal perturbation in high performance magnets in frictional heating, dissipated either because of relative motion between the entire magnet and its support structure, or because of relative motion between adjacent conductors in the winding. Over the past 15 years considerable effort has been devoted to determining the extent and general location of these motions,[1–3] and developing a variety of cryotribological methods for minimizing their consequences.[3–6]

Much of our research has concentrated on the premise that thermal stability in high-performance magnets can be best achieved by selecting construction materials on the basis of their steady-state sliding stability.[7–10] In absolutely stable sliding pairs, those which possess a positive friction-velocity

characteristic, motion occurs in a smooth, gradual manner resulting in the low-power dissipation of frictional energy. By contrast, unstable pairs are those for which sliding occurs as a series of irregular 'stick-slips'; an extreme example of this instability occurs for materials whose static friction coefficient is substantially larger than the subsequent kinetic value. Because the speed fluctuates rapidly during stick-slip, frictional dissipation occurs as a series of high-intensity heat pulses. Hence, stable motion is sought as a desirable condition for minimizing quench-inducing conductor motions.

ADHESION FRICTION THEORY

The contact between engineering surfaces is concentrated into discrete locations where the asperities, or high points, on each surface touch. The normal stresses at these asperity contacts are quite high, often comparable with the flow strength of the softer surface. For engineering materials the flow strength is typically equated with the indentation hardness. However, for highly elastic materials or materials with marked time-dependent properties it is not unusual for alternate measures of the material's flow strength to be used, those which more accurately reflect the asperities' deformation behavior. The asperity contact diameter for most materials typically ranges from 10 to 100 μm.[11]

The molecular contact between the sliding surfaces within the asperity junctions produces strong intermolecular forces, binding the surfaces together. The strength of the adhesive junctions depends on factor like the chemical compatability and cleanliness of the surfaces, and the time available for the for the junctions to grow to full strength. The adhesive friction force, F, is represented as the product of the junction shear stress, s, times the total real area of contact, A: $F = sA$.

VELOCITY-DEPENDENT FRICTIONAL EFFECTS

Velocity-dependent frictional effects have been observed in several materials. These materials include low melting point metals like lead, tin and indium,[11,12] boundary lubricants like waxes, soaps and fatty acids,[11,13] and elastomeric polymers.[14,15] These materials typically demonstrate small but finite friction coefficient value at very low speeds; the friction coefficients then increase with sliding speed and eventually pass through peak values. The magnitude of the friction peak and corresponding sliding speed depend on the sliding material and test conditions. As the temperature decreases, the speed corresponding to the peak friction coefficient shifts progressively to lower and lower values.[3,14,15]

According to Ludema, these velocity-dependent frictional effects result because of competition between area and strain-rate-dependent-shear-stress effects.[15] Figure 1 presents Ludema's model for the viscoelastic friction peak commonly observed in elastomeric polymers. Because elastomers possess elastic limits typically extending to 100% strain, the contact area is evaluated in terms of the time-dependent creep modulus, while the junction shear stress is related to the rubber's strain-rate-dependent rupture strength. The large elastic modulii observed at high speeds and low temperatures prevent excessive junction growth, thus maintaining relatively low friction values. At low speeds or high temperatures, the strain-rate-dependent junction shear stress drops markedly, resulting in similarly low friction values. The peak friction value results during the transition from small-contact-area, high-shear-stress contact conditions to large-contact-area, low-shear-stress values.

FRICTION-VELOCITY-TEMPERATURE EXPERIMENTS

We have performed friction-velocity measurements at temperatures of 4.2, 77, and 293 K. The sliding tests were performed on the rotational pin-on-disk friction apparatus described previously.[3,7,8] The normal force during these tests was typically 7.5 N while the sliding speed ranged 10^{-7}~10^{-1} m/s. Over the past few years these measurements have emphasized materials, such as silicone rubber, lead, tin, and indium, and boundary lubricants like soaps and fatty acids, which are known to possess

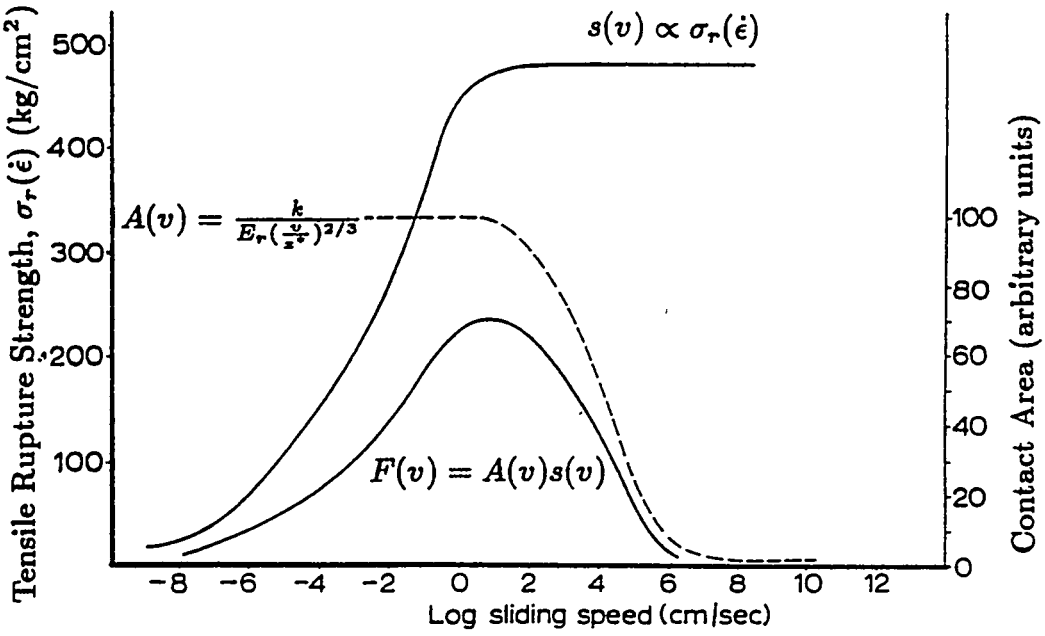

Fig. 1 Schematic representation of velocity-dependent elastomeric friction model. (Figure from [15].)

favorable room-temperature friction-velocity characteristics. Two main reasons for examining these materials were to determine their cryogenics-temperature sliding behaviors, and perhaps more importantly to investigate the fundamental mechanisms of low-temperature frictional stabilization.

A second component of this investigation was the concurrent evaluation of the sliding materials' low temperature mechanical behaviors. These behaviors were determined principally by means of time- and temperature-dependent hardness measurements.[3,16] Hardness measurements are favored for this determination because of their close similarity to the normal contact conditions that prevail at the asperity junctions.[11]

Figure 2 show our velocity-dependent friction coefficients for an indium disk slid against AISI 316 stainless steel pins at temperatures of 4.2, 77, and 293 K. The friction-velocity-temperature results correspond closely to the behavior proposed by Ludema's friction model. At room temperature the competition between junction growth and interfacial shear creep produces a peak friction value of $\sim$6 at a sliding speed of $\sim 10^{-4}$ m/s. Negative friction-velocity characteristics prevail near 77 K; the friction coefficient value decreases from 1.2 at 10^{-7} m/s to 0.5 at 10^{-1} m/s. At 4.2 K the friction coefficient appears virtually independent of velocity and equal in value to 0.5. Similar results have been observed in comparable temperature ranges for several other low-melting-point metals including copper, lead, tin, and mercury.[3,12,17,18]

The friction traces from Fig. 2 were compared with the time- and temperature-dependent hardness data previously obtained by Mulhearn and Tabor.[19] Their measurements were performed at several test temperatures between 77 and 493 K at indentation times ranging $10^{-3}\sim 10^{3}$ s. Three distinct regions of material behavior were observed. At temperatures below approximately 20% of the melting point, $\sim 0.2T_m$, constant hardness values were obtained. In the temperature range $0.2\sim 0.6T_m$ the hardness decreased rapidly for low contact times but eventually approached asymptotic limits. Above $\sim 0.6T_m$ the hardness values can be fitted to a thermally activated creep equation, with an activation energy for the process approximately equal to the metal's self-diffusion activation energy.[19]

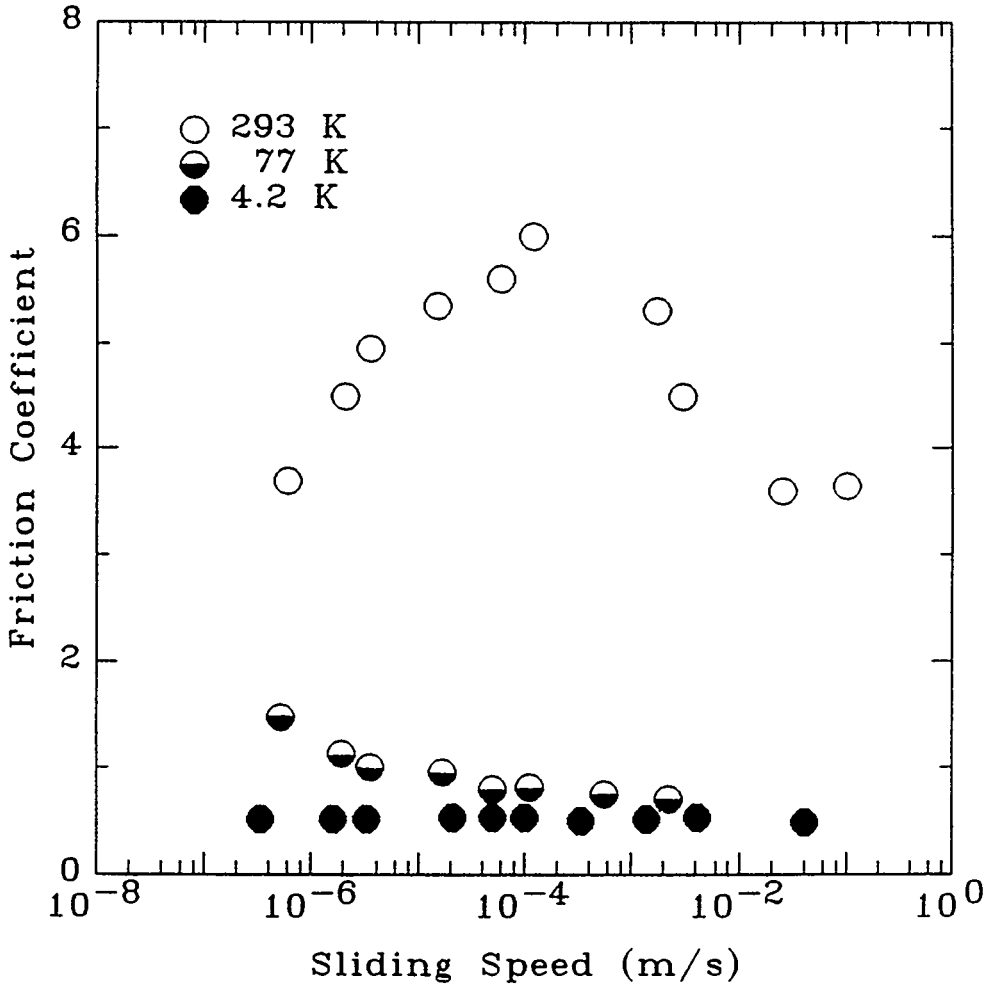

Fig. 2 Friction coefficient *vs* sliding speed for an indium disk slid against AISI316 stainless steel at 4.2, 77, and 293 K. The normal force was 7.5 N.

Our empirical evidence[2,16] and Ludema's friction model[15] both indicate that positive friction-velocity behavior is observed only in materials whose shear stress increases with strain rate. The positive correlation between stress and strain rate is typically observed only at temperatures above 0.3~0.6 of the material's melting temperature, in the viscoelastic region for glassy materials and the creep regime for crystalline materials.[20] At liquid helium temperatures, the usual operating temperature for superconducting magnets, all other materials are substantially below their viscous creep ranges. Thus, we conclude that it is not possible to use absolute steady-state sliding stability as a means for ensuring superconducting magnet thermal stability.

FORCE-BASED MOTION CONTROL

We have recently developed an alternate approach for improving the thermal stability of high-performance solenoidal superconducting electromagnets. That is, to encourage incipient motions to occur as early during the magnet charging cycle as possible rather than relying on the construction materials' intrinsic sliding stability to minimize frictional heating.[6] At the start of operation, a superconducting winding is far from its critical surface, hence it can tolerate substantially greater transient thermal disturbances without reverting to the resistive state than are possible as the magnet nears its rated operating point.

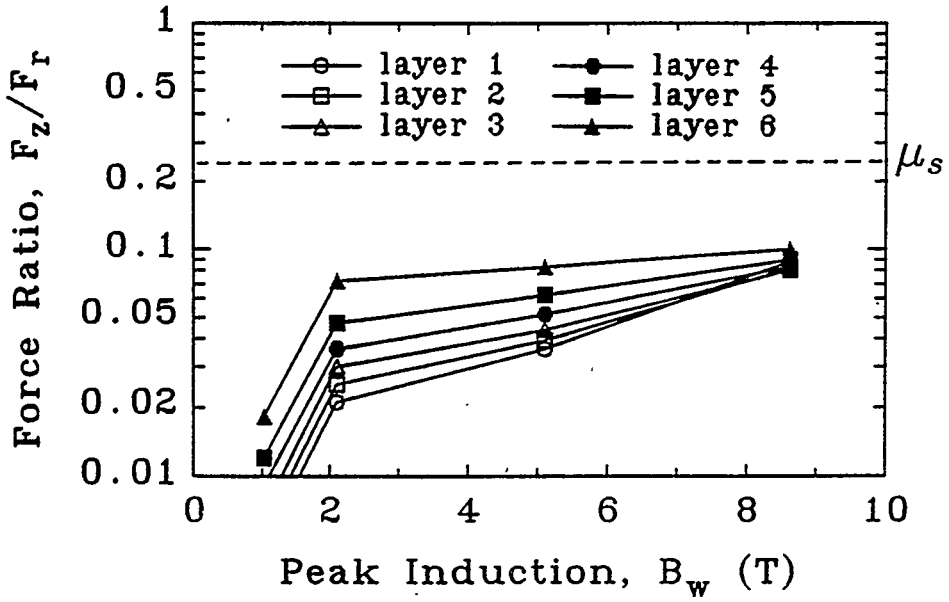

Fig. 3 Variation in the axial/radial conductor force ratios during tight wound coil energization.

The geometry of solenoidal windings makes them especially well suited to the force-based motion control approach.[6] The electromagnetic forces in a simple solenoid are self-constraining. As the magnet is energized the electromagnetic forces tend to expand it radially and compress it axially. However, because it is not possible to wind a perfectly defect free winding, the small axial gaps that are initially present between adjacent conductors allow sufficient space for conductor motions to occur. Conductor-motion-induced quenches are usually caused by the axial displacement of short conductor lengths near the ends of a windings innermost layers, where the ratio of its axial electromagnetic body forces to radial contact forces are often greatest.[6,21] Motion is generally assumed to occur when the ratio of these forces exceeds the conductor's static friction coefficient.

A series of small test magnets were built to examine the effect that the axial-radial force ratio has on the coils' quench characteristics. The coils were constructed with 0.9×1.3 mm Formvar-insulated multifilamentary copper-composite niobium titanium superconducting wires wound on a 76.2 mm inner diameter, 126.2 mm long AISI 316 stainless steel coil form. The radial forces in the coils were controlled in part by externally reinforcing the windings with 0.25×2.5 mm beryllium-copper ribbon. The axial and radial quench initiation locations were determined using the combined acoustic emissions/voltage technique.[1,3,6]

The axial electromagnetic body forces at the ends of each of the coil's six layers were calculated from field maps of the magnetic field during various stages of the energization sequence.[3] The radial interconductor forces were determined using standard 2-dimensional plane-stress approximations.[22] This force distribution was calculated by superposing the effects of the conductor tension during winding, differential thermal contraction between the winding components, and the radial electromagnetic body force. The magnitude and distribution of these radial forces were varied from coil to coil using the programmed winding tension approach advocated by Bobrov and Williams.[22]

Figure 3 shows the predicted axial-radial force ratios *vs* peak magnetic induction for a test coil constructed following the conventional approach, using an extremely high conductor tension to "frictionally pin" the conductors in their as-wound locations. The winding tensions for this magnet consisted of 100 MPa in each conductor layer and 120 MPa in the two beryllium copper overbanding layers. No wire motions were initially anticipated for this coil because its maximum force ratio of ~0.1 is less than accepted value of 0.26 for the conductors static friction coefficient.[21]

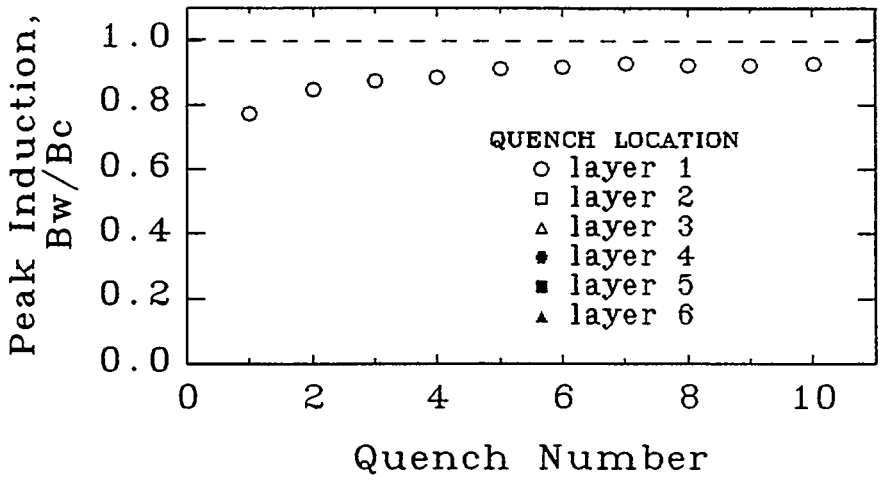

Fig. 4 Quench and training behavior for tight wound coil.

Figure 4 shows the quench characteristic for this tightly wound coil during its first ten training cycles. Its vertical axial presents the peak induction in the winding at quench, B_w, divided by the conductor's critical point induction, B_c. The plotting symbols indicate that all of the quenches initiated in innermost layer, layer 1, as the results of transient conductor motions. The first quench occurred at $\sim 0.77 B_c$. Following this, the coil trained slowly and saturated at a degraded performance of about $0.92 B_c$ after about 6 charging sequences. A recent study has demonstrated that because of statistical fluctuations in thickness along the conductor length it is impossible to exactly predict the ratio of forces acting on any given segment.[23] Given the typical range of dimensional tolerances, the forces needed for frictional immobilization becomes increasingly impractical for large-bore high-field magnets. In fact, high-winding tensions frequently postpone wire motions until late in the magnet's charging sequence where it is much more sensitive to transient thermal perturbations.

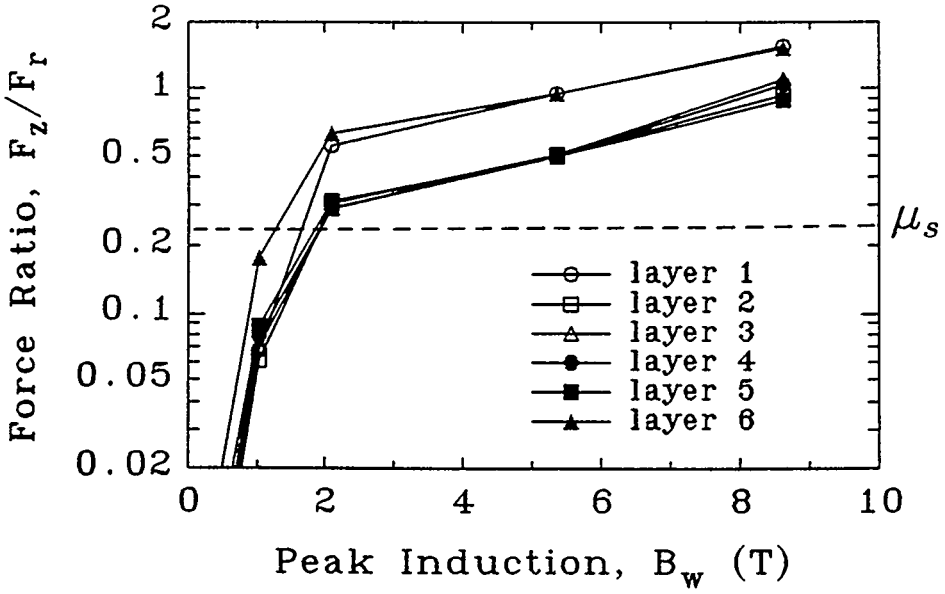

Fig. 5 Variation in the axial/radial conductor force ratios during loose wound coil energization.

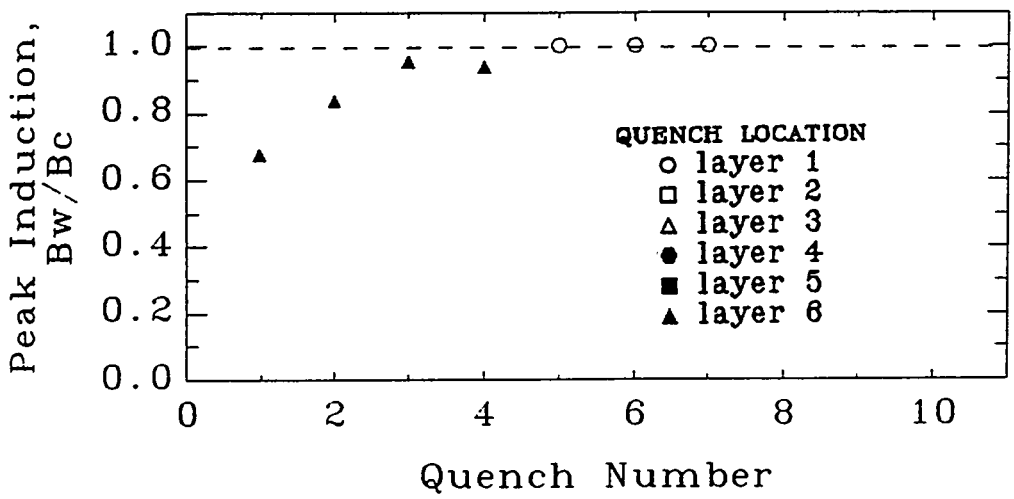

Fig. 6 Quench and training behavior for loose wound coil.

Figure 5 presents the axial-radial force ratios *vs* peak induction for a coil designed to encourage impeding wire motions to as early in the charging sequence as possible. Each wire motion eliminates some of the interconductor spaces, hence, these motions eventually become self-limiting as the entire winding is compressed into a single structural entity. The conductor force ratios in Fig. 5 all pass above the conductor's static friction coefficient while the peak induction in the winding is below 2 T. The winding tensions for this coil consisted of 21 MPa in layer 1, 38 MPa in layer 2, 32 MPa in layers 3, 4 and 5, 49 MPa in layer 6, and no overbanding layers.

Figure 6 shows quench and training characteristics for this loosely-wound coil. All of the motion-induced quenches in this winding occurred near the top of the outermost layer. The first quench occurred at $\sim 0.68 B_c$. However, by the second quench it achieved the same performance level as the tightly-wound coil and then reached its full critical surface limit by its fifth charging cycle. Critical surface quenches typically occur only in the winding's innermost layer where its magnetic induction is greatest. Because of the quench initiation location, and our understanding of the coil's construction technique, we attribute the early training quenches to a poorly designed lead wire termination method. Steps are presently being taken to relieve this deficiency in the coil's design before continuing the investigation.

CONCLUSIONS

To advance our understanding of cryogenic-temperature sliding stability, and thereby to improve the reliability of superconducting magnets, we have initiated an experimental and theoretical program to examine the fundamental mechanisms of frictional stability. The attainment of absolutely stable, positive friction-velocity characteristics at cryogenic temperatures appears improbable because of the lack of thermally-activated steady-state shear creep. We are presently investigating a force-based approach to magnet design that promotes quench-causing conductor microslips to occur early in the magnet's charging cycle where their consequences are relatively benign.

ACKNOWLEGEMENTS

This work was supported in part by the U.S. Department of Energy, Office of Basic Energy Sciences.

REFERENCES

1. **Tsukamoto, O., Maguire, J.F., Bobrov, E.S., and Iwasa, Y.** Identification of quench origins in a superconductor with acoustic emission and voltage measurements *Appl. Phys. Lett.* **39** (1981) 172-174.

2. **Tsukamoto, O., and Iwasa, Y.** Sources of acoustic emission in superconducting magnets *J. Appl. Phys.* **54** (1983) 997-1007.

3. **Michael, P.C.** Cryotribological investigation of sliding motion emphasizing mechanical behaviors of high-performance superconducting magnets *Ph.D. thesis* ME Dept., MIT (1992).

4. **Iwasa,Y., Maguire, J.F., and Williams, J.E.C.** The effect on stability of frictional decoupling for a composite superconductor *8th Symp. Eng. Prob. Fus. Res.* **IEEE CH1441-5/79/** (1979) 1407-1411.

5. **Williams, J.E.C., and Bobrov, E.S.** Magnet system of the 500 MHz NMR spectrometer at the Francis Bitter National Magnet Laboratory: II. Disturbances, quenches, and training. *Rev. Sci. Instrum.* **52** (1981) 657-661.

6. **Michael, P.C., Arata, M., Bobrov, E.S., and Iwasa, Y.** Stabilization of dry-wound high-field NbTi solenoids *IEEE Trans. Appl. Superconductivity* (1993) *to be published.*

7. **Iwasa, Y, Kensley, R., and Williams, J.E.C.** Frictional properties of metal-insulator interfaces *IEEE Trans. Mag.* **MAG-15** (1979) 36-39.

8. **Kensley, R.S., and Iwasa, Y.** Frictional properties of metal insulator surfaces at cryogenic temperatures *Cryogenics* **20** (1980) 25-35.

9. **Maeda, H., Tsukamoto, O., and Iwasa, Y.** The mechanism of frictional motion and its effects at 4.2 K in superconducting winding models *Cryogenics* **22** (1982) 287-295.

10. **Kensley, R.S., Maeda, H., and Iwasa, Y.** Frictional disturbances in superconducting magnets *IEEE Trans. Mag.* **MAG-17** (1981) 1068-1071.

11. **Rabinowicz, E.** *Friction and Wear of Materials* John Wiley, New York (1965)

12. **Burwell, J.T., and Rabinowicz, E.** The nature of the coefficient of friction *J. Appl. Phys.* **24** (1953) 136-139.

13. **Russell, J.A., Campbell, W.E., Burton, R.A., and Ku, P.M.** Boundary lubrication behavior of organic films at low temperatures *ASLE Trans.* **8** (1965) 45-58.

14. **Grosch, K.A.** The relation between the friction and viscoelastic properties of rubber *Proc. Roy. Soc. London* **A 274** (1963) 21-39.

15. **Ludema, K.C., and Tabor, D.** The friction and visco-elastic properties of polymeric solids *Wear* **9** (1966) 329-348.

16. **Michael, P.C., Aized, D. Rabinowicz, E., and Iwasa, Y.** Mechanical properties and static friction behaviour of epoxy mixes at room temperature and at 77 K *Cryogenics* **30** (1990) 775-786.

17. **Bowden, F.P., and Childs, T.H.C.** The friction and deformation of clean metals at very low temperatures *Proc. Roy. Soc.* **A 312** (1969) 451-466.

18. **Coffin, L.F.** Some metallurgical aspects of friction and wear *Friction and Wear: Proc. Symp. on Friction and Wear, Detroit, 1957* Elsevier, New York (1959) 149-164.

19. **Mulhearn, T.O., and Tabor, D.** Creep and hardness of metals: a physical study *J. Inst. Met.* **89** (1960) 7-12.

20. **McClintock, F.A., and Argon, A.S.** *Mechanical Behavior of Materials* Addison-Wesley, Reading, MA (1966).

21. **Urata, M., and Maeda, H.** Relation between radial stress and quench current for tightly wound dry solenoids *IEEE Trans. Mag.* **MAG-23** (1987) 1596-1599.

22. **Bobrov, E.S., and Williams, J.E.C.** Stresses in superconducting solenoids *Mechanics of Superconducting Structures* **ASME AMD-41** (1980) 13-41.

23. **Takao, T., Tsukamoto, O., Amemiya, N., Nishimura, H., Mito, T., Tamura, H., Yamamoto, J., and Motojima, O.** Study on fluctuations in supporting force of conductors caused by fluctuations in conductor dimensions *IEEE Trans. Appl. Superconductivity* (1993) *to be published.*

ONE-COMPONENT SURFACE WAVES IN ANISOTROPIC LINEAR ELASTIC MEDIA

D. M. Barnett

Department of Materials Science & Engineering
Stanford University
Stanford, CA. 94305-2205

ABSTRACT

We consider the possibility that a single partial wave (an inhomogeneous plane wave) can serve as a free surface (Rayleigh) wave in an anisotropic linear elastic half-space. The conditions required for the existence of such a wave are derived from a study of the fundamental eigenvalue problem set by A. N. Stroh for steady plane disturbances in anisotropic solids. We show by direct computation that such one-component waves are necessarily supersonic; since isotropic solids do not admit supersonic surface wave solutions, these one-component waves are pure anisotropic effects. A stable solid of triclinic symmetry yielding one-component surface waves is constructed and discussed. In the limit as the supersonic surface wave speed approaches that of a subsequent transonic state, the one-component surface wave becomes an **exceptional** homogeneous plane wave.

INTRODUCTION

In general a free surface (Rayleigh) wave in an anisotropic linear elastic half-space is constructed from three partial waves which are inhomogeneous plane waves whose amplitudes decay exponentially with distance normal to the traction-free half-space boundary. It is well-known [1,2] that elastic surface waves polarized in a plane of material symmetry (reflection symmetry) consist of only two such partial waves. Thus it is prudent to inquire as to the possible existence of a one-component free surface wave, i.e., a single inhomogeneous plane wave which leaves a half-space boundary traction-free. Such a wave, if indeed it can exist, is the inhomogeneous plane wave analogue of the homogeneous plane waves called **exceptional waves** (or surface-skimming bulk waves) which play a prominent role in the theory of subsonic surface waves. Although the theory of subsonic surface waves is now reasonably established, the development of the theory has been relatively recent, and the Stroh formalism on which it is based has not been widely digested in either mechanics or mathematical circles. Nevertheless, space limitations preclude our presentation here of either the mathematical preliminaries on which the theory is based or more than a cursory reference to the Stroh formalism beyond what is absolutely necessary for the one-component surface wave problem. Therefore, we must assume the reader is at least familiar with the work presented in [3,4].

We consider a stable anisotropic linear elastic half-space (positive definite elastic stiffness C_{ijkl}). The unit inner normal to the half-space boundary is $\mathbf{n}$, and $\mathbf{m}$ is a unit vector in the half-space boundary (and thus normal to $\mathbf{n}$) along the direction of propagation of the free surface wave in the boundary. The plane defined by $\mathbf{m}$ and $\mathbf{n}$ is referred to as the **reference plane**. The candidate for a small amplitude surface wave solution is a displacement field given by the inhomogeneous plane wave

$$u_i = A_i \exp\left[ik\left(\mathbf{m}\cdot\mathbf{x} + p_\alpha \mathbf{n}\cdot\mathbf{x} - vt\right)\right]. \tag{1}$$

The above displacement field is a solution to the equations of motion for any wave number k if the polarization $\mathbf{A}$ and the complex constant p_α are chosen to satisfy the fundamental eigenvalue problem set by

A. N. Stroh, which we present in the next section. The surface wave speed v must be selected to ensure that the above displacement can exist in the half-space with no tractions acting on the half-space boundary, which requires that the three-vector **L** in Stroh's eigenvalue problem must vanish. In order for (1) to actually represent a surface wave in the half-space $\mathbf{n}\bullet\mathbf{x} \geq 0$, the imaginary part of the constant p_α must be positive.

When **L** vanishes, the polarization vector **A** of the (presumed) one-component Rayleigh wave is a solution to the six-dimensional eigenvalue problem

$$[\mathbf{N}]\begin{bmatrix}\mathbf{A}\\ \mathbf{0}\end{bmatrix} = p\begin{bmatrix}\mathbf{A}\\ \mathbf{0}\end{bmatrix}. \tag{2}$$

$|\mathbf{N}|$ is a 6 x 6 real matrix whose form we shall give shortly. From the identity [4]

$$(\mathbf{m} + p\mathbf{n})\bullet\mathbf{L} + \rho v^2\mathbf{A}\bullet\mathbf{n} = 0, \tag{3}$$

where ρ is the half-space mass density, we conclude that $\mathbf{A}\bullet\mathbf{n} = 0$, i.e., the one-component surface wave is polarized **in** the half-space boundary. Furthermore, since p must be complex (for a decaying wave), **A** must be complex with linearly independent real and imaginary parts. If this were not the case the two six-vectors $|\mathbf{A}\ \mathbf{0}|$ and $|\mathbf{A}^*\ \mathbf{0}|$ corresponding to the eigenvalues p and p* would be linearly dependent, which is not possible if p is complex ($p \neq p^*$, its complex conjugate). Thus, both the real and imaginary parts of **A** are orthogonal to **n.**

ANALYSIS OF THE STROH EIGENVALUE PROBLEM

In order to analyze the Stroh eigenvalue problem associated with the one-component surface wave, we adopt the notation

$$(ab)_{jk} = a_i\, C_{ijkl}\, b_l = (ba)_{kj} \tag{4}$$

where we have assumed the full symmetries of the elastic stiffnesses. The 6 x 6 matrix $|\mathbf{N}|$ has the block form

$$[\mathbf{N}] = \begin{bmatrix}\mathbf{N}_1 & \mathbf{N}_2\\ \mathbf{N}_3 & \mathbf{N}_1^T\end{bmatrix}. \tag{5}$$

The 3 x 3 matrices $\mathbf{N_1}$, $\mathbf{N_2}$, and $\mathbf{N_3}$ are real; $\mathbf{N_2}$ and $\mathbf{N_3}$ are symmetric, and $-\mathbf{N_2}$ is positive definite. The actual forms of these three matrices are

$$\mathbf{N_1} = -(nn)^{-1}(nm);\quad \mathbf{N_2} = -(nn)^{-1};\quad \mathbf{N_3} = -(mn)(nn)^{-1}(nm) + (mm) - \rho v^2\mathbf{I} \tag{6}$$

where v is the (supposed) Rayleigh wave speed.

From the eigenvalue problem (2) we find that

$$\mathbf{N_1}\,\mathbf{A} = p\,\mathbf{A} \quad \text{and} \quad \mathbf{N_3}\,\mathbf{A} = \mathbf{0}. \tag{7}$$

Now $\mathbf{N_3}$ is real and **A** is complex with linearly independent real and imaginary parts, so that both the real and imaginary parts of **A** are null vectors of $\mathbf{N_3}$. Since both the real and imaginary parts of **A** are also normal to **n**, any vector in the **m-t** plane (where $\mathbf{t} = \mathbf{m} \times \mathbf{n}$) is a null vector of $\mathbf{N_3}$. In particular,

$$\mathbf{N_3}\,\mathbf{m} = \mathbf{0} \text{ and } \mathbf{N_3}\,\mathbf{t} = \mathbf{0}. \tag{8}$$

As $\mathbf{N_3}$ is real and symmetric, its third eigenvector must be $\mathbf{n}$, as can be verified directly in the following manner. We first note that for any three vectors $\mathbf{a}$, $\mathbf{b}$, and $\mathbf{c}$, the symmetry associated with the elastic stiffness tensor components is such that

$$(\mathbf{ab})\,\mathbf{c} = (\mathbf{ac})\,\mathbf{b} \qquad \text{and} \qquad \mathbf{c}^{\mathbf{T}}\,(\mathbf{ab}) = \mathbf{a}^{\mathbf{T}}\,(\mathbf{cb}). \tag{9}$$

Using (9) and the definition of $\mathbf{N_3}$ in (6) it is a simple matter to show that

$$\mathbf{N}_3\mathbf{n} = -\rho v^2\mathbf{n} \tag{10}$$

so that in an **m-n-t** basis the matrix $\mathbf{N_3}$ has (at the one-component Rayleigh wave speed) the form

$$[\mathbf{N}_3] = \begin{bmatrix} 0 & 0 & 0 \\ 0 & -\rho v^2 & 0 \\ 0 & 0 & 0 \end{bmatrix}. \tag{11}$$

We now proceed to examine the 3 x 3 block matrix $\mathbf{N_1}$. Post-multiplying $\mathbf{N_1}$ by $\mathbf{n}$ yields

$$\mathbf{N}_1\mathbf{n} = -(\mathbf{nn})^{-1}(\mathbf{nm})\mathbf{n} = -(\mathbf{nn})^{-1}(\mathbf{nn})\mathbf{m} = -\mathbf{m}, \tag{12}$$

where we have used (9_1). Thus, we have that

$$\begin{aligned} &\mathbf{m}^{\mathrm{T}}\mathbf{N}_1\mathbf{n} = -1 \\ &\mathbf{n}^{\mathrm{T}}\mathbf{N}_1\mathbf{n} = \mathbf{t}^{\mathrm{T}}\mathbf{N}_1\mathbf{n} = 0. \end{aligned} \tag{13}$$

In addition, from $\mathbf{N}_1\mathbf{A} = p\mathbf{A}$,

$$\mathbf{n}^{\mathrm{T}}\mathbf{N}_1\mathbf{A} = p\mathbf{n}^{\mathrm{T}}\mathbf{A} = p(\mathbf{n}\cdot\mathbf{A}) = 0, \tag{14}$$

since $\mathbf{A}$ is orthogonal to $\mathbf{n}$. Thus $\mathbf{n}^{\mathrm{T}}\mathbf{N}_1$ is orthogonal to $\mathbf{A}$ (and hence to both its linearly independent real and imaginary parts) which is possible if and only if

$$\mathbf{n}^{\mathrm{T}}\mathbf{N}_1 = \gamma\mathbf{n}^{\mathrm{T}}. \tag{15}$$

Post-multiplying (15) by $\mathbf{n}$ reveals that $\gamma = 0$ by virtue of (13). Thus, in addition to (13) we find that

$$\mathbf{n}^{\mathrm{T}}\mathbf{N}_1\mathbf{m} = \mathbf{n}^{\mathrm{T}}\mathbf{N}_1\mathbf{t} = 0. \tag{16}$$

Finally, we have deduced that if a one-component surface wave exists, the block $\mathbf{N_1}$ expressed in an **m-n-t** basis has the form

$$[\mathbf{N}_1] = \begin{bmatrix} N_{11} & -1 & N_{13} \\ 0 & 0 & 0 \\ N_{31} & 0 & N_{33} \end{bmatrix}. \tag{17}$$

Hence, at the one-component surface wave speed, v, the matrix $\mathbf{N} - p\mathbf{I}$, where $\mathbf{I}$ is the 6 x 6 unit matrix, has the form (relative to an **m-n-t** basis)

$$[\mathbf{N}-p\mathbf{I}]=\begin{bmatrix} N_{11}-p & -1 & N_{13} & & & \\ 0 & -p & 0 & & -(nn)^{-1} & \\ N_{31} & 0 & N_{33}-p & & & \\ 0 & 0 & 0 & N_{11}-p & 0 & N_{31} \\ 0 & -\rho v^2 & 0 & -1 & -p & 0 \\ 0 & 0 & 0 & N_{13} & 0 & N_{33}-p \end{bmatrix}. \tag{18}$$

The Stroh eigenvalues p_α (α = 1, 2, ...6) are the six values of p for which the determinant of $[\mathbf{N} - p\mathbf{I}]$ vanishes. Using Laplace's method for expanding the determinant, the six Stroh eigenvalues are found from

$$\left[\{N_{11}-p\}\{N_{33}-p\}-N_{13}N_{31}\right]^2\left[p^2-\rho v^2(\mathbf{nn})^{-1}_{22}\right]=0. \tag{19}$$

The 6 roots are

$$p=\pm\sqrt{\rho v^2(\mathbf{nn})^{-1}_{22}} \tag{20}$$

and

$$p=\frac{1}{2}\left\{(N_{11}+N_{33})\pm\sqrt{(N_{11}-N_{33})^2+4N_{13}N_{31}}\right\}, \qquad \text{twice.} \tag{21}$$

The repeated roots represented by (21) reveal that if a one-component surface wave exists, it must be associated with degeneracy in the Stroh eigenvalue problem. We return to the issue of the type of degeneracy , i.e., semisimple or non-semisimple degeneracy, later. The more important feature of the one-component surface wave problem is the result given by (20). Since the block matrix $\mathbf{N_2}$ is negative definite, the matrix $(\mathbf{nn})^{-1}$ is positive definite [Note that $(\mathbf{nn})$ is the acoustical tensor corresponding to the direction $\mathbf{n}$, which is necessarily positive definite for a **stable** elastic medium; actually, the weaker requirement of strong ellipticity associated with C_{ijkl} is all that is needed to ensure the positive-definiteness of the acoustical tensor associated with any crystallographic direction.] Clearly, equation (19) reveals that two of the Stroh eigenvalues (at the one-component Rayleigh wave speed v) must be real, since the mass density, speed, and the element $(\mathbf{nn})^{-1}$ are real and positive. Since the existence of **real** Stroh eigenvalues corresponds to the supersonic regime, we have deduced that

A one-component surface wave is possible only in the supersonic regime.

We also note that if we are to have a true one-component surface wave representing a displacement whose amplitude decays exponentially with distance from the half-space boundary , the repeated eigenvalues given in (21) must be complex, which requires that

$$(N_{11}-N_{33})^2+4N_{13}N_{31}<0. \tag{22}$$

We have now shown that it is possible for a one-component free surface wave to exist in an anisotropic linear elastic half-space, provided certain conditions are met. It remains only to construct a medium with stable elastic stiffnesses which are capable of admitting these conditions to actually be met. We mention that a necessary, but not a sufficient, condition that (22) be satisfied is that the product $N_{13}\,N_{31} < 0$, i.e., the pair (N_{13} , N_{31}) must be oppositely signed.

Before showing that a stable crystal can be constructed so as to yield a one-component surface wave, it is in order to mention what happens in the event that (a) the inequality in (22) is reversed, or (b) the inequality in (22) becomes an equality. If the inequality in (22) is reversed, the doubly repeated roots given by (21) are **real**, so that all six Stroh eigenvalues are real; the two values of p in (21) now correspond to two

exceptional limiting waves (two homogeneous plane waves leaving the half-space boundary traction-free) associated with a **subsequent** Type 4 transonic state. If the inequality in (22) becomes an equality, all four values of p given by (21) are real and identical, corresponding to a **subsequent** transonic state of either Type 2 for Type E1 (a so-called zero curvature transonic state); there are two limiting exceptional waves associated with each of these subsequent transonic states. Such **exceptional** transonic states (with two exceptional limiting waves) are not possible as first transonic states [4].

In a certain sense one can think of these **exceptional subsequent transonic states** as arising from the one-component surface waves in the following fashion. When the inequality in (22) is satisfied, the one-component surface wave is of the form (1) with

$$i\,\mathrm{Im}(p) = \pm i\sqrt{-(N_{11}-N_{33})^2 - 4N_{13}N_{31}}\,. \tag{23}$$

The + (-) sign in (23) goes with a one-component surface wave of the form (1) decaying exponentially with depth normal to the interface in the half-space $\mathbf{n}\bullet\mathbf{x} > 0$ ($\mathbf{n}\bullet\mathbf{x} < 0$). If we now imagine varying the elastic stiffnesses of the medium continuously so as to maintain a one-component surface wave while the left side of the inequality (22) continuously increases through negative values toward zero (this can actually be done as pointed out by Barnett and Chadwick [5]), we reach a set of stiffnesses for which the radical in (23) vanishes and Im (p) = 0. The **two** one-component surface waves (one inhomogeneous plane wave in each of the "upper" and "lower" half-spaces) have degenerated into two homogeneous plane waves. These homogeneous plane waves are **exceptional** (they leave the have space boundary traction-free), since **each** has **inherited** that property from the one-component surface waves giving rise to them. These two exceptional waves are associated with either a Type 2 or Type E1 subsequent transonic state as explained in [5], depending on whether the Stroh eigenvalue of multiplicity four belongs to one slowness sheet (Type E1) or to two slowness sheets making tangential contact (Type 2).

If the stiffnesses are now continuously varied so that the inequality in (22) undergoes a reversal, the roots given by (21) now form two pairs of **real** roots. One of the roots in **each** pair corresponds to an exceptional limiting wave belonging to a Type 4 transonic state, i.e., the exceptional limiting waves associated with the Type 2 or Type E1 states mentioned in the last paragraph remain exceptional, but these exceptional waves now belong to two **different** points on either one or two of the three slowness sheets.

DEGENERACY OF THE ONE-COMPONENT SURFACE WAVE PROBLEM

Clearly, the one-component surface wave exists only when the Stroh eigenvalue problem is degenerate; two of the Stroh eigenvalues are of multiplicity two. It is interesting to inquire as to the type of degeneracy occuring. Let us consider the eigenvalue p with positive imaginary part given by (21). If the degeneracy is **semisimple**, one eigenvector associated with p is found from equation (2), and a second linearly independent eigenvector is by solving the eigenvalue problem

$$[\mathbf{N}]\begin{bmatrix}\mathbf{A}\\ \mathbf{L}\end{bmatrix} = p\begin{bmatrix}\mathbf{A}\\ \mathbf{L}\end{bmatrix}. \tag{24}$$

If the degeneracy is **non-semisimple**, a second linearly independent eigenvector must be a **generalized** eigenvector found from

$$[\mathbf{N}-p\mathbf{I}]^2\begin{bmatrix}\mathbf{A}\\ \mathbf{L}\end{bmatrix} = \begin{bmatrix}\mathbf{0}\\ \mathbf{0}\end{bmatrix}. \tag{25}$$

It was originally believed [5] that a one-component surface wave was always associated with **non-semisimple** degeneracy, and, in a certain sense, this is correct. Wang and Gundersen [6], however, have actually examined the consequence of having the second eigenvector be an **ordinary** eigenvector defined by (24). The analysis is straightforward and reveals that a second ordinary eigenvector can be found if and only if a certain constraint is obeyed. Usually, non-semisimple degeneracy prevails, and the second eigenvector is a generalized eigenvector. Chadwick [7] had unknowingly found a one-component surface

wave which corresponds to semisimple degeneracy, a fact he uncovered after Wang and Gundersen's analysis led Chadwick to re-examine his earlier study.

Wang and Gundersen's analysis of the second eigenvector as an **ordinary** eigenvector actually leads to a surface wave which can be regarded as the analogue of a "circularly polarized homogeneous plane wave". From (2) and (24), corresponding to the eigenvalue p of multiplicity 2 are two ordinary eigenvectors satisfying

$$[\mathbf{N}]\begin{bmatrix}\mathbf{A}_1\\ \mathbf{L}_1\end{bmatrix} = p\begin{bmatrix}\mathbf{A}_1\\ \mathbf{L}_1\end{bmatrix} \text{ and } [\mathbf{N}]\begin{bmatrix}\mathbf{A}_2\\ \mathbf{L}_2\end{bmatrix} = p\begin{bmatrix}\mathbf{A}_2\\ \mathbf{L}_2\end{bmatrix} . \tag{26}$$

Clearly, any linear combination of the two eigenvectors is an eigenvector, and there is precisely one such combination that produces

$$\mathbf{L} = E_1\,\mathbf{L_1} + E_2\,\mathbf{L_2} = \mathbf{0}, \tag{27}$$

which is the condition for a traction-free boundary. This linear combination **cannot** be used as a **normalized** eigenvector according to the usual Stroh scheme for semisimple degeneracy, namely,

$$2\,\mathbf{A}\bullet\mathbf{L} = 1. \tag{28}$$

When **non-semisimple** degeneracy applies, then the ordinary eigenvector satisfies

$$2\,\mathbf{A}\bullet\mathbf{L} = 0, \tag{29}$$

and this eigenvector can be used in the normalization scheme appropriate for non-semisimple degeneracy. Thus, it seems more reasonable to reserve the term "one-component free surface wave" for the case in which the associated Stroh eigenvector can participate as a **normalized** eigenvector. This definition would preclude semisimple degeneracy, whose associated surface wave would only qualify as a "two-component surface wave with perhaps less exotic appeal.

A MEDIUM ADMITTING A ONE-COMPONENT SURFACE WAVE

Barnett and Chadwick [5] have constructed a one-parameter family of media of triclinic symmetry which admits one-component surface waves and the exceptional subsequent transonic states discussed above. Here we present a single numerical example which the reader may use to verify that indeed a stable linear elastic solid admitting a one-component surface actually is a possibility. The elastic stiffness matrix given by

$$[\mathbf{C}] = \begin{bmatrix} 2/5 & 0 & -2/5 & 3/5 & 0 & 0 \\ 0 & 13/6 & -7/8 & 0 & 1/24 & -4/3 \\ -2/5 & -7/8 & 977/480 & -18/5 & -3/32 & -1 \\ 3/5 & 0 & -18/5 & 72/5 & 0 & 0 \\ 0 & 1/24 & -3/32 & 0 & 37/96 & -1/3 \\ 0 & -4/3 & -1 & 0 & -1/3 & 32/3 \end{bmatrix} \tag{30}$$

can be shown to be stable (Mathematica was used to compute its six eigenvalues, all of which are positive). Furthermore, the eigenvectors of C_{ijkk} were computed to be distinct from those of C_{ikkj}, so that invoking a theorem and algorithm due to Cowin and Mehrabadi [8], the stiffness matrix given in (30) is associated with a stable medium of triclinic symmetry. [C] in (30) is referred to an **m-n-t** basis and corresponds to $\tau = 0$ in [5].

In addition to the one-component surface wave existing in the supersonic regime, if the mass density of the medium is taken as unity, there is a subsonic Rayleigh wave with speed $v = 0.5668$ and a "limiting speed" marking the transition from "subsonic" to "supersonic" at $v = 0.5977$. The one-component surface wave travels at a speed $v = 0.6124$.

SUMMARY

We have derived the conditions under which one-component surface waves exist, and we have shown that such waves are necessarily supersonic. Hence, they are only possible in anisotropic linear elastic solids, since isotropy precludes the existence of supersonic Rayleigh waves. If the eigenvector corresponding to the one-component surface wave is required to be normalizable in the sense of Stroh, then such waves are always associated with non-semisimple degeneracy of the Stroh eigenvalue problem. The elastic stiffnesses of a triclinic solid admitting such a wave have been constructed.

ACKNOWLEDGMENT

This work was performed under the auspices of the U. S. Department of Energy.

REFERENCES

1. P. CHADWICK, "The Behaviour of Elastic Surface Waves Polarized in a Plane of Material Symmetry. I. General Analysis," *Proc. Roy. Soc. London*, A430, 213 (1990).

2. D. M. BARNETT, P. CHADWICK and J. LOTHE, "The Behaviour of Elastic Surface Waves Polarized in a Plane of Material Symmetry. I. Addendum," *Proc. Roy. Soc. London*, A433, 699 (1991).

3. P. CHADWICK and G. D. SMITH, "Foundations of the Theory of Surface Waves in Anisotropic Elastic Materials," in Advances in Applied Mechanics (ed. C.-S. Yih), 17, 303, Academic Press, New York, N. Y. (1977).

4. D. M. BARNETT and J. LOTHE, "Free Surface (Rayleigh) Waves in Anisotropic Elastic Half-Spaces: The Surface Impedance Method," *Proc. Roy. Soc. London*, A402, 135 (1985).

5. D. M. BARNETT and P. CHADWICK, "The Existence of One-Component Surface Waves and Exceptional Transonic States of Types 2, 4, and E1 in Anisotropic Elastic Media," in Modern Theory of Anisotropic Elasticity and Applications (eds. J. J. Wu, T. C. T. Ting, and D. M. Barnett), 199, SIAM, Philadelphia, PA. (1991).

6. L. WANG and S. A. GUNDERSEN, "Existence of One-Component Surface Waves in Anisotropic Elastic Media," *Physica Scripta* (in press).

7. P. CHADWICK, "Some Remarks on the Existence of One-Component Surface Waves in Elastic Materials with Symmetry," *Physica Scripta*, T44, 94 (1992).

8. S. C. COWIN and M. M. MEHRABADI, "Identification of Crystal Symmetry from the Elastic Constant Tensor," *Quarterly Journal Mechanics and Applied Mathematics*, 40, 451 (1987).

STRESS-INDUCED ROUGHENING INSTABILITIES ALONG SURFACES OF PIEZOELECTRIC MATERIALS

Nelly Yung Chien and Huajian Gao
Division of Applied Mechanics, Stanford University, Stanford, CA 94305-4040

ABSTRACT

The possibility of using electric field to stabilize surfaces of piezoelectric solids against stress-induced morphological roughening is explored in this paper. Two types of idealized boundary conditions are considered: 1) a traction free and electrically insulated surface and 2) a traction free and electrically conducting surface. A perturbation solution for the energy variation associated with surface roughening suggests that the electric field can be used to suppress the roughening instability to various degrees. A completely stable state is possible in the insulating case, and kinetically more stable states can be attained in the conducting case. The stabilization has importance in reducing concentration of stress and electric fields due to microscopic surface roughness which might trigger failure processes involving dislocation, cracks and dielectric breakdown.

INTRODUCTION

This paper is concerned with a class of stress-induced instabilities which causes material surfaces to roughen under diffusional mass transport. These instabilities occur, for example, in heteroepitaxial thin films where the elastic strain energy due to lattice misfit provides a thermodynamic driving force for the onset of the island-like surface morphology, also known as the Stranski-Krastonov pattern (e.g., [1]), during film growth or annealing. The conclusion that the strain energy tends to destabilize an initially flat surface and thus to promote the development of surface roughness has been reached by studying linearized kinetic equations along a slightly wavy surface [2] [3] and by showing that the strain energy is always reduced when an initially flat surface is slightly perturbed in an arbitrary manner [4]. Gao [5] [4] also studied the stress concentration along a slightly undulating surface of a stressed isotropic or anisotropic solid and found that even a slightly undulating surface can generate significant stress concentration causing deformation and fracture. It appears that a thorough investigation of the surface roughening instability and the resulting stress concentration is of importance for understanding the nucleation of misfit dislocations in heteroepitaxial thin films [6] [7] and general flaw initiation at material surfaces exposed to environmental corrosions. The significance of microscopic surface roughness is further elucidated by the recent work of Chiu and Gao [8] who adopted a cycloid surface to model periodic rough surfaces. Chiu and Gao found that the cusped cycloid surface generates a crack-like stress singularity within a thin surface layer. Under uniform tension this singularity shows identical strength (i.e. stress intensity factor) as a row of periodic parallel cracks. Even though a rough surface with cusps may not have been perceived to be as dangerous as a periodically cracked body, application of fracture mechanics predicts that the two structures should fail at the same stress level.

The essence of the surface roughening instability leading to formation of stress singularities lies in the competition between elastic energy and surface energy in a stressed material system. The elastic energy can be most efficiently released by formation of localized defects such as cusps, cracks and dislocations. However, such strain relaxation must occur at the cost of creating additional free surfaces, thus increasing the surface

energy of the system. One may show that the elastic energy will dominate over surface energy at relatively long wavelengths (However, at long wavelengths, the gravitational energy may also interfere in the instability process; see [4]). A question that arises is whether other forms of energy such as those of electromagnetic origin can sometimes be utilized to interfere in the instability process so as to control the development of defects. As a first study in that direction, we explore in this paper the possibility of using electric field as a control parameter to minimize or even stabilize the stress-induced surface instabilities in piezoelectric materials.

The subject here is of physical significance. Piezoelectric materials have been widely used as electromechanical transducer, such as ultrasonic generators, filters, sensors, and actuators. Thin films technology plays an important role in many industrial processes and in the fabrication of solid state components. Recent developments involving piezoelectric thin films include applications such as force-sensing resistors [9], built-in vibration sensors [10], molecular sensing devices [11], and surface acoustic waves (SAW) generators [12]. As piezoelectric thin films may be subjected to very large stresses generated by strain sources such as thermal mismatch and lattice mismatch. Stress concentration effects due to an undulating surface may trigger processes involving nucleation of dislocations and cracks. Electric field concentrations might also occur causing dielectric breakdown. Thus, it is of interest to investigate the possibility of controlling surface instabilities with an applied electric field. To achieve our objectives, a perturbation analysis developed in Gao [4] for anisotropic elastic solids is extended to the piezoelectric case. The perturbation solution of energy variations is then used to examine the effects of mechanical and electric loading on the instability wavelength.

Conducting and Insulated Surfaces of a Stressed Piezoelectric Medium

Details concerning the theory of piezoelectricity can be found, for example, in [13] and [14]. The constitutive equations of a piezoelectric medium is usually expressed as

$$\begin{aligned} T_{ij} &= C_{ijkl}S_{kl} - e_{kij}E_k \\ D_i &= e_{ikl}S_{kl} + \epsilon_{ij}E_j \ , \end{aligned} \tag{1}$$

where C_{ijkl} are the stiffness constants measured at a constant electric field, e_{kij} the piezoelectric stress constants, ϵ_{ij} the dielectric constants measured at constant strains, S_{ij} the mechanical strains, T_{ij} the mechanical stresses, D_i the electrical displacements, and E_i the electric field derivable from an electric potential ϕ by $E_i = -\phi_{,i}$. For linear, quasi-static piezoelectricity in absence of body forces and free charges, these quantities satisfy the equilibrium equations $T_{ij,i} = 0$ (mechanical) and $D_{i,i} = 0$ (electrical). Two types of idealized boundary conditions along the free surface are of importance: 1) a traction free and electrically insulated surface and 2) a traction free and electrically conducting surface. Fig. 1 shows these two boundary value problems. The

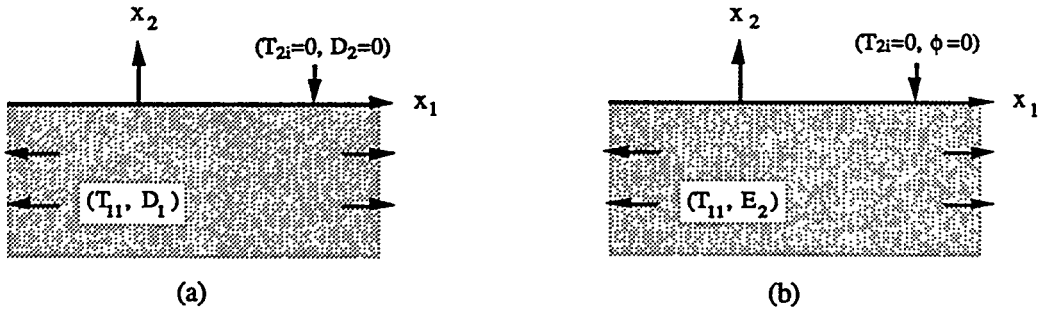

Figure 1: Surfaces of a Piezoelectric Medium with (a) Insulating Boundary Conditions and (b) Conducting Boundary Conditions.

electrically insulating boundary condition corresponds to an adjoining medium with zero dielectric constant and having no free charges residing on the piezoelectric surface. Even though it is not physical to have a

medium with zero dielectric constant, it has been argued in [15] [16] [17] that this condition is approximately attained if the piezoelectric medium has much higher dielectric constant and stronger piezoelectric coupling than the adjoining medium such as air. The electrically conducting boundary condition corresponds to an adjoining medium having much higher electric conductivity. Following Lothe and Barnett [15], we attach a superscript Φ to quantities relating to the insulating case and a superscript F to quantities relating to the conducting case.

In view of thin film applications, we consider a piezoelectric medium subjected to fixed misfit strains S_{11} and S_{33}. To illustrate some typical results, 3% biaxial misfit strain is assumed to exist in the absence of an externally applied electric field. For an insulated surface, we examine the effects of an additional applied electric field E_1 in the longitudinal direction. For a conducting surface, we consider an externally applied electric field E_2 in the transverse direction. Before surface instabilities occur, both the stress field and the electric field quantities are constants, so that the equilibrium equations are automatically satisfied; the unperturbed solutions can be readily deduced from the constitutive equations using appropriate boundary conditions.

The Stability Analysis and A Critical Wavelength

We now investigate whether the surfaces in Fig. 1 are energetically stable, i.e. whether infinitesimal deviations from flatness will be magnified by some kinetic processes such as mass diffusion along the surface. The stability analysis requires the solution to a first order perturbation problem depicted in Fig. 2 where an infinitesimal cosine wave perturbation with amplitude A and wavelength λ is assumed along an otherwise perfectly flat surface. This problem can be solved following a perturbation method used by Gao [4]. For

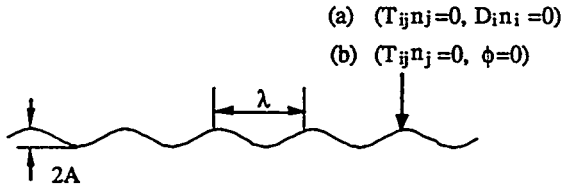

Figure 2: A Cosine Wave Surface with (a) Insulating Boundary Conditions (b) Conducting Boundary Conditions; n_i is the Surface Normal.

conciseness, the details of the mathematical derivations are neglected here. Essentially, the undulating cosine surface problem is converted into a reference flat surface subjected to a distribution of effective surface tractions. The perturbation problem is then solved using a Stroh-like formalism [18] [15] [19] [20] for piezoelectric elasticity problems. The most important result for the stability analysis is the energy change as an initially flat surface (Fig. 1) evolves into the cosine wave surface (Fig. 2). The total energy change (internal energy plus surface energy) per wavelength is found to be

$$\Delta E_{tot} = \frac{\pi^2 \gamma A^2}{\lambda} - \frac{\mathbf{t}_0^T Re[\mathbf{Y}]\mathbf{t}_0}{2}\pi A^2 + O\left[(A/\lambda)^4\right]. \tag{2}$$

The first term on the right hand side represents the change in the surface energy where γ denotes the surface energy density constant and the second term is the change in internal energy. Superscript T implies vector transpose, $\mathbf{t}_0$ is a 4×1 loading vector, and $\mathbf{Y}$ is a 4×4 constant matrix usually referred to as the surface admittance tensor for a piezoelectric medium [15] [19].

The energy expression in Eq. (2) is formally identical to that derived by Gao [4] for the anisotropic elastic case. The reader may be referred to [4] for some helpful insights and discussions. In the piezoelectric case, both the loading vector $\mathbf{t}_0$ and the admittance tensor $\mathbf{Y}$ take different meanings. In the anisotropic elastic case, $\mathbf{t}_0$ is a 3×1 vector and $\mathbf{Y}$ is a 3×3 matrix. The presence of piezoelectric coupling is exhibited as an added fourth dimension in these quantities.

The loading vector $\mathbf{t_0}$ depends on the electrical boundary condition. In the insulating case $\mathbf{t_0}$ takes the form

$$\mathbf{t_0^\Phi} = (T_{11}, 0, T_{13}, D_1)^T \tag{3}$$

where T_{11} and T_{13} denote the mechanical stresses and D_1 is the electric displacement in the x_1 direction induced by an applied electric field. In the conducting case, the loading vector becomes

$$\mathbf{t_0^F} = (T_{11}, 0, T_{13}, -E_2)^T \ . \tag{4}$$

where E_2 is the electric field in the x_2 direction. Note that a conducting surface necessarily implies that E_1 and E_3 vanish.

The admittance matrix $\mathbf{Y}$ also has a strong dependence on the electrical boundary condition. Lothe and Barnett [15] [19] showed that the calculation of $\mathbf{Y}$ can be reduced to an eight-dimensional eigenvalue problem involving the material stiffness C_{ijkl}, piezoelectric coefficients e_{kij} and dielectric constants ϵ_{ij}. In the insulating case, $\mathbf{Y}$ is more explicitly written as $\mathbf{Y^\Phi}$, while in the conducting case $\mathbf{Y^F}$. The properties of $\mathbf{Y^\Phi}$ and $\mathbf{Y^F}$ have been investigated extensively by Lothe and Barnett [15] [19]. In particular, it was shown that both $\mathbf{Y^\Phi}$ and $\mathbf{Y^F}$ are Hermitian matrices with symmetric real parts and anti-symmetric imaginary parts, and have real eigenvalues; $\mathbf{Y^\Phi}$ has three positive and one negative eigenvalues, while all four eigenvalues of $\mathbf{Y^F}$ are positive.

The question of whether a perfectly flat piezoelectric surface is stable amounts to whether the total energy change ΔE_{tot} in going from an initially flat to a slightly undulating surface is positive. In other words, $\Delta E_{tot} > 0$ implies that the flat surface is stable in that any perturbation would tend to increase the energy in the system. On the other hand, if ΔE_{tot} is negative for at least one perturbation wavelength, then a wavy surface is preferred energetically because the energy can be further lowered by roughening. Following Eq. (2), a critical wavelength exists so that the stability condition can be stated as $\lambda < \lambda_{cr}$ where

$$\lambda_{cr} = \frac{2\gamma\pi}{\mathbf{t_0^T} Re[\mathbf{Y}]\mathbf{t_0}} \ . \tag{5}$$

Discussions

Having established the stability condition for a stressed piezoelectric surface, i.e. $\lambda < \lambda_{cr}$, we investigate whether it is possible to suppress surface instabilities by using the electric field as a control parameter. Two types of stabilization can occur leading to a completely stabilized surface or a kinetically more stable surface. The first pertains to applying an external electric field to the system such that $\Delta E_{tot} > 0$ where any perturbation would increase the total energy of the system. This corresponds mathematically to λ_{cr} being negative. For the second type of stabilization, a kinetically more stable surface can be achieved by applying an electric field to the system with a net effect of increasing λ_{cr}. Here, the stressed surface is not truly stable but matter has to diffuse a longer distance in the roughening process, and hence requires a longer period of time. In both cases, what we hope to achieve reduces mathematically to minimizing the product of $\mathbf{t_0^T} Re[\mathbf{Y}]\mathbf{t_0}$. Since the properties of $\mathbf{Y^\Phi}$ for the insulating problem is different from $\mathbf{Y^F}$ for the conducting problem, we will discuss these two cases separately.

To stabilize an insulated piezoelectric surface, we try to minimize the following:

$$\mathbf{t_0^T} Re[\mathbf{Y}]\mathbf{t_0} = \mathrm{y}_{11}^\Phi (T_{11})^2 + 2\mathrm{y}_{13}^\Phi T_{11} T_{13} + 2\mathrm{y}_{14}^\Phi T_{11} D_1 + \mathrm{y}_{33}^\Phi (T_{13})^2 + 2\mathrm{y}_{34}^\Phi T_{13} D_1 + \mathrm{y}_{44}^\Phi (D_1)^2 \ , \tag{6}$$

where y_{ij} representing the real part of Y_{ij}.

There exist three mechanisms for stabilization in an insulating problem. The first arises from the negative nature of y_{44}^Φ. It has been shown by Lothe and Barnett [15] that, for stable materials, the upper 3×3 block of the $\mathbf{Y^\Phi}$ is positive definite, while Y_{44}^Φ is negative definite. If we increase the external electric loading E_1, an increase in electric displacement D_1 will occur in all piezoelectric materials. With a negative y_{44}^Φ in Eq. (6), and using Eq. (5), we see that any increase in D_1 will enlarge λ_{cr} creating a kinetically more stable state. Furthermore, if D_1 is increased beyond a critical value, λ_{cr} will become negative corresponding to $\Delta E_{tot} > 0$, and a totally stabilized surface can be realized. This y_{44}^Φ stabilizing effect exists for all piezoelectric insulated

surface. As a demonstration, we consider a zinc oxide surface under a 3% biaxial misfit strain. The orientation in this example is such that the six-fold rotational axis of symmetry of the crystal coincides with the x_2 axis in our problem. For plotting convenience, we normalized the critical wavelength with respect to its value in the absence of an electric field. This normalized critical wavelength $\hat{\lambda}_{cr}$ is plotted as a function of E_1 in Fig. 3. From this example, we see that an electric field of the order of gigavolts is needed to completely stabilize

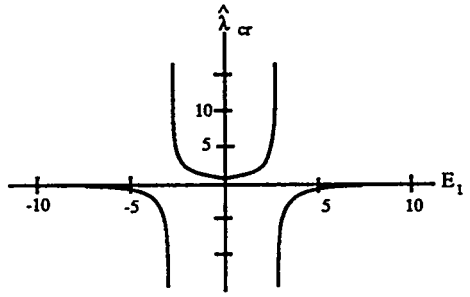

Figure 3: Normalized $\hat{\lambda}_{cr}$ vs. E_1 in Gigavolts for Zinc Oxide in an Insulating Problem

an insulated zinc oxide surface with a 3% misfit strain.

The second mechanism for stabilization can be termed the bulk stress reduction effect where an increase in E_1 may lead to a decrease in the bulk stress T_{11}. This effect occurs in materials where piezoelectric coupling exists between the T_{11} stress and the electric field E_1. Lithium Niobate and Lithium Tantalate, belonging to crystal class *Trigonal* $3m$, are examples of such materials. In addition to the Y^{Φ}_{44} stabilization effect, an insulated surface with this specific coupling behavior can also be stabilized by a reduction of the bulk stress. It must be noted that this stabilizing effect only occurs within a range, if the electric field is increased beyond this range, it might destabilizes the system by overshooting. As this behavior also applies to a conducting problem, additional details and an example on this effect will be presented shortly.

The third mechanism for stabilization occurs in materials, such as quartz of the *Trigonal* 32 class, where piezoelectric coupling exists between the shear stress T_{13} and the electric field E_1. This stabilization effect stems from the cross terms such as $2\mathrm{y}^{\Phi}_{13}T_{11}T_{13}$ and $2\mathrm{y}^{\Phi}_{34}T_{13}D_1$ in Eq. (6). As it is possible to have a negative shear stress T_{13} induced by E_1 and a negative y^{Φ}_{34}, the net effect might decrease the product $\mathrm{t}_0^T Re[\mathrm{Y}]\mathrm{t}_0$ and allowing the surface to attain a kinetically more stable state. We call this the shear stress coupling effect. Since the Y^{Φ}_{44} effect is always present in the isolating case, it is not possible to isolate an example where the shear stress coupling effect alone accounts for stabilization. Thus, an example on this mechanism is not included in this paper.

In general, all three stabilizing mechanisms can be present simultaneously. For the materials we have considered, the Y^{Φ}_{44} stabilization effect is a much more dominant effect than the bulk stress reduction and the shear stress coupling effect. As the Y^{Φ}_{44} effect can completely stabilize an insulated piezoelectric surface, the effects of bulk stress reduction and shear stress coupling are relatively unimportant in the insulating case. However, this is not true in the conducting case.

For conducting surfaces, the product that we try to minimize for stabilization is

$$\mathrm{t}_0^T Re[\mathrm{Y}]\mathrm{t}_0 = \mathrm{y}^F_{11}(T_{11})^2 + 2\mathrm{y}^F_{13}T_{11}T_{13} - 2\mathrm{y}^F_{14}T_{11}E_2 + \mathrm{y}^F_{33}(T_{13})^2 - 2\mathrm{y}^F_{34}T_{13}E_2 + \mathrm{y}^F_{44}(E_2)^2 \ . \qquad (7)$$

In this case, the 4×4 Y^{F} matrix has been shown by Lothe and Barnett [15] to be positive definite. Thus, unlike the insulating case where the surface can be stabilized by the Y^{Φ}_{44} effect, stabilization of a traction free and conducting piezoelectric surface can only be achieved by bulk stress reduction or by shear stress coupling. These two mechanisms do not completely stabilize a conducting surface, only leading to a kinetically more stable state.

To demonstrate the effects of bulk stress reduction in a conducting problem, we consider the example of zinc oxide under a 3% misfit strain. The orientation of the crystal here is identical to that in the insulating example. The result for the normalized critical wavelength $\hat{\lambda}_{cr}$ is plotted in Fig. 4. The bulk stress reduction effect is the only stabilization mechanism present in this example, and we found that an applied electric field of one gigavolts in the x_2 direction causes a 25% increase in λ_{cr}. In several other cases that we have studied.

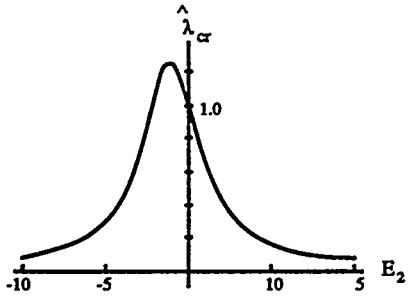

Figure 4: Normalized λ_c vs. E_2 in Gigavolts for Zinc Oxide in a Conducting Problem

the percentage increase in λ_{cr} is less than 10%. This seems to suggest that the bulk stress reduction effect is not particularly effective in controlling instabilities in conducting piezoelectric surfaces. However, in materials exhibiting quadratic effects such as electrostriction and magnetostriction, an increase in electric or magnetic field might lead to a significant reduction in the bulk stress. These effects should be investigated as they might provide better alternatives for stabilization of stressed surfaces.

The shear stress coupling cross terms in Eq. (7) for a conducting surface are identical to that for an insulated surface in Eq. (6). Therefore, as discussed in the insulating case, shear stress coupling effect is also a feasible mechanism, mathematically, for controlling instabilities in a conducting surface. However, we are unable to find a physical example to illustrate this effect. For the materials we have considered, a non-zero shear stress T_{13} either has no effect on stabilization or it leads to instabilities.

Both stabilizing mechanisms for a conducting surface depends on piezoelectric coupling between T_{11}, T_{13} and E_2, thus stabilization is impossible for materials in an orientation where such coupling effect is absent. In fact, an applied E_2 in these cases will only destabilize the system.

Based on the above discussions, it seems possible, at least mathematically, to control the surface stability of a piezoelectric solid by varying an applied electric field in both the insulating and the conducting case. However, we must also address the difficulty in applying these electrical loading physically. With a conducting piezoelectric surface, it might be possible to apply E_2 by imposing an electric potential on the surface. Since x_2 is the thickness direction, typically small on a thin film, a small potential difference might generate a large electric field. A possible setup of this is to grow an insulated thin film on a capacitor plate. Applying E_1 to an insulated surface is an obviously more difficult task, it might be done by setting the surface transverse to a set of parallel capacitor plates.

Also, as an applied electric field of the order of gigavolts is needed to stabilize surface instabilities in thin film applications, we must also investigate other possible adverse effects on the piezoelectric medium caused by an electric field of such magnitude.

Conclusions

In this paper, we have extended the morphological stability analysis for anisotropic materials by Gao [4] to address surface roughening in piezoelectric medium. In contrast to the analysis for an anisotropic medium, where Gao concluded that the surface is always unstable under sufficiently large bulk stress, we found that the electric field can be used as a control parameter to stabilize a stressed piezoelectric surface. Two sets of boundary conditions were considered: A traction free and insulated surface and a traction free and conducting surface.

The stability condition is obtained from analyzing the total energy change associated with roughening of a flat surface. To completely stabilize a stressed flat surface, we try to apply an electric field such that $\Delta E_{tot} > 0$ in Eq. (2). In this case, any perturbation of the flat surface would result in an overall increase of energy for the system. The stability condition can also be expressed in terms of a critical wavelength $\lambda < \lambda_{cr}$. If we can increase this critical wavelength λ_{cr} by applying an electric field, a kinetically more stable state can be achieved.

Three types of stabilizing mechanisms are possible. The first is referred to as the Y_{44}^{Φ} effect and it is applicable only to an insulated surface. This effect arises from the non-positive definiteness of the admittance matrix for an insulating problem. With a large enough electric field in the x_1 direction, this Y_{44}^{Φ} effect can completely stabilize a flat insulated surface. For a conducting surface, a stabilizing mechanism is the bulk stress reduction effect. This effect stems from the piezoelectric coupling of the T_{11} stress and the electric field component E_1. By applying an optimal E_1, we can attain a kinetically most stable state for a conducting surface via bulk stress reduction. The third stabilizing mechanism is the shear stress coupling effect and it arises from a coupling between the shear stress T_{13} and electric components E_1 or E_2. Mathematically this effect can be present in both the insulating and conducting cases. However, the influence of this effect in the insulating case is minimal compared to the Y_{44}^{Φ} stabilization. Furthermore, in the conducting case, a physical example cannot be found where shear stress coupling stabilizes the surface.

As stress and electric field concentrations associated with an undulating surface might lead to mechanical failures, the stabilization of stressed piezoelectric surfaces should be an important concern. In the insulating case, we have shown that a possible mechanism exists, at least mathematically, for complete stabilization of a stressed surface. For a conducting surface, even though a completely stable surface is not attainable by the stabilizing mechanisms presented here; we have shown that it is possible, for some materials, to achieve a kinetically more stable state.

Due to the length restriction imposed on this paper, many of the necessary mathematical theories and details relating to the derivation of our results are not presented here. They will be reported in another paper in the near future.

Acknowledgement

This work was supported by the U.S. Department of Energy under grant DE-FG03-91ER14196. This support is gratefully acknowledged.

References

1. J. W. Matthews, "Coherent Interfaces and Misfit Dislocations," in *Epitaxial Growth*, ed. J. W. Mathews, Academic Press, New York, Part B, Chap. 8, (1975).

2. D. J. Srolovitz, "On the Stability of Surfaces of Stressed Solids," *Acta Metallurgica*, 37, pp. 621-625, (1989).

3. B. J. Spencer, P. W. Voorhees, and S. H. Davis,"Morphological Instability in Epitaxially Strained Dislocation-Free Solid Films," *Physical Review Letters*, 67, pp. 3696-3699, (1991).

4. H. Gao, "Morphological Instabilities Along Surfaces of Anisotropic Solids," in *Modern Theory of Anisotropic Elasticity and Applications*, eds. J.J. Wu, T.C.T. Ting and D.M. Barnett, SIAM, pp. 139–150, (1991).

5. H. Gao, "Stress Concentration at Slightly Undulating Surfaces," *Journal of the Mechanics and Physics of Solids*, 39, pp. 443-458, (1991).

6. L. B. Freund, "The Stability of a Dislocation Threading a Strained Layer on a Substrate," *Journal of Applied Mechanics*, 54, pp. 553-557, (1987).

7. W. D. Nix, "Mechanical Properties of Thin Films," *Metallurgical Transactions A*, 20A, pp. 2217-2245, (1989).

8. C. H. Chiu and H. Gao, "Stress Singularities Along a Cycloid Rough Surface," to appear in *Int. J. Solids Structures.*

9. T. Ormond, "Touch-Responsive Devices Enable New Applications," *EDN (European Edition)*, 38, No. 2, pp.39–40, 42, 44, (1993).

10. S. Egusa *et. al.*, "Piezoelectric Paints: Preparation and Application as Built-in Vibration Sensors of Structural Materials," *Journal of Materials Science*, 28, No. 6, pp 1667–72, (1993).

11. I. Sugimoto *et. al.*, "Molecular Sensing Using Plasma Polymer Thin-Film Probes," *Sensors and Actuators B (Chemical)*, B10, No. 2, pp.117–22, (1993).

12. Akinaga, Masahiro *et. al.*, "Surface Acoustic Waves (SAW) in High-T//c Superconducting Thin Films on Piezoelectric PbTiO//3 Films," *Japanese Journal of Applied Physics, Part 1: Regular Papers & Short Notes*, 31, No. 9B, pp.2978–2981, (1992).

13. H .F. Tiersten, *Linear Piezoelectric Plate Vibrations*, Plenum Press, New York, (1969).

14. B.A.Auld, *Acoustic Fields and Waves in Solids*; Vol. I, John Wiley & Sons, New York, (1973).

15. J. Lothe and D. M. Barnett, "Integral Formalism for Surface Waves in Piezoelectric Crystals. Existence Considerations," *Journal of Applied Physics*, 47, No. 5, pp. 1799–1807, (1976).

16. Y. E. Pak, "Circular Inclusion Problem in Antiplane Piezoelectricity," *Int. J. Solids Structures*, 29, No. 19, pp. 2403–2419, (1992).

17. H. Sosa, "On the Fracture Mechanics of Piezoelectric Solids," *Int. J. Solids Structures*, 29, No. 21, pp. 2613–2622, (1992).

18. A. N. Stroh, "Dislocations and Cracks in Anisotropic Elasticity," *Philosophical Magazine*, Ser. 8, 3, pp. 625–646, (1958).

19. J. Lothe and D. M. Barnett, "Further Development of the Theory for Surface Waves in Piezoelectric Crystals," *Physica Norvegica*, 8, No. 4, pp. 239–254, (1977).

20. C. M. Kuo, "Selected Two-Dimensional Static and Dynamic Problems in Anisotropic Elastic and Piezoelectric Media," Ph.D. Dissertation, Stanford University, (1992).

Effects of Capillarity on Microscopic Flow in Porous Media

Michael J. Miksis and Tse-Min Tsai
Department of Engineering Sciences
and Applied Mathematics
Northwestern University
Evanston, Illinois 60208

Abstract

Here we study the effect of capillarity on a microscopic problem related to foam flow in porous media: the transport of a bubble or drop through a constricted capillarity tube. The aim is to study the snap off process which occurs during the formation of a foam in a porous media. We illustrate the dynamics of the bubble for different initial data and for several different sets of the physical parameters.

Introduction

The behavior of a single phase fluid as it flows in a porous medium is governed by the properties of the fluid and the geometry of the porous material. For a two-phase flow in a porous material, we have the additional dependence on the interaction of the two fluids. In particular, the surface tension between the two phases can have a major influence on the microscopic (pore size) dynamics of the mixture. Hence the macroscopic behavior of the two-phase flow must depend on the microscopic dynamics of the two fluids. One important type of two-phase flow in a porous material is foam flow. This is because of its applications to enhanced oil recovery and hazardous waste management. Our aim here it to study a microscopic problem which occurs in foam flow. In particular here we will study numerically the generation process of a foam. The dominate mechanism for this is called 'snap-off'. This is related to the instability of a gas bubble as it moves through a constriction in the porous material. As the bubble moves through the constriction an instability is initiated which results in the bubble splitting into two (or more) parts. The result of many of these divisions occurring is a foam.

In order to study the basic phenomena of the generation of a foam, we will consider flow in a capillary tube. This geometry has been used by many others in the study of flow in porous media. We will first consider the problem of a pressure driven bubble in a capillary tube. There have been many investigations of this problem. In particular, Bretherton [1] consider the steady motion of a semi-infinite bubble in a tube. By using lubrication theory, he was able to show that the speed U of the bubble exceeds the average speed of the fluid by the amount UW where W is proportional to the Capillary number to the 2/3 power. There was considerable work to follow this up. For example Park and Homsy [2] used a matched asymptotic analysis to justify Bretherton's result and later Schwartz et al. [3] compared the predictions of Bretherton's theory with experiment and found an

under prediction of the film thickness for long bubbles but good agreement for bubbles of length less than 20 tube radii. Also Reinelt and Saffman [4] computed the exact shape and speed of a steadly moving semi-infinite bubble in a capillary tube numerically. Later Martinez and Udell [5] computed the steady motion of a bubble of finite size in a pressure driven flow in a capillary tube.

Our primary concern will be with the transient motion of a bubble or drop (both words will be used here) through a constriction in the capillary tube. There has also been some recent works in this direction. For example, Pozrikidis [6] has studied the transient motion of a period array of bubbles in a straight capillary tube. This work was primarily directed to determining the steady motion although some unsteady cases were considered. The periodicity had a big effect unless the bubbles were widely spaced. In the case of a constricted capillary tube, Gauglitz and Radke [7] used a lubrication model to study the dynamics of a semi-infinite bubble. In particular they did observe snap-off and found that the snap-off times compared well to experiment when the initial data was taken from an experiment. On the other hand, their lubrication model was not asymptotic in its treatment of the curvature term. In particular, since the pinching instability for flow of a thin film in a capillary is primarily due to the effect of the curvature, a careful treatment of the equations of motion is important to an understanding of the dynamics of the bubble. Our aim is to study the dynamics of a bubble of finite length as it passes through a constriction (Tsai [8] and Tsai and Miksis [9]). This will be done numerically using a boundary-integral method.

Formulation

Consider the pressure driven motion of a bubble or drop in a axisymmetric capillary tube (see Fig. 1). Letting (r, z) be cylindrical coordinates with the z-axis along the centerline of the tube. Suppose that the suspending fluid of viscosity μ flows at a constant flux Q and that the velocity profile far upstream and downstream is given by a steady Poiseuille profile. Inside of the tube suppose that there is a drop of fluid of viscosity $\lambda\mu$ of undeformed volume $4\pi a^3/3$. Here a is called the effective radius of the drop. The problem is to determine the dynamics of the drop as it moves within the capillary tube given an initial shape. For straight-sided tubes steady state shapes can be expected for certain values of the parameters. For tubes with a constriction, steady shapes can only be expected downstream of the constriction. Denote the region containing the suspending fluid by Ω_1 and the region containing the drop by Ω_2.

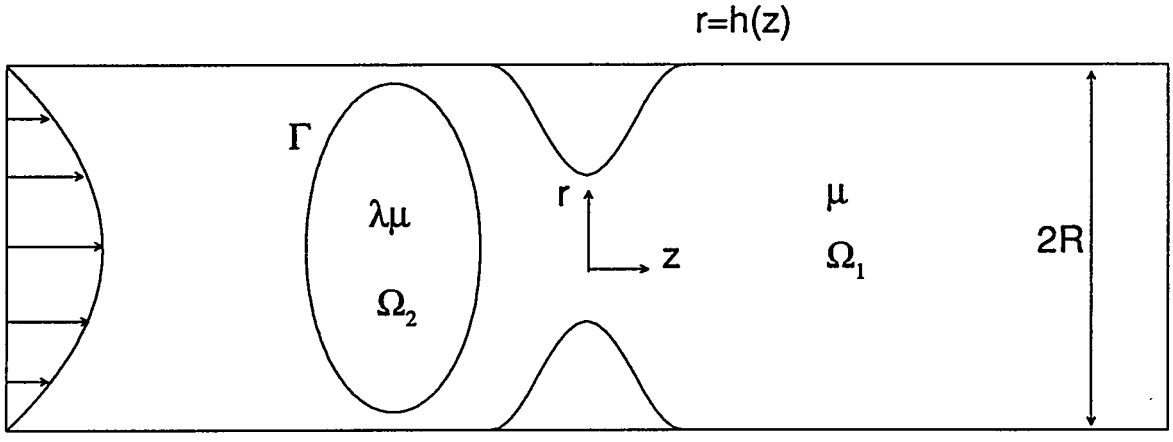

Fig.1 Bubble in a Constricted Capillary Tube

We assume that the motion of the fluid is governed by the Stokes equations. Hence in the fluid region Ω_i, the equations of motion

$$\nabla \cdot \vec{v}_i = 0, \tag{1}$$

$$\nabla \cdot \Sigma_i = 0, \tag{2}$$

where $\vec{v}_i$ is the velocity vector and Σ_i is the stress tensor for the fluid,

$$\Sigma_i = -p_i I + \lambda_i \left[\nabla \vec{v}_i + (\nabla \vec{v}_i)^t\right]. \tag{3}$$

Here p_i is the pressure, $\lambda_1 = 1$ and $\lambda_2 = \lambda$. The superscript t in (3) means transpose. The boundary conditions along the tube surface, $r = h(z), -\infty < z < \infty$ is no-slip,

$$\vec{v}_1 = 0. \tag{4}$$

Along the unknown interface, Γ, between the two fluids we have the continuity of velocity,

$$\vec{v}_1 = \vec{v}_2, \tag{5}$$

the stress condition

$$(\Sigma_1 - \Sigma_2) \cdot \vec{n} = \frac{1}{Ca}(\nabla \cdot \vec{n})\vec{n}, \tag{6}$$

and the kinematic condition

$$\frac{\partial \vec{Y}}{\partial t}(r, z, t) \cdot \vec{n} = \vec{v} \cdot \vec{n}. \tag{7}$$

Here, $\vec{Y}(r, z, t)$ is the position vector of the interface Γ. In addition we have the upstream and downstream conditions that the velocity profile becomes parabolic,

$$\vec{v}_1 = 2(1 - r^2)\vec{z}. \tag{8}$$

The variables in (1)-(8) are dimensionless with the tube radius R at infinity as the unit of length, $Q/\pi R^2$ as the unit of velocity, $\mu Q/\pi R^3$ as the unit of pressure (and stress) and $\pi R^3/Q$ as the unit of time. We have also introduced the Capillary number $Ca = \mu Q/\pi\gamma R^2$ where γ is the surface tension. In addition $\vec{z}$ is the unit vector parallel to the z-axis and $\vec{n}$ is a unit vector normal to Γ pointing into the drop. Finally we would like to define the dimensionless effective radius of the drop as $r_e = a/R$, our results will be presented as a function of this parameter and the Capillary number.

Numerical Method

In order to solve the moving boundary problem (1)-(8) with a given set of initial data we will us a boundary integral method (see e.g., Rallison and Acrivos [10] and Pozrikidis [11]). The idea here is to reformulate (1)-(8) as an integral equation along the surface of the drop and the tube walls. Solve this integral equation for the velocities along Γ and then use the kinematic condition (7) to advance the moving boundary Γ. Following Rallison and Acrivos [10] we can reformulate (1)-(8) as the integral equation over the moving boundary Γ and the fixed boundary Γ_w which is determined by the size of the computational domain. In particular, if the computational domain is given by $K_1 \le z \le K_2$ then Γ_w includes that portion of the tube wall for these values of z plus the cross sections of the tube at $z = K_1$ and $z = K_2$. We will assume that the velocity profiles at

$z = K_i, i = 1, 2$ is given by (8). Following Rallison and Acrivos [10] we find that along the boundary Γ or Γ_w the following integral equation holds,

$$
\begin{aligned}
kC\vec{v}(\vec{x}) &- \frac{3}{4\pi}\int_{\Gamma_w}\frac{(\vec{x}-\vec{y})}{|\vec{x}-\vec{y}|^5}[(\vec{x}-\vec{y})\cdot\vec{n}(\vec{y})][(\vec{x}-\vec{y})\cdot\vec{v}(\vec{y})]d\Gamma_w(\vec{y}) \\
&- (1-\lambda)\frac{3}{4\pi}\int_{\Gamma}\frac{(\vec{x}-\vec{y})}{|\vec{x}-\vec{y}|^5}[(\vec{x}-\vec{y})\cdot\vec{n}(\vec{y})][(\vec{x}-\vec{y})\cdot\vec{v}(\vec{y})]d\Gamma(\vec{y}) \\
&= -\frac{1}{8\pi}\int_{\Gamma_w}\left[\frac{\vec{T}}{|\vec{x}-\vec{y}|}+\frac{\vec{x}-\vec{y}}{|\vec{x}-\vec{y}|^3}(\vec{x}-\vec{y})\cdot\vec{T}\right]d\Gamma_w(\vec{y}) \\
&- \frac{1}{8\pi}\frac{1}{Ca}\int_{\Gamma}\left[\frac{\vec{n}}{|\vec{x}-\vec{y}|}+\frac{\vec{x}-\vec{y}}{|\vec{x}-\vec{y}|^3}(\vec{x}-\vec{y})\cdot\vec{n}\right](\nabla\cdot\vec{n})d\Gamma(\vec{y}).
\end{aligned}
\tag{9}
$$

Here $\vec{n}$ represents the unit outward normal along the boundary of Ω_1 pointing out of the region, $\vec{v}$ is the fluid velocity vector and $\vec{T} = \Sigma_2 \cdot \vec{n}$. Also $k = 1 + \lambda$ if the position vector $\vec{x}$ is along Γ while $k = 1$ if $\vec{x}$ is along Γ_w. In addition the tensor C depends on the smoothness of the boundary, e.g., for a smooth boundary point $C = -\frac{1}{2}I$ (see e.g., Pozrikidis [11]).

An outline of the numerical method to advance the interface a time step Δt goes as follows. First select the number of mesh points along the boundaries of the wall Γ_w and the interface Γ. Assume that the initial shape of the drop is given. Compute the total arc length of the drop. Spline fit the radius and axial coordinates along the interface in terms of arc length and redistribute the mesh points along the interface with equal arc length. Solve the integral equations (9) to obtain the velocities along the interface Γ. Use the kinematic condition (7) to update the interface. This equation is integrated by using a 2nd order Runge-Kutta scheme. Hence this involves first updating the interface by a time step $\Delta t/2$. Then this information is required to update the interface to the time step Δt. Therefore we again need to fit a cubic spline to the interface, redistribute the points, and solve the integral equation for the updated interface. Then this updated interface is used in the Runge-Kutta scheme to get the final prediction at the time step Δt. The above is then repeated to advance to $2\Delta t$ and beyond. The calculations were all done on an IBM RS6000 workstation and the results presented here are graphically accurate. The scheme appears to be second order accurate. This was illustrated by computational checks. In addition the volume of the droplet was computed as we advanced in time as a check on the accuracy of the scheme.

Computational Results

Our aim here is to illustrate some of the types of behavior that can happen to a bubble as it is flowing within a capillary tube. We will begin with some examples of a straight-walled tube and then introduce the constriction. In Fig. 2 an initially spherical bubble of $r_e = 0.9$ and $\lambda = 0.1$ was placed in the flow inside of a straight-walled capillary tube. In Fig. 2a we set $Ca = 0.1$ and we see that the bubble approachs a steady state shape which is elongated compared to the initial data (Note the difference in the vertical and horizontal scales). In Fig. 2b we set $Ca = 1.0$. In this case the bubble elongates with the back of the bubble increasing towards the front (a re-entrant cavity) as a function of time. Hence we see that the effect of the Capillary number is to change the shape of the bubble significantly.

The effect of the initial data is illustrated in Fig. 3 for a bubble with $r_e = 0.7667$ and $\lambda = 0.1$ The initial data here is an ellipsoid as illustrated. In Fig. 3a we set the flux $Q = 0$, hence $Ca = 0$. A slightly different scaling of the variables was necessary in order to do this. We see that the pinching

Fig.2 Spherical Bubble in Straight Capillary

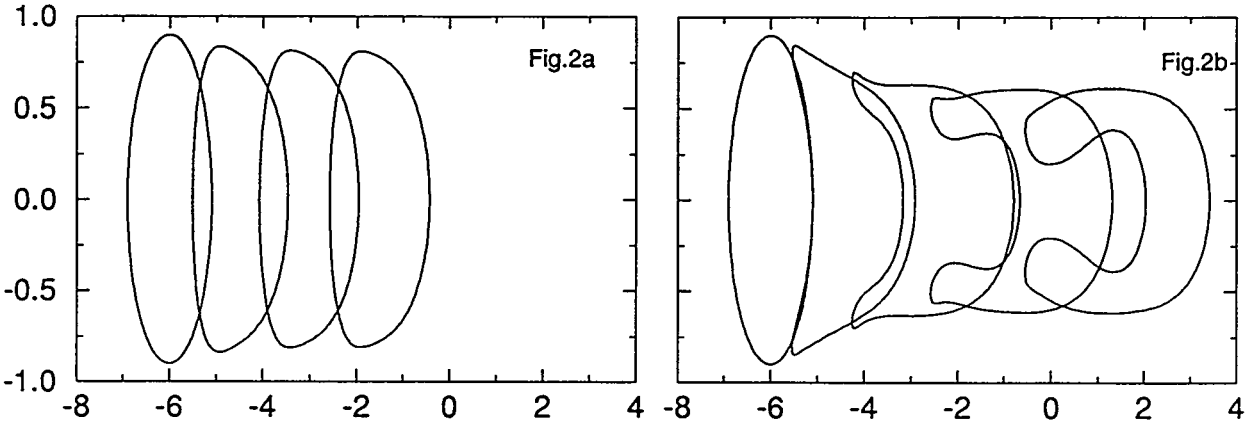

Fig.3 Long Narrow Bubble in Straight Capillary

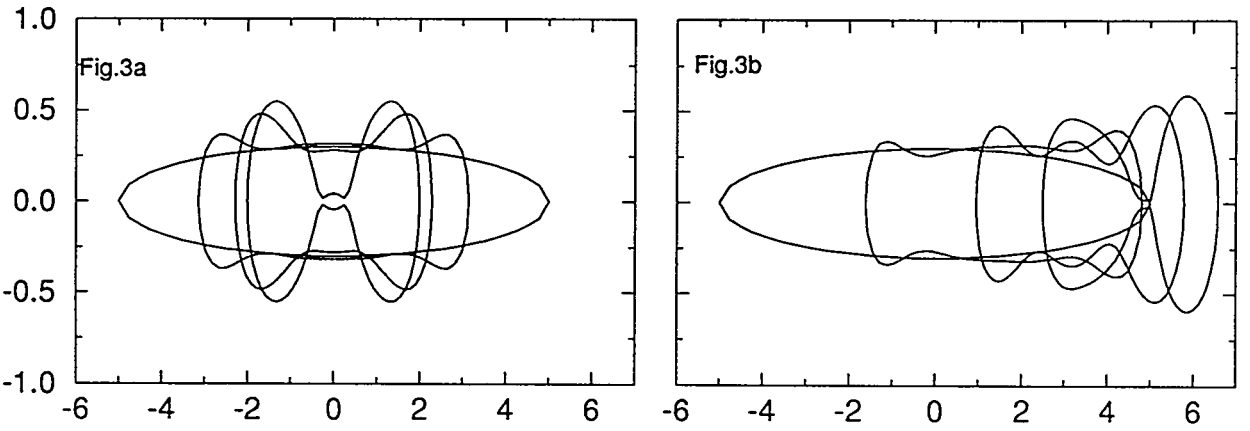

Fig.4 Spherical Bubble in Constricted Capillary

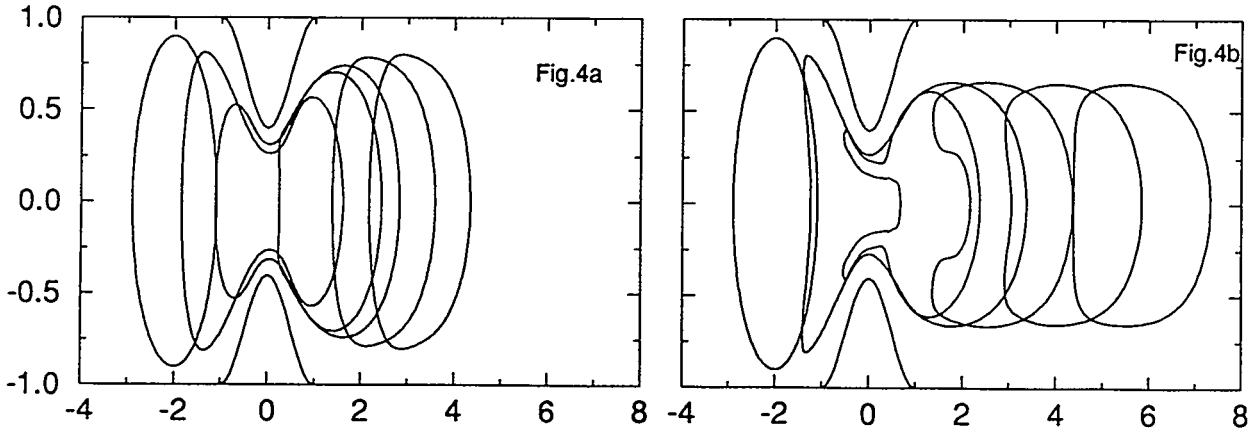

instability of a long bubble is observed. In Fig. 3b we set $Ca = 0.1$ with the same initial data as Fig. 3a. The pinching instability is still observed here but the bubble now moves downstream. Hence a snap-off can occur because of the initial data, so the results of any study of this instability will be very dependent on the initial data. In a random porous material one would think that any initial data is possible, so all of the observed phenomena should be possible.

Now consider the case of a constricted capillary. Suppose we replace the straight-walled part of the capillary, i.e., $h(z) = 1$, in the section $-L \leq z \leq L$ by the formula

$$h(z) = 1 - g\,[1.0 + \cos(\pi z/L)]\,. \tag{10}$$

This is the same perturbation in capillary tube shape as used by Gauglitz and Radke [7]. It implies that the length of the constriction is $2L$ and the gap radius is $1 - 2g$. In Fig. 4 we set $L = 1$and $g = 0.3$, $\lambda = 0.1$ and $r_e = 0.9$. The initial data is plotted in the figures. In Fig. 4a we set $Ca = 0.1$. We see that the bubble is squeezed through the constriction and it approachs the same steady shape downstream of the constriction as in Fig. 2a. In Fig. 4b we set $Ca = 0.5$. We see that as the bubble passes under the constriction, the back of the bubble advances toward the front as in the straight tube case of Fig.2b with a larger Capillary number. In a straight tube, a re-entrant cavity is not expected in this case (see Martinez and Udell [5]). The reason for this re-entrant cavity is the presence of the constriction and downstream it will disappear. Hence the constriction enhances this deformation and can possibility introduce an instability. Although, not illustrated we should note that for all other variables being constant, we find that the bubble motion slows down as λ is increased.

A more interesting case is for a bigger bubble. In Fig. 5 we set $Ca = 0.1$, $\lambda = 0.1$ and $r_e = 1.77$. The initial bubble is placed upstream of the constriction, $g = 0.3$ and $L = 9.0$. We see that as the bubble passed through the constriction, a perturbation develops along the interface, downstream of the constriction. As time marches on, the perturbation moves along with the bubble front and does not appear to grow in size after an initial growth period. Finally we find that the perturbation disappears and the bubble passes through the constriction.

In Fig. 6 we set $Ca = 0.005$, $\lambda = 0.1$, $r_e = 1.77$, $g = 0.3$ and $L = 9.0$. For the initial data we took a bubble profile from Fig. 5, i.e., not spherical, which was almost entering the constriction. We see that downstream of the constriction the perturbation to the profile as noted in Fig. 5 is not observed. Hence decreasing the Capillary number does not enhance the instability. This is not surprising since the growth of disturbances along the bubble interface should be proportional to Ca^{-2}. Therefore if a disturbance is growing, it will take longer to grow. We also note that upstream of the constriction a disturbance along the interface is growing. This is due to the initial data having a thicker initial film along the wall than would otherwise be there for this value of Ca, if we had used the same initial data as used in Fig. 5.

In Fig. 7 we set $Ca = 0.1$, $\lambda = 0.1$, $r_e = 1.23$, $g = 0.3$ and $L = 9.0$. The initial data is the same as in Fig. 6 but with the back truncated in order to decrease the volume. Hence this is a problem similar to Fig. 5 except the bubble has a smaller volume. Here we again find that there is a perturbation of the interface downstream of the constriction. The dynamics is similar to that of Fig. 5. Extrapolating from the experimental curves of Gauglitz and Radke [12] (this value of Ca is not on their figure), we can expect this bubble to snap-off. This was not observed here. A larger bubble or other values of the parameters may lead to snap-off for this initial data. Calculations are now being done to try and verify this remark. Here we have shown that different initial data can lead to snap-off.

Fig.5 Large Bubble in Constricted Capillary with Ca=0.1

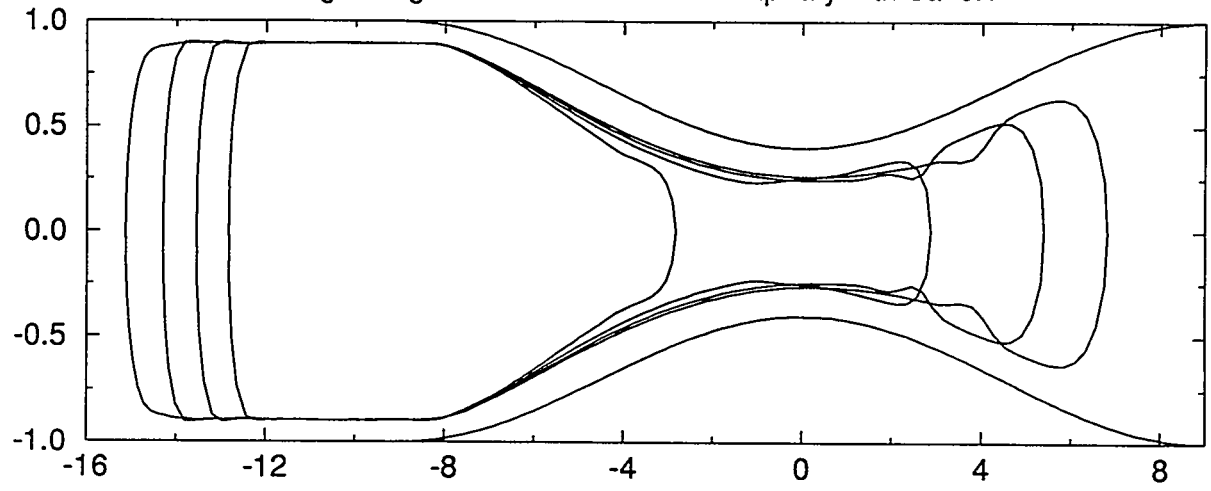

Fig.6 Large Bubble in Constricted Capillary with Ca=0.005

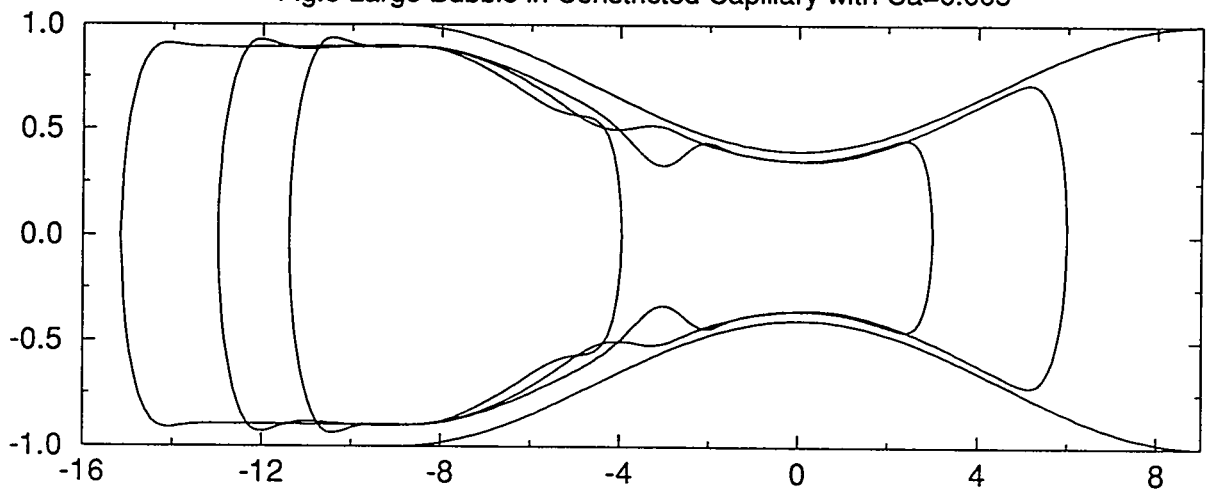

Fig.7 Large Bubble in Constricted Capillary with Ca=0.1

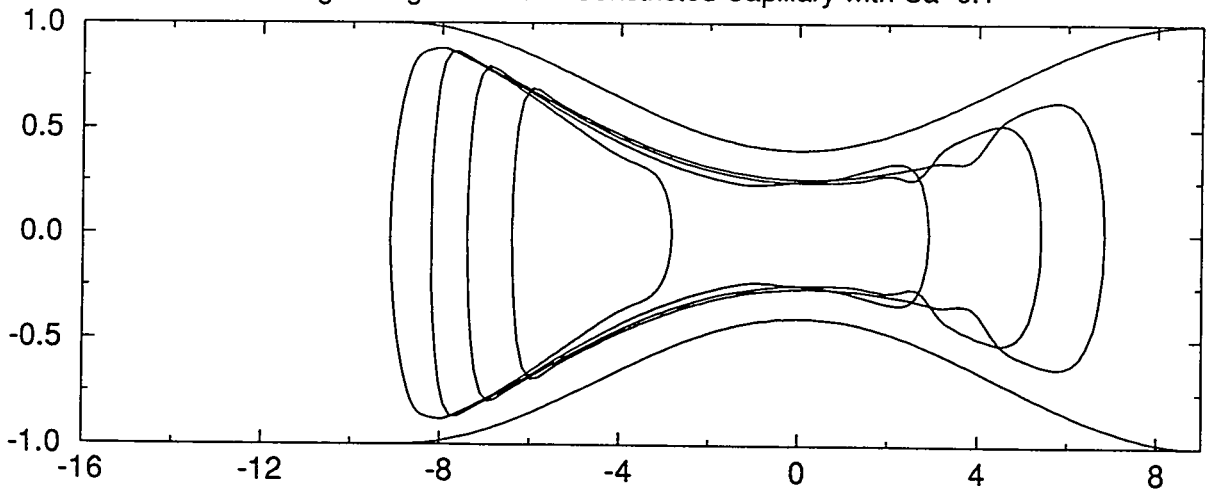

Acknowledgement

This research was supported in part by Department of Energy grant DE-FG02-88ER13927.

References

[1] F. P. Bretherton, "The Motion of Long Bubbles in Tubes", *J. Fluid Mech.*, 10, 166, (1961).

[2] C.-W. Park and G.M. Homsy, "Two-phase Displacement in Hele Shaw Cells: Theory", *J. Fluid Mech*, 139, 291, (1984).

[3] L.W. Schwartz, H.M. Princen and A.D. Kiss, "On the motion of Bubbles in Capillary Tubes", *J. Fluid Mech*, 172, 259, (1986).

[4] D.A. Reinelt and P.G. Saffman, "The Penetration of a Finger into a Viscous Fluid in a Channel and Tube", *SIAM J. Sci. Statist. Comput.*, 6, 542, (1985).

[5] M.J. Martinez and K.S. Udell, "Axisymmetric Creeping Motion of Drops Through Circular Tubes", *J. Fluid Mech.*, 210, 565, (1990).

[6] C. Pozrikidis, "The Buoyancy-Driven Motion of a Train of Viscous Drops Within a Cylindrical Tube", *J. Fluid Mech.*, 237, 627, (1992).

[7] P.A. Gauglitz and C.J. Radke, "The Dynamics of Liquid Film Breakup in Constricted Cylindrical Capillaries", *J. Colloid Interface Sci.*, 134, 14, (1990).

[8] T.-M. Tsai, Ph.D. Thesis, Department of Engineering Sciences and Applied Mathematics, 1993.

[9] T.-M. Tsai and M.J. Miksis, "Transient motion of Bubbles and Drops is Constricted Capillaries", in preparation.

[10] J.M. Rallison and A. Acrivos, "A Numerical Study of the Deformation and Burst of a Viscous Drop in an Extensional Flow", *J. Fluid Mech.*, 89, 191, (1978).

[11] C. Pozrikidis, *Boundary Integral and Singularity Methods for Linearized Viscous Flow*, Cambridge University Press, (1991).

[12] P.A. Gauglitz, C.M. St. Laurent and C.J. Radke, "Experimental Determination of Gas-Bubble Breakup in a Constricted Cylindrical Capillary", *Ind. Eng. Chem. Res.*, 27, 1282, (1988).

EVOLUTION OF LONG WAVE DISTURBANCES IN HORIZONTAL GAS-LIQUID FLOWS

W. C. Kuru, E. D. Montalbano, J. F. Brennecke and M. J. McCready

Department of Chemical Engineering
University of Notre Dame

ABSTRACT

Coherent nonlinear interactions between linearly stable, long wavelength modes and modes that are near the peak of the growth rate are observed in experiments. These "side-band" interactions are suggested as the mechanism for initiation of long wavelength modes that are otherwise predicted to be stable from linear stability theory. Quadratic interaction theory is used to provide insight into when long wavelength modes will appear and how their frequency will be selected. The present work differs from previous side band analyses in that a low frequency mode is retained as a dominant mode (consistent with observations). Because of its relevance to continued growth of long wavelength disturbances and possibly slug formation and owing to its importance in modeling flow regime transitions, a discussion of the validity of the one-dimensional macroscopic equations and the boundary-layer equations as models of long wavelength disturbances for the two-layer stability problem is given in the context of laminar flow of a fluid over a solid wavy surface.

INTRODUCTION

Formation of slugs in gas-liquid flows is a much-studied problem which is as yet unresolved. The Taitel-Dukler [17] flow regime model predicts slugs for situations where system is unstable to a slightly modified Kelvin-Helmholtz instability. While the implications are that slugs form from long wavelength waves (consistent with earlier work by Kordyban and Ranov, [12] and Wallis and Dobson,[18]) the K-H model implicitly suggests that slugs form from relatively short waves as can be seen in figure 1. Also shown in figure 1 is the linear stability for the same situation predicted from the linearized Navier-Stokes equations, clearly the K-H model does not realistically describe two-layer instability. Lin and Hanratty [13] use integral momentum equations expected to describe the long wave region and find some agreement with data. However, it will be shown below that if their "macroscopic" or 1-dimensional equations are used to predict instability, they do not correctly capture the behavior of important destabilizing and stabilizing terms in the region of α somewhat greater than 0. Consequently, the linear stability calculation is in error and agreement with data must therefore be considered fortuitous. This problem not withstanding, recent works by Brauner and Maron [2],[3], Crowley et al.[6] and Barnea [1] continue to use 1-D equations as the basis for prediction of the transition between stratified and slug flow. Hanratty et al. [9] demonstrate that several mechanisms are responsible for slug formation; growth of long wave disturbances is reaffirmed as one of the mechanisms. Consequently, any linear or nonlinear instability theory starting with stratified flow can, at best, be considered only a sufficient condition for the observance of slugs. Recent measurements by Fan and Hanratty [7] demonstrate the existence of period-doubling in a horizontal pipe at conditions somewhat less severe than where slugs are observed. They suggest that this is a possible (nonlinear) origin of a long wavelength mode which could grow into a slug. Jurman et al. [11] note that a low frequency mode (i.e. much lower than a subharmonic) can be generated by nonlinear interactions of side-band modes of the fundamental. This is another mechanism that can generate a long wavelength mode which could evolve into a slug.

This paper examines several issues pertinent to the generation and spatial evolution of disturbances that are much longer in wavelength than the depth of the liquid or gas phases. The motivation is slug generation when it occurs by the growth of waves from a stratified layer. For the channel flow we are examining, roll waves serve as a good model for many of the properties of slugs and so these will be considered. First the existence of a low frequency peak which is coherent in phase with the fundamental peak (and therefore likely to be generated nonlinearly), is demonstrated. Second, the validity of the boundary-layer equations and the 1-D macroscopic equations as models for linear and nonlinear wave behavior is examined by looking at analytical solutions to single phase flow over a solid wavy

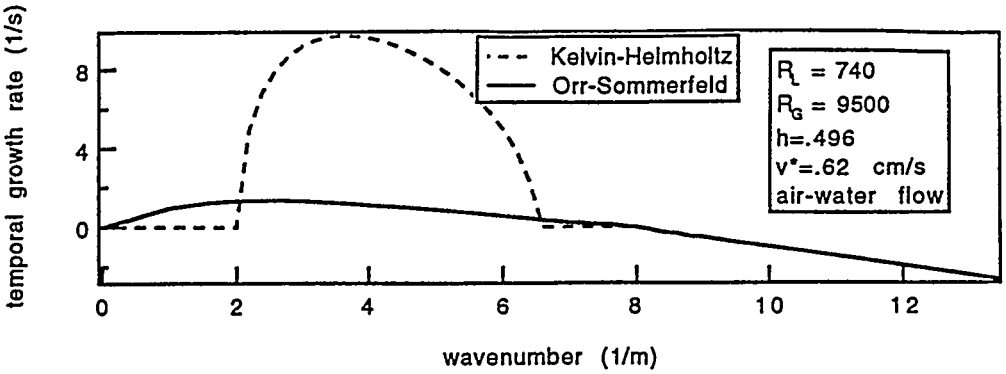

Figure 1. Comparison of Kelvin-Helmholtz (inviscid) with full linearized Navier-Stokes equations for air-water flow in a 2.54 cm high rectangular channel

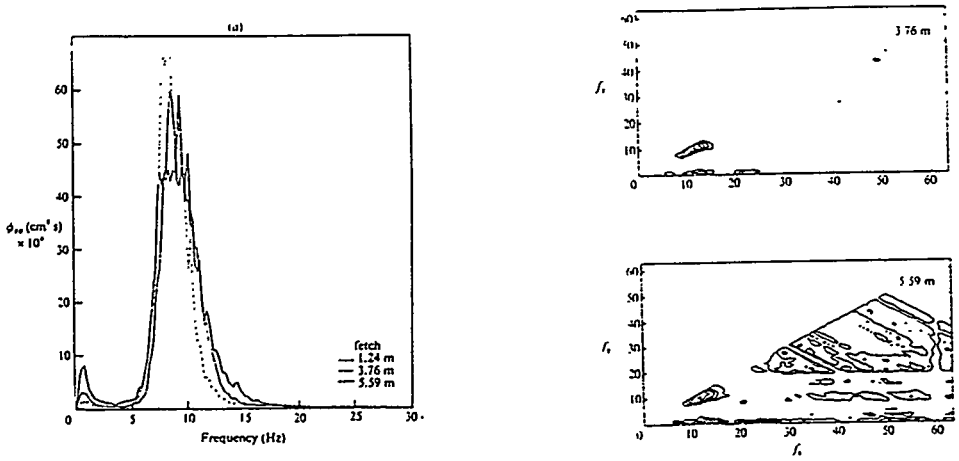

Figure 2. (from Jurman et al., 1992) Frequency spectra as a function of fetch and bispectra for the last two locations for $R_L = 5$, $R_G = 6300$, h=0.44 cm, $\mu_L = 20$ cP. The low frequency mode is observed to grow with distance. Contour lines at $f_2 = 1$, $f_1 = 10\text{-}15$ indicate that his mode is coherent with the main peak.

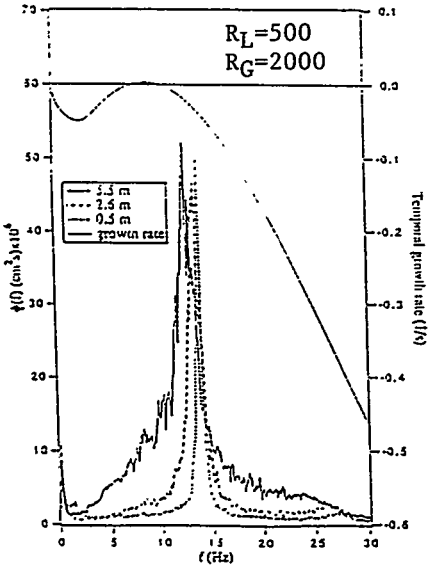

Figure 3a. Power spectra and growth rate

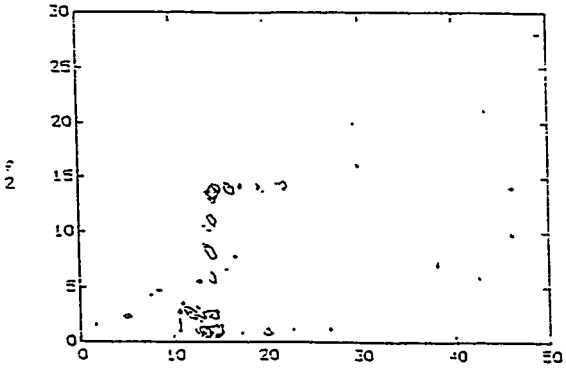

figure 3b. Bicoherence at 0.5 m for conditions of 3 a.

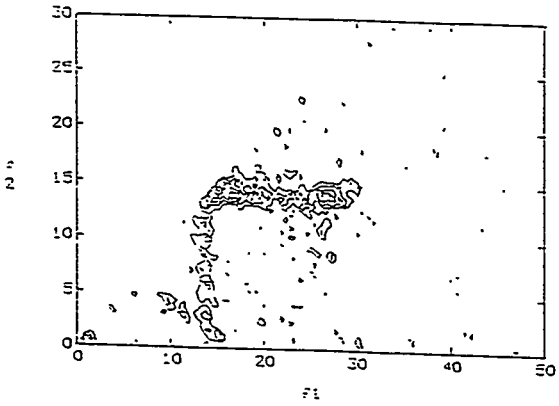

Figure 3c. Bicoherence at 2.6 m for conditions of 3a.

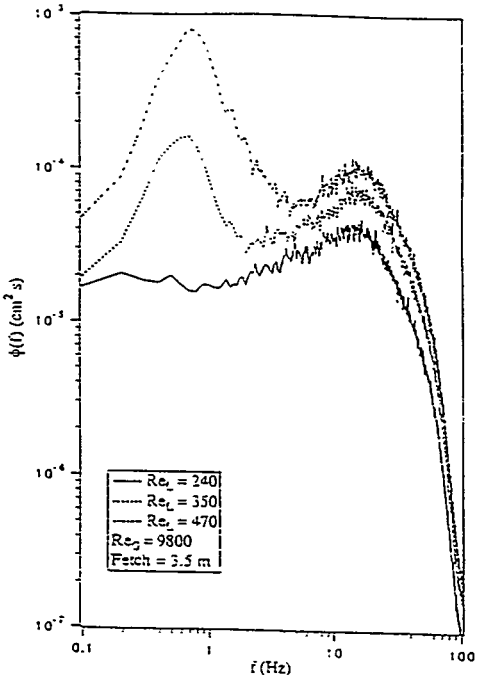

Figure 4a. Power spectra at increasing R_L showing roll wav precursor peak at .5 Hz

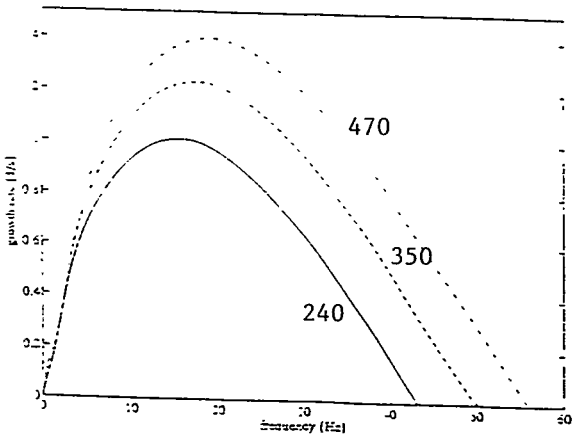

Figure 4b. Linear stability predictions for conditions of 4a.

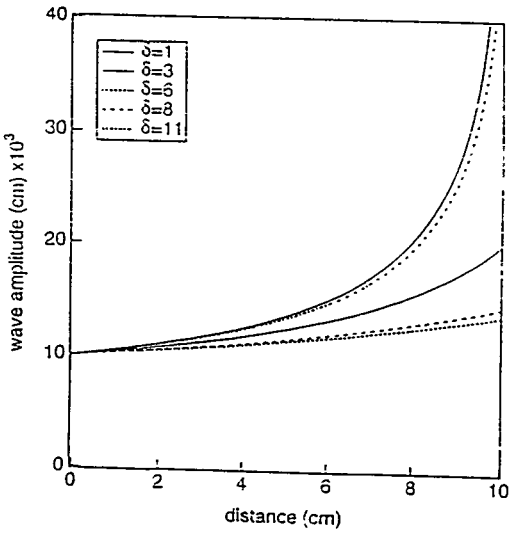

Figure 5. Amplitude of delta mode as a function of distance for different values of delta

surface. It is shown that the 1-D equations cannot be expected to work for most situations, but that the boundary-layer equations can be quite useful. Finally, the nonlinear generation of the low frequency mode is discussed with considerations to conditions that are too severe to be described rigorously.

OBSERVANCE OF LONG WAVELENGTH DISTURBANCES

Figure 2a shows data from Jurman et al. [11] for a sheared layer close to neutral stability, note that a small low frequency peak is present in the power spectrum. The bispectra (fig. 2b), show contours at f_1=10-12 and f_2=1 Hz suggesting that the low mode is coherent with modes around the peak. It is seen that both the strength of the interaction and the magnitude of this peak grow with distance. For this case, the long wavelength mode will not have any effect on the overall regime stability, even at very long distances, because the layer thickness is very small. Figure 3a shows new data for an air-water flow where the liquid Reynolds number is high enough for roll waves to form (given a high enough gas Re) but at Re_G close to neutral stability, along with the linear stability prediction of a two-layer laminar flow. The unfortunate discrepancy between the peak in the spectra and the fastest growing peak is due to a slight hydraulic gradient which exists at these low shear conditions; the error is not due to nonlinear effects. The important feature of the data is that the low frequency peak is coherent in phase with the fundamental as can be seen by the contour lines in the bicoherence spectra in figures 3b and 3c at f_1= 14, f_2=<1. Note that this peak is predicted to be *stable* from linear stability analysis and should not grow nor be phase coherent with the fundamental if only linear effects are important.

Figures 2 and 3 show low frequency modes that are clearly the result of nonlinear interactions between modes near the peak and a particular low frequency mode. These data are particularly intriguing because we have shown previously (Bruno and McCready, [4]), that roll waves emanate from continuous growth of a low frequency mode. Figure 4a shows data at a fixed location for three more severe conditions before roll waves where observed (i.e. either a longer distance or higher Re_G would be needed). Note that a low frequency peak is again present for two of the cases. From the linear stability prediction, figure 4 b(again using a 2-layer laminar flow), it is seen that all wavelengths are linearly unstable and the only peak is around 15-20 Hz. This suggests the question: What causes a low frequency peak to dominate and how is its frequency selected ?? Our previous arguments (Bruno and McCready, [4]) using two approximate linear theories that we spliced together are not consistent with the complete linear behavior shown in figure 4b.

It is certainly possible that this mode is initially excited by interactions with peak waves, similar to figures 2 and 3, and it gets larger because of the gas flow. If this is the case, the analysis used to describe the conditions close to neutral stability should provide insight into the roll wave formation problem. A second scenario is that nonlinear effects in the gas flow cause this mode to dominate. While there is no evidence to support this scenario, it should be given consideration in future studies.

COMPARISON OF DIFFERENT APPROXIMATE LINEAR STABILITY PROCEDURES USING FLOW OF A SINGLE PHASE FLUID OVER A WAVY SURFACE

To describe the formation of slugs starting with weakly nonlinear waves, a complete understanding of the behavior of the gas flow over long waves of increasing wave slope is needed. As a starting point for this work which will include weakly-nonlinear analysis (e.g. like Hooper and Grimshaw [10]) and numerical solution of the strongly nonlinear problem, we provide some analytical predictions from linear theories of the pressure and shear variations over waves.

None of the standard procedures for predicting slugs in gas-liquid flows use the Orr-Sommerfeld equation as a basis so it is worthwhile to determine the extent of their applicability. Because the linear stability problems for the simplified equations are still algebraically complex and difficult to compare, we examine the case of a single phase flow over a sinuous wavy surface centered around y=0. The different approximations are used to predict the components of the pressure and shear stress over the solid wavy surface.

Consider a rectangular channel with a sinuous wall centered around y=0. The wave number is $\alpha = 2\pi h/\lambda$, where h is the channel height and λ is the wavelength, the amplitude is assumed to be such that the wave slope is much less than 1. If the Navier-Stokes equations are linearized, the average pressure driven flow will be parabolic and the equation for the disturbance stream function, $\phi(y)$ is just the Orr-Sommerfeld equation with no wave velocity,

$$U(y)\left(\frac{d^2}{dy^2} - \alpha^2\right)\phi(y) - \phi(y)\frac{d^2U(y)}{dy^2} = \frac{1}{I\,\alpha\,R}\left(\frac{d^2}{dy^2} - \alpha^2\right)^2\phi(y) \cdot \qquad (1)$$

In this equation R is defined using the average velocity and the channel height, and U(y) is parabolic pressure driven flow velocity. The no slip boundary conditions are applied at the wave surface using domain perturbation. An exact analytical solution to eq. 1 is not available but because our only interest is the long wavelength region, we can generate a useful asymptotic solution for $\phi(y)$ is powers of α as,

$$\phi(y) = \phi_0(y) + \alpha\,\phi_1(y) + \alpha^2\phi_2(y) + \ldots \quad . \qquad (2)$$

When this is done and powers up to α^3 are kept, the perturbation shear stress, $\hat{\tau}$, defined as

$$\tau = \bar{\tau} + a\,\hat{\tau}\,\mathrm{Exp}[I\,\alpha\,x], \ (\text{at } y=0) \qquad (3)$$

is
$$\frac{\hat{\tau}}{\bar{\tau}} = 4 + \frac{I}{35}R\,\alpha + \frac{2}{8085}(R\,\alpha)^2 + \frac{4}{15}\alpha^2 + \frac{I}{105}R\,\alpha^3 - \frac{17\,I}{5659500}(R\,\alpha)^3 - \frac{17863}{63063000}R^2\alpha^4 - \frac{2792189}{54895395555000}(R\,\alpha)^4 + \frac{4}{1575}\alpha^4 \quad . \qquad (4)$$

The perturbation pressure, $\hat{p}$, is
$$\frac{\hat{p}}{\bar{p}} = \frac{36\,I}{R\,\alpha} - \frac{54}{35} + \frac{36\,I}{5\,R}\,\alpha + \frac{117\,I}{13475}R\,\alpha - \frac{57}{175}\alpha^2 + \frac{52\,I}{175\,R}\alpha^3 + \frac{1233}{12262250}(R\,\alpha)^2 + \frac{3202\,I}{525525}R\,\alpha^3 - \frac{33723827}{18298465185000}(R\,\alpha)^3 \ . \qquad (5)$$

It is interesting to note that as $\alpha \to 0$, the largest pressure term is out of phase with the wave height and the largest shear stress term is in phase with the wave height.

If the Reynolds number is sufficiently large a useful approximate solution can be obtained by a boundary-layer simplification of 1. The resulting equation cannot be solved analytically, but it does yield to a series solution around y=0. If a sufficiently large number of terms are kept in the series, the results are
$$\frac{\hat{\tau}}{\bar{\tau}} = 4 + \frac{I}{35}R\,\alpha + \frac{2}{8085}(R\,\alpha)^2 - \frac{17\,I}{5659500}(R\,\alpha)^3 - \frac{2792189}{54895395555000}(R\,\alpha)^4 \qquad (6)$$
and
$$\frac{\hat{p}}{\bar{p}} = \frac{36\,I}{R\,\alpha} - \frac{54}{35} + \frac{117\,I}{13475}R\,\alpha + \frac{1233}{12262250}(R\,\alpha)^2 - \frac{33723827}{18298465185000}(R\,\alpha)^3 \ . \qquad (7)$$
All of the $(R\,\alpha)^n$ terms match exactly, however none of the other terms are generated. Thus, if $\alpha < 0.1$, and $R > 10$, the solutions are effectively identical. There is an upper limit on αR, probably about $O(10)$.

A final approximate solution is to use the macroscopic equations used by Lin and Hanratty [13] which for this calculation are identical to the 1-D equations used by Crowley et al. [6] and Brauner and Maron [2],[3]. Only one term can be obtained for the pressure and shear stress. Because the y-direction is integrated out of the problem, these equations cannot provide a *prediction* for the disturbance shear stress. However, the pressure perturbation is
$$\frac{\hat{p}}{\bar{p}} = \frac{36\,I}{R\,\alpha} - \frac{6}{5}, \qquad (8)$$
no higher terms can be produced. The first term is exact and the second term is not too bad, but without the inclusion of any more terms, and no perturbation shear stress, this model is not likely to provide a realistic prediction of the stability of a two-layer flow and therefore slug formation !!

THEORETICAL BASIS FOR LOW FREQUENCY MODES

While it is not known *apriori* why the dominant observed modes are f=δ and the fundamental, we begin our analysis by assuming this to be the case. Our goal is to determine the conditions under which the low mode is predicted to be present. The behavior of a weakly sheared liquid layer close to neutral stability is expected to be well-described by the weakly-nonlinear, weakly-viscous theory of Jurman et al. [11] if the parameter αR is sufficiently large. For the data of fig. 3, αR is 760 for fundamental and about 5 for the δ mode. For these conditions, the delta mode is a high enough wavenumber that the "low mode" wave equation recently-derived by Renardy and Renardy [14] will probably not be valid. Previous work on side band stability (Cheng and Chang, [5]) is also not expected to describe this problem because of the omission of the low frequency mode. Starting with the spatial quadratic equations for l = δ, 2δ, 1-δ, 1 1+δ and 2 modes (only terms which will contribute to final equations are shown),

$$U_\delta \frac{\partial A_\delta}{\partial x} = \lambda_\delta A_\delta + (P_{1,\delta} A_1 A^*_{1-\delta} + P_{1+\delta,\delta} A^*_1 A_{1+\delta} + P_{2\delta,\delta} A^*_\delta A_{2\delta}) \quad (9a)$$

$$U_{2\delta} \frac{\partial A_{2\delta}}{\partial x} = \lambda_{2\delta} A_2 + Q_{\delta,2\delta} A_\delta A_\delta \quad (9b)$$

$$U_{1-\delta} \frac{\partial A_{1-\delta}}{\partial x} = \lambda_{1-\delta} A_{1-\delta} + P_{1,1-\delta} A^*_\delta A_1 \quad (9c)$$

$$U_1 \frac{\partial A_1}{\partial x} = \lambda_1 A_1 + (P_{1+\delta,1} A_{1+\delta} A^*_\delta + Q_{\delta,1} A_\delta A_{1-\delta} + P_{2,1} A^*_1 A_2) \quad (9d)$$

$$U_{1+\delta} \frac{\partial A_{1+\delta}}{\partial x} = \lambda_{1+\delta} A_{1+\delta} + Q_{\delta,1+\delta} A_1 A_\delta \quad (9e)$$

$$U_2 \frac{\partial A_2}{\partial x} = \lambda_2 A_2 + Q_{1,2} A_1 A_1 \quad (9f)$$

where U_l is the group velocity of mode l, A_l is the complex amplitude assumed to be a function only of x, the flow direction, λ_l is the complex (temporal growth rate), the P's and Q's are the interaction coefficients for a weakly viscous sheared layer given by Jurman et al. [11] and * denotes complex conjugate. Eq's (1) can be easily integrated numerically (as can a very large set), but this will not be done here. To uncover the nature of the interactions that lead to the low frequency mode, we will proceed analytically using center manifold theory (Guckenheimer and Holmes, [8]). Because the 2 δ mode is not observed experimentally and has a negative growth rate, thus it will be projected away. The 2 mode, which is the overtone of the fundamental is confined to small amplitudes and has a very negative growth rate and therefore it will also be projected away. It is harder to justify projecting the 1+δ and the 1 - δ modes. These have positive growth rates unless δ is rather large and while they are not seen as distinct from the main peak, could be contained in it. These will be projected away in this analysis to allow for some conclusions regarding the behavior of the δ mode. The consequences of this perhaps unjustifiable projection will be discussed below. The two projected equations are

$$U_\delta \frac{\partial A_\delta}{\partial x} = \lambda_\delta A_\delta - \frac{P_{1+\delta\,\delta} Q_{\delta\,\delta+1} U_\delta U_1}{-\lambda_\delta U_1 U_{\delta+1} + \lambda_{\delta+1} U_1 U_\delta - \lambda_1 U_\delta U_{\delta+1}} A_1 A^*_1 A_\delta +$$
$$\mathrm{Conj}\left(\frac{-P_{1\,\delta} P_{1\,1-\delta} U_\delta U_1}{-\lambda^*_\delta U_1 U_{\delta-1} + \lambda_{\delta-1} U_1 U_\delta - \lambda_1 U_\delta U_{\delta-1}} A_1 A^*_1 A^*_\delta\right) + \frac{P_{2\delta\,\delta} Q_{\delta\,2\delta}}{\lambda_{2\delta} U_\delta - 2\lambda_\delta U_{2\delta}} A_\delta A^*_\delta A_\delta \quad (10a)$$

$$U_1 \frac{\partial A_1}{\partial x} = \lambda_1 A_1 - \left(\frac{P_{1+\delta\,1} Q_{\delta\,\delta+1} U_\delta U_1}{-\lambda_\delta U_1 U_{\delta+1} + \lambda_{\delta+1} U_1 U_\delta - \lambda_1 U_\delta U_{\delta+1}} +$$
$$\frac{Q_{\delta\,1} P_{1\,1-\delta} U_\delta U_1}{-\lambda^*_\delta U_1 U_{\delta-1} + \lambda_{\delta-1} U_1 U_\delta - \lambda_1 U_\delta U_{\delta-1}}\right) A_1 A_\delta A^*_\delta + \frac{P_{21} Q_{12}}{\lambda_2 U_1 - 2\lambda_1 U_2} A_1 A^*_1 A_1 \quad (10b)$$

These are already in the "double-Hopf" normal form (G&H [8]) as can be seen if they are written in polar form,

$$\frac{d\, r_\delta}{dx} = \mu_\delta r_\delta + a_{11} r_\delta^3 + a_{12} r_\delta r_1^2 \quad (11a)$$

$$\frac{d\, r_1}{dx} = \mu_1\, r_1 + a_{21}\, r_\delta{}^2 r_1 + a_{22}\, r_1{}^3 \qquad (11b)$$

where r_δ and r_1 are the real amplitudes of δ and 1 modes. The coefficients a_{ii} are the real parts of the corresponding coefficients from eqs 10, and $\mu_1 = \text{Real}(\lambda_1/U_1)$. These are substantially simpler than eqs 10 because the phase angles and amplitudes are decoupled to this order. Eqs. 11 can be transformed to reduce the number of coefficients into the form

$$\frac{d\, r_\delta}{dx} = \mu_\delta\, r_\delta + \quad r_\delta{}^3 + b\, r_\delta\, r_1{}^2 \qquad (12a)$$

$$\frac{d\, r_1}{dx} = \mu_1\, r_1 + c\, r_\delta{}^2 r_1 + d\, r_1{}^3 \cdot \qquad (12b)$$

A table of values for b,c and d are given below. Note that d is always <0, therefore the fundamental is supercritical. However, the δ mode is subcritical.

Table 1

Coefficients for Equations (12) for different values of δ

δ (1/m)	μ_1	μ_2	b	c	d
1	-.0043	.000944	.000918	25227	-1
2	-.00515	.000944	.00131	4934	-1
3	-.00594	.000944	.00288	1617	-1
4	-.00670	.000944	.00167	646.6	-1
5	-.00734	.000944	.00169	310.9	-1
6	-.00796	.000944	.004	166.0	-1
8	-.00899	.000944	.00262	59.9	-1
11	-.0103	.000944	.00197	18.4	-1

DISCUSSION

Results of the integration of eqs. (12) for several different values of δ are shown in figure 5. It is seen that the δ mode always grows with distance even though it is linearly stable. It is interesting that the rate of growth varies depending upon the value of δ. Consequently, one contribution to the value of δ is probably determined by its initial growth rate. This criterion does not work exactly for the case of fig. 3, where the value of δ= 2/m corresponds to .1 Hz, would not be quite the one with the largest predicted initial growth.

Two other issues are important here. First is the effect of initial conditions. We have reported previously (Sangalli et al., [16]) that the fundamental wave number is selected to some extent by the noise present at the initial gas-liquid contact point, although the effect is likely to cause a distribution of values around the preferred value. Therefore, the value of δ must also be influenced in this way. Secondly, recall that we have assigned values for the 1+ δ and 1-δ modes as $O(r_1{}^2)$. In the real system this may not be true and the *amplitudes* of the 1+ δ and 1-δ modes may also be important. If we consider the case that these modes have amplitudes of order r_1 then it will, of course, not be possible to use center manifold theory to transform away these modes. However, if this is the case, a second kind of approximation is tempting. We could recognize that $A_{1-\delta}$ and $A_{1+\delta} \approx A_1$. This would give terms like $A_1 A^*_1$ in the delta equation. When the two quadratic equations are transformed into the normal form (12), the same $r_\delta\, r_1{}^2$ term appears with a similar coefficient. Consequently, the assumption about the magnitudes of the sideband modes may not be too crucial.

Finally, if it is necessary to do analysis for more severe conditions, such as fig. 4, it may be reasonable to assume that the same type of qualitative picture exists. However, it will be necessary to use eqs (12) as a model with coefficients determined (perhaps) by experiment.

ACKNOWLEDGEMENT

This work has been supported by the U.S. Department of Energy under Grant DOE FG02-88ER13913.

REFERENCES

1. Barnea, D. On the effect of viscosity on stability of stratified gas-liquid flow—application to flow pattern transition at various pipe inclinations. *Chem. Eng. Sci.* 46, 2123 (1991).
2. Brauner, N. & D. M. Maron " Analysis of stratified/nonstratified transitional boundaries in horizontal gas-liquid flows", *Chem. Eng. Sci.* 46, 1849 (1991).
3. Brauner, N. & D. M. Maron Stability analysis of stratified liquid-liquid flow. to appear: *Int. J. Mult. Flow.* (1992)
4. Bruno, K. & McCready, M. J. " Origin of roll waves in gas-liquid flows", *AIChE J.* 34 1431 (1988).
5. Cheng, M. and H. -C. Chang, "A generalized side-band theory via center manifold projection", *Phys. Fluids* A 2, 1364 (1990).
6. Crowley, C. J., G. B. Wallis and J. J. Barry (1992) Validation of a one-dimensional wave model for the stratified to slug flow regime transition, with consequences for wave growth and slug frequency. to appear *Int. J. Mult. Flow* .
7. Fan and T. J. Hanratty preprint (1992)
8. Guckenheimer J. and P. Holmes *Nonlinear oscillations, Dynamical Systems and Bifurcations of vector fields.* Springer (1983).
9. T. J. Hanratty , V. Bontozoglou and N. Adritsos. "Theories on the initiation of slug flow", *Proc. Seventh Symp. Energy Eng. Sci.* (1989)
10. A. P. Hooper and R. Grimshaw, "Nonlinear instability at the interface between two viscous liquids", *Phys. Fluids*, 28 37 (1985).
11. L. A. Jurman, S. E. Deutsch, S. E. and M. J. McCready,"Interfacial mode interactions in horizontal gas-liquid flows", *J. Fluid Mech.* 238, 187 (1992).
12. E. S. Kordyban and T. Ranov, "Mechanism of slug formation in horizontal two-phase flow", *J. Basic Engng.*, 92, 857 (1970).
13. P. Y. Lin and T. J. Hanratty, "Prediction of the initiation of slugs with linear stability theory", *Int. J. Mult. Flow,* 12, 79 (1986) .
14. Y. Renardy, and M. Renardy "Sideband instabilities in two-layer flows" preprint (1993)
15. Y. Renardy, "Weakly nonlinear behavior of periodic disturbances in two-layer Couette-Poiseuille flow", *Phys. Fluids* A 1 1666 (1989).
16. M. Sangalli, Th. Prokopiou, M. J. McCready and H. -C. Chang, "Observed transitions in two-phase stratified gas-liquid flow", *Chem. Eng. Sci.*, 47, 3289, (1992).
17. Y. Taitel. and A. E. and Dukler, "Model for predicting flow regime transitions in horizontal and near horizontal gas-liquid flow", *AIChE J.* 22, 47 (1976).
18. G. B. Wallis and J. E. Dobson, The onset of slugging in horizontal stratified air-water flow", *Int. J. Mult. Flow* , 1 173 (1973)
19. S. G. Yiantsios and B. G. Higgins,"Linear stability of plane Poiseuille flow of two superposed fluids", *Phys. Fluids* A 31, 3225 (1988).

FUNDAMENTAL ASPECTS OF BRITTLE DAMAGE PROCESSES - DISCRETE SYSTEMS

D. Krajcinovic and V. Lubarda

Mechanical and Aerospace Engineering
Arizona State University, Tempe AZ 85287-6106, USA.

ABSTRACT

The analysis of cooperative brittle processes are performed on simple discrete models admitting closed form solutions. A connection between the damage and fracture mechanics is derived and utilized to illustrate the relation between two theories. The performed analyses suggest that the stress concentrations (direct interaction between defects) represent a second order effect during the hardening part of the response in the case of disordered solids.

INTRODUCTION

The evolution of damage in disordered microstructures is obviously not a simple, deterministic process admitting careless application of conventional continuum models formulated originally for the considerations of ductile phenomena. In general, crack growth will commence when the available elastic energy release rate exceeds the material toughness at the crack tip. Hence, the damage evolution (defined here as formation of new internal surfaces in the material through the process of cracking) depends on the coincidence of local stress concentrations (hot spots) and regions of inferior toughness (weak links) of the microstructure. Fracture toughness is a random function of coordinates and its scatter depends on the material itself, previous history and defects attributable to manufacturing processes. The energy release rate for the observed crack is an integrated quantity which depends on the adjacent microdefects and microstructure. In the case of many microcracks estimates of their individual growth are quantified by the change in a continuum measure of damage representing expectations of the growth of the entire ensemble of microcracks. In order to be useful this measure must be physically identifiable and measurable in tests.

PARALLEL BAR MODEL

Analytical modeling of processes involving evolution of damage is fraught by pitfalls and open to ambiguity. For the most part the depth of these pitfalls is proportional to the inherent complexities of the cumbersome mathematical structure of non-deterministic models which claim both rigor and generality. A bevy of different continuum damage models, often pretentious and seldom rigorous [1], is a testimony to this state of affairs.

As a result of the inherent complexity of the problem and the contradicting requirements of rigor and simplicity the analytical representation of the damage and its evolution is not unique. To clarify some of the fundamental aspects of the physics of the deformation process dominated by the cooperative action of microdefects it is advisable to reduce the mathematical complexities by concentrating on simplified analytical models. Simplification in modeling is typically achieved through discretization of a solid. Simulations of brittle deformation processes in disordered media are often performed on discretized networks consisting of nodes interconnected by links. The mechanical properties of the links can be quite general incorporating complex, time dependent stiffnesses and rupture criteria.

The parallel bar system is the simplest computational artifice which is typically employed when both the specimen and the load diffusion pattern are essentially unidirectional. This rather simple and attractive artifice was extensively and successfully applied in the past to the studies of both ductile [2,3] and brittle [4,5] phenomena. For certain geometries and materials the selection of the parallel bar model is fully justified by the structure of the material itself. Cables containing many parallel strands or fibers and polymeric matrices reinforced by strong continuous fibers are the two most obvious examples. In other cases the microstructure of a material and the failure mode render the parallel bar model a viable alternative. The distribution of the external force to individual links may be democratic (each link shares equally in carrying the external loads) or follow a local load sharing rule. The democratic (loose bundle) parallel bar models entirely ignore the stress concentrations (spatial correlations). Thus, by assuming that the failure is controlled exclusively by the distribution of weak links this model belongs to the group of the "infinite disorder" models.

Consider first the simplest approximation [4,5] of a perfectly brittle solid by a loose bundle parallel bar system assuming that:

- all extant links share equally in carrying the external tensile load F regardless of their position within the system,
- all N links have identical stiffness $k = K/N$ and elongation u,
- all links remain linearly elastic until rupture, and
- the rupture strength f_r of links is a random variable defined by a prescribed probability density distribution $p(f_r)$.

These assumptions eliminate from considerations all spatial interactions. The exact position of each particular link is assumed to have no effect on the macro-response. Consequently, the macro-response (measured by the system displacement u) depends only on the fraction of ruptured bars (n/N) and not on their location. The above listed assumptions eliminate the size effect since the response depends only on the fraction of the ruptured bars. The absence of the length parameter renders the theory local.

Application of a loose bundle parallel bar system implicitly assumes that the damage evolution and ultimately the failure is attributable primarily to the existence of the regions of inferior toughness within the material. Local stress concentrations are assumed to have a second order effect on the structural response. In view of the assumptions listed above the parallel bar model is the discrete version of the popular self consistent model. Thus, the loose bundle parallel bar model is an *infinite disorder* system. Link forces are equal and the failure occurs solely as a result of the microstructural disorder, i.e. the rupture strength distribution $p(f_r)$.

During the deformation of the system subjected to a quasi-statically incremented external tensile load F the tensile forces in individual links f_i (i = 1 to N) keep increasing. When the force f_i in the i-th link exceeds its strength f_{ri} link ruptures and releases its force. The released force is distributed quasi-statically and equally (democratically) to all extant links. The sequential rupture of individual links slowly degrades the stiffness and the load bearing capability of the system. On the system scale rupture of individual links can be measured as a gradually decrease of the effective stiffness.

The equilibrium of the system requires that

$$F = \sum_{i=1}^{N} f_i = Ku\left(1 - \frac{n}{N}\right) = Ku(1 - D) \tag{1}$$

where n is the number of ruptured links at a given magnitude of the externally applied tensile force F. On the micro-scale number of ruptured links n suffices to define the recorded history. The fraction of ruptured links

$$D = \frac{n}{N} \tag{2}$$

is a physically appealing measure of the recorded history (i.e. the accumulated damage) on the macro-scale. In absence of plastic strains, parameter D defines the state of the material and quantifies the level of degradation of the material stiffness and, perhaps, even the residual load bearing capability. Deformation of the system is defined by two kinematic variables: u and D. The loose bundle parallel bar model makes no distinction between the case when all n ruptured links are adjacent to each other from the case when they are dispersed. Model provides no information regarding the maximum defect size. This is consistent with the statement that the considered model belongs to the class of traditional effective continua models. Failures caused by the critical size of the largest defect (Griffith's instability) or localization cannot be predicted by this class of models.

For a very large number of links N a given property can be treated as being equal to its expectation. The equilibrium equation (1) can be then rewritten in the form of an integral

$$F = ku\left\{N\int_{ku}^{f_{max}} p(f_r)df_r\right\} = K(1-D)u \tag{3}$$

where f_{max} is the strength of the strongest link. The bracketed term in (3) represents the number of the load carrying links. The expression for the damage parameter D is from above

$$D = \int_{f_{min}}^{ku} p(f_r)df_r = prob.(f_r < ku) = P(ku) \tag{4}$$

Statistically, the damage parameter can be interpreted as the cumulative probability function P(ku) of the given rupture strength probability density function p(f_r). In (4) f_{min} is the rupture strength of the weakest link. Expression (4) represents the damage evolution law, i.e. the constitutive relation relating the rates at which the damage and elongation increase. The incremental form of (4) is

$$dD = p(ku)\,k\,du = p(u)\,du\,. \tag{5}$$

Therefore, once the distribution of rupture strengths p(f_r) on the microscale is known, the damage evolution law can be derived in contrast to being *a priori* and arbitrarily postulated.

Thermodynamic Considerations: The energy E used to rupture the links is equal to the difference between the mechanical work W of the externally applied tensile force F on the displacement u and the energy of elastic deformation U that would be released in the course of subsequent unloading, i.e.

$$E = W - U = \int_o^u Fdu - \frac{1}{2}Fu \tag{6}$$

Numerically the energy E is equal to the area contained within the loading (ascending) and unloading (descending) segments of the force-displacement curve.

Consider the Helmholtz free energy of the system $\Phi = \Phi(u,D,T)$. Restricting considerations to isothermal processes, the rate of change of the free energy of the system, loaded by a monotonically increasing tensile force F, can be written using the first law of thermodynamics in the form suggested in [6]

$$\dot{\Phi} = F\dot{u} - T\Lambda \tag{7}$$

where $\Lambda \geq 0$ is the irreversible entropy production rate.

The free energy is selected to be equal to zero in the initial, unruptured and unloaded state ($D=0$, $F=0$). The free energy of a state defined by some load $F>0$ and damage $D>0$ is then equal to the work done in transforming the body from its initial to current state along an imagined reversible and isothermal path. Thermodynamic analysis of the quasi-static growth of Griffith cracks in a loaded state in which at least some of the links are ruptured ($D>0$), can be considered [6] as consisting of an imagined sequence of two steps. In the first step, $n=DN$ links are ruptured quasi-statically pulling against the cohesive forces bonding together two adjacent layers of atoms. In the second step, the extant links are elastically stretched until the requested state of deformation u has been reached. The work associated with the described sequence of two steps is

$$\dot{\Phi} = F\dot{u} - T\Lambda \qquad \text{where} \qquad E_\gamma = 2A\int_{\gamma_{min}}^{\gamma_r} \gamma_r p(\gamma_r)d\gamma_r \tag{7}$$

Thus, E_γ is the energy of free surfaces created by rupturing n links, while γ_r is the link dependent specific surface energy. In (7.b) A denotes the initial unruptured cross sectional area of the system. The linear elastic fracture mechanics suggests that the surface energy is a quadratic function of the force in the link at its rupture. Assuming that a fraction λ of the energy is used for new internal surfaces the expression (7.b) can be manipulated into the following form [5]

$$E_\gamma = \frac{2\lambda A}{4kA_r} \int_{\gamma_{min}}^{\gamma_r} f_r^2 p(f_r) df_r \tag{8}$$

where A_r is the surface area of ruptured links. Since $ku = f_r$, the fracture (surface) energy density is

$$\gamma_r = \frac{\lambda}{4kA_r} f_r^2 \tag{9}$$

Assume uniform distribution of link rupture strengths $p(f_r) = \Delta f^{-1}$ where $\Delta f = f_{max} - f_{min}$. The damage-displacement relationship is from (4)

$$D = \frac{ku - f_{\min}}{\Delta f} \tag{10}$$

The expression for the entropy production rate can be finally derived [5] using the equilibrium equation in the following form

$$T\Lambda = \left(\frac{1}{2}Ku^2 - 2A\gamma_r\right)\dot{D} \tag{11}$$

Equation (11), in conjunction with the second law of thermodynamics (requirement of the non-negative entropy production rate $\Lambda \geq 0$), leads to the inequality

$$(\Gamma - R)\dot{D} \geq 0 \tag{12}$$

where the thermodynamic forces driving and resisting the damage evolution are

$$\Gamma = -\frac{\partial U}{\partial D} = \frac{1}{2}Ku^2 \qquad \text{and} \qquad R = 2A\gamma_r \tag{13}$$

Inequality (12) is a discrete analogue of the Griffith's condition as generalized by Rice [7]. According to (12) the condition $\Gamma - R \geq 0$ must be satisfied for the damage to grow $\dot{D} \geq 0$ Conversely, healing *may* take place only if the resistive force exceeds the force driving link rupture. Inequality (12) places a restriction $\lambda \geq 1$ on the energy partition parameter. If the entire energy used in the deformation process is transformed into the surface energy it follows that $\lambda = 1$ and $\Gamma = R$..

<u>Conjugate Measures of Damage and Associated Affinities</u>. The rate of energy used in the course of the sequential link rupturing process (or damage evolution) is from (6)

$$\dot{E} = \dot{W} - \dot{U} = \left(F - \frac{\partial U}{\partial u}\right)\dot{u} - \frac{\partial U}{\partial D}\dot{D} = \Gamma\dot{D} \tag{14}$$

Since $F = \partial U/\partial u$, as shown in [5]

$$\Gamma dD = \frac{1}{2}Ku^2 dD = \frac{1}{2}ku^2 dn \tag{15}$$

The smallest increment of damage dD is associated with the rupture of a single additional link ($dn = 1$). Thus, the product ΓdD is the elastic energy of link ($ku^2/2$) released when a single link ruptures.

The suggested definition (4) of the damage variable is not unique. A different damage variable may be defined relating its rate of change to the current number of the unruptured links $(N-n)$

$$\dot{D}_n = \frac{\dot{n}}{N-n} \qquad \text{such that} \qquad D_n = \ln\left(\frac{N}{N-n}\right) \tag{16}$$

In analogy with the strain measure commonly used in the theory of plasticity, damage variable (16) can be referred to as a logarithmic measure of the damage. Since $0 \le n \le N$, it follows that $0 \le D_n \le \infty$. In contrast, previously introduced damage variable $D=n/N$ is defined in the interval $0 \le D \le 1$. Two measures of damage D and D_n are related as

$$D_n = -\ln(1-D) \qquad \text{and} \qquad D = 1-\exp(-D_n) \tag{17}$$

The relation between the two damage rates, Langrangian and Eulerian damage parameters and their expressions in terms of the initial and current cross-sectional areas are derived in [5].

The Damage Resistance Curve. The stability of the damage growth can be investigated considering the energy balance. An alternative method for the examination and interpretation of the stability of damage growth takes advantage of the damage resistance curve, in analogy to the well known resistance (R --curve) of fracture mechanics. Consider first the potential energy in a force controlled test defined by expression

$$\Pi_f(F,D) = \pi_f(F,D) + E_\gamma(D) = -\frac{F^2}{2(1-D)K} + \frac{8F_m^2}{3K}D^3 \tag{18}$$

where $\pi_f(F,D)$ represents the sum of the elastic strain energy and the load potential, while $E_\gamma(D)$ is the surface energy (8). The energy release rate associated with the damage growth is

$$G(F,D) = -\frac{\partial \pi_f}{\partial D} = \frac{F^2}{2(1-D)^2 K} \tag{19}$$

The thermodynamic force resisting the damage increase is

$$R(D) = \frac{dE_\gamma}{dD} = \frac{8F_m^2 D^2}{K} \tag{20}$$

For a given value of the force F, the accumulated damage is obtained from the equilibrium requirement

$$G(F, D) = R(D) \ , \tag{21}$$

The corresponding state is one of stable damage growth if, for a given force level, the rate of damage resistance force exceeds the rate at which the energy is released, i.e.

$$\frac{\partial G}{\partial D} < \frac{\partial R}{\partial D} \tag{22}$$

The stability condition (22) requires that the slope of the R curve is greater than the slope of G curve at the point of their intersection. If the inequality (22) is not satisfied the growth of damage is unstable. In analogy with the fracture mechanics, R curve (20) can be referred to as the damage resistance curve. For the considered model the damage resistance curve can be determined analytically if the rupture strength

distribution is known. The shape of the R and G curves depends on the selected damage variable. Adroit selection of damage variable leads to R and G curves similar in shape to those encountered in fracture mechanics. Using the Weibull distribution of link rupture strengths the expression for the energy release rate G and the damage resistance force R

$$G(F,D)=-\frac{\partial \pi_f}{\partial D}=\frac{F^2}{2(1-D^2)K} \quad \text{and} \quad R(D)=\frac{dE_\gamma}{dD}=\frac{F_m^2}{2K}(\alpha e)^{2/\alpha}\left(\ln\frac{1}{1-D}\right)^{2/\alpha} \tag{23}$$

As the shape parameter α becomes larger the Weibull distribution (tending in the limit to the Dirac delta function) becomes increasingly more typical of the brittle response (ordered solids). The corresponding R curve coincidentally tends to the Heaviside function approaching the Griffith's criterion for homogeneous, perfectly brittle solids.

Tangent Stiffness and System Compliance. If all of the energy used in the rupturing process is transformed into the surface energy, the complementary work W of the externally applied force F is

$$W^*(F)=\int_0^F u(F)dF=W_m^*-F_m u_m\left[1-\frac{F}{F_m}-\frac{2}{3}\left(1-\frac{F}{F_m}\right)^{3/2}\right] \tag{24}$$

where W_m^* is the complementary work at maximum force F_m. The tangent compliance of the system can be derived as the second derivative of the complementary work with respect to the force

$$\frac{1}{K_t}=\frac{d^2W^*}{dF^2}=\frac{u_m}{2F_m}\left(1-\frac{F}{F_m}\right)^{-1/2} \tag{25}$$

At the apex $F = F_m$ of the force-displacement curve the compliance is infinite and the tangent stiffness vanishes. At this point a continuous change in the microstructure (gradual removal of links) results in a qualitative change in the macro response defined as a loss of the ability to sustain further increases in the load. The stiffness of the specimen can be also be considered a transport property. The threshold value defining the critical state at which the transport property disappears is in physics classified as the phase transition. Since the complementary (or Gibbs') free energy (24) is convex in force F, and since the compliance is the second derivative of the complementary energy, the failure of a parallel bar model in force controlled conditions is a paradigm of a second order phase transition. This phase transition is interpreted as a transition in the connectedness. In a load controlled test at the critical point, or percolation threshold, the remaining links will fail in a rapid succession (avalanche or cascade mode) in response to a minute increase in the force F beyond F_m. Physically, the system undergoes a transition from a connected to a disconnected state.

The above sketched discussion of the loose bundle parallel bar model provides a very good illustration of some of the essential aspects the physics of damage processes. However, the simplicity is lost in an attempt to generalize the model by including the effect of stress concentrations. It is interesting that the estimates of the critical state rendered by the hierarchical parallel bar model [7] are in very good agreement with the predictions of the above discussed loose bundle parallel bar model [8]. This provides a first but insufficient indication that the stress concentrations (direct interaction of defects) might not always be significant in the ascending part of the response.

LATTICES

Lattices represent not only a more realistic discretization but also a provide a very natural method of estimates of the stress concentrations. A truly comprehensive study of rupture in triangular central-force lattices, consisting of links with identical stiffness and randomly distributed rupture strengths, was recently completed by Hansen, et al. [9]. At each end the lattice was supplied by a rigid member ensuring identical displacement of all end nodes. Periodicity conditions were enforced in lateral direction to eliminate the end effects. Quenched disorder was introduced assuming uniform distribution of link rupture strengths $p(f_r)$ = const. (modeling the initial damage by links of zero strength). On such a

lattice Hansen, et al. [9] performed repeated computations for a large number of different physical realizations of the same statistics. The only difference between individual simulations consisted of different spatial distribution of links strengths. To ascertain the effect of the lattice size Hansen, et al. [9] considered four different lattice sizes defined by the number of rows in the lattice λ.

Computations were performed using conventional truss analyses. Forces in links were computed for every increment of the externally imposed displacement. Whenever the force in a link exceeded its rupture strength f_r, the link was removed and its force redistributed to extant links in accordance with the equilibrium and compatibility conditions. Since the lattice geometry was periodic, and analysis deterministic, the disorder is attributable solely to the non-deterministic distribution of the initial damage and rupture strengths (quenched disorder).

The macro-variables defining the kinematics of the considered dissipative process are the displacement u of the lattice (change of the distance separating the rigid members) and an appropriately defined damage variable D (2). On the micro-scale the history is recorded by the number of broken links n. Since n, or D, are the only history recording variables, all macro-variables and transport properties (such as the effective lattice stiffness) must be defined as a function of D or as some other appropriate function the number of removed links n. To determine the statistics of the process the results of computations are averaged over the entire ensemble of physical realizations selecting the number n of ruptured links as the control variable.

TABLE 1: Number n_m, density n_m/N of ruptured bonds, displacement u_m, forceF_m and damage D_m at the apex of the force-displacement curve.

λ	4	8	16	24
n_m	9	25 (26)	85 (86)	173 (168)
$D_m=n_m/N$	0.280	0.195	0.166	0.155
u_m	1.09	1.83 (1.91)	3.08 (3.00)	4.17 (4.13)
F_m	0.54	0.92 (0.94)	1.54 (1.56)	2.09 (2.15)
ω_m	0.5 (0.500)	0.5 (0.521)	0.5 (0.487)	0.5 (0.495)

The same lattice was analyzed using the self consistent model in [10]. The analytical results of these analyses are arranged in the Table 1 while the results of the numerical simulations reported in [9] are added in parentheses. The remarkable accuracy with which the self consistent method fits the numerical simulations provides a strong indication that the lattice response during the *hardening* phase of the deformation process (i.e. along the ascending part of the force-displacement curve) depends entirely on the volume averages of the disorder. The exact details of the spatial distribution of ruptured links has a second order effect on the response. The parallel bar model with democratic load sharing rule completely ignores the role and the influence of the stress concentrations on the connectivity threshold. This is a reasonable assumption for the damage tolerant materials, i.e. for deformation processes characterized by the presence of a large number of small crack-like defects. In the case of ordered materials, having a narrow band-width of rupture strengths, the failure occurs by unstable propagation of a single defect at negligible levels of distributed damage. In these cases the stress concentration becomes a dominant effect requiring introduction of a load sharing rule.

The choice of the damage parameter for the parallel bar model is not unique. The damage is fully described by the number of ruptured links n which can be, in principle, selected as the damage parameter. The number of ruptured links can be related to the number of original links $D = (n/N)$, number of surviving links $(n/(N-n))$, etc.. All of these measures are equally valid and a selection of the "best" or "most appropriate" damage parameter is largely a matter of taste. This is not so in the case of lattices. According to the computations in Hansen, et al. [9] both the total number of ruptured bonds n_m and the density of the ruptured bonds (n_m/N) at the apex strongly depend on the specimen size. As such neither of them is a viable candidate for the internal variable. However, the magnitude of the damage variable ω_m (defining the reduction of the secant modulus $\bar{K}(\omega) = K(1-\omega)$) at the apex depends only on the selected distribution of rupture strengths (microstructure). In lattices it becomes necessary to make distinction between the density of ruptured bonds $D = (n/N)$ and the parameter ω. Both of these parameters, as expected, depend on the microstructure (selected distribution of the link rupture strengths $p(f_r)$). However, only the parameter ω, or more accurately the magnitude of the secant modulus $\bar{K}(\omega)$, is

invariant of the lattice size. Since the effective secant modulus $\bar{K}(\omega)$ is readily measurable this conclusion is potentially very important in selection of the internal variable quantifying the damage.

SUMMARY AND CONCLUSIONS

Analyses of damage processes using simple discretized models provides valuable insights into the essential features of the problem. The most important conclusion relates to the selection of the effective secant stiffness as a size independent internal variable (order parameter) which is not only measurable but depends only on the distribution of rupture strengths in the microstructure. Secondly, identification of the rupture in load controlled tests as a phase transition suggests that the threshold itself and all scaling laws are robust with respect to the higher statistical moments of the microstructural disorder. Consequently, the effective continua (mean-field) models should provide reasonably good predictions of the macro response during the entire hardening segment of the load-displacement curve.

ACKNOWLEDGMENT

The authors gratefully acknowledge the financial support in form of a research grant from the U.S. Department of Energy, Office of Basic Energy Research, Division of Engineering and Geosciences which made this work possible.

REFERENCES

1. D. KRAJCINOVIC, "Continuous Damage Mechanics," *Appl. Mech. Rev.* 37, 1-6 (1984).
2. W.D. IWAN, "On a class of Models for the Yielding Behavior of Continuous and Composite Systems," *J. Appl. Mech.* 34, 612-617 (1967).
3. V. LUBARDA, D. SUMARAC and D. KRAJCINOVIC, "Preisach Model and Hysteretic Behavior of Ductile Materials," *Eur. J. of Mechanics A* (in press).
4. D. KRAJCINOVIC and M.A.G. SILVA, "Statistical Aspects of the Continuous Damage Theory," *Int. J. Solids Struct.* 18, 551-562 (1982).
5. D. KRAJCINOVIC, V. LUBARDA and D. SUMARAC, "Fundamental Aspects of Brittle Cooperative Phenomena - Effective Continua Models," *Mech. of Mater.* (in press).
6. J.R. RICE, "Thermodynamics of the Quasi-Static Growth of Griffith Cracks," *J. Mech. Phys. Solids* 26, 61-78 (1978).
7. R.F. SMALLEY, D.L. TURCOTTE and S.A. SOLLA, "A Renormalization Group Approach to the Stick-Slip Behavior of Faults," *J. Geophys. Res.* 90, 1984-1900 (1985).
8. D. KRAJCINOVIC and D. SUMARAC, "Fundamental Aspects of Brittle Cooperative Phenomena - Local Load Sharing Rule," *Mech. of Mater.* (in press).
9. A. HANSEN, S. ROUX and H.J. HERRMANN, "Rupture of Central-Force Lattices," *J. Phys. France* 50, 733-744 (1989).
10. D. KRAJCINOVIC and M. BASISTA, "Rupture of Central-Force Lattices Revisited," *J. Phys. I* 1, 241-245 (1991).

FLUIDIZATION AND SEGREGATION IN BI-DISPERSE SOLID-LIQUID PARTICULATE SYSTEMS

Harri K. Kytömaa, Carl R. Peterson, Frank A. McClintock, Stefano Schiaffino

Department of Mechanical Engineering
Massachusetts Institute of Technology
Cambridge, Massachusetts 02139, U.S.A.

ABSTRACT

Fluidization is investigated as an energy efficient method of removing fines in a machine in which comminution and material transport are integrated features of the design. Two different conditions are explored. In the first, small mono-disperse particles are steadily fluidized within a randomly arranged fixed bed of bigger particles. The results show that the fluidization conditions can be predicted by means of an extension of the general correlations proposed by Richardson and Zaki, and intended for fluidization of mono-disperse particles in confined beds. In the second, a uniformly mixed binary bed of glass spheres is impulsively fluidized. The transient bed behavior is found to be more complex than what can be projected from our understanding of the steady state. The initial upward motion of the packed bed forms an upward moving void which is essential for segregation to occur. These experimental findings can be directly used to integrate an efficient separation process into new crushing machines. Information on the optimization of the machine working conditions can be extracted from the obtained results.

INTRODUCTION

Comminution processes find extensive applications in many different fields: mining engineering, powder technology, and the pharmaceutical industry. There is great potential for energy improvement in these areas, as present comminution processes are highly inefficient [1]. The program of which this is a part, addresses the design of a crushing device in an attempt to improve the efficiency of the entire process. Particle fracture and material transport are integrated features of the machine, the final goal being a periodic removal of the fine particles created by the crushing action, while new coarse material is introduced into the system. The necessary size dependent segregation is obtained through the fluidization of the particle bed. In an attempt to simplify the complexity of the problem and gain basic insight of the dominant phenomena, two simple cases are considered. At first, steady fluidization is studied to explore the interactions of coarse and fines in a fluidized system. Then impulsive fluidization is investigated to understand the mechanisms responsible for particle segregation.

Although the results can be directly related to a jaw-crusher-like machine operating on a vertical wet bed, the fundamental nature of this research provides useful information and insight into other particulate processes.

STEADY FLUIDIZATION OF FINE PARTICLES IN A FIXED BED OF COARSE PARTICLES

Spherical fine particles are steadily fluidized within a fixed vertical bed of spherical coarse particles. Particle diameters are 0.15, 0.2, 0.3 and 0.4 mm for the fine particles, and 2, 3 and 4 mm for the coarse particles. Fines and coarse particles are confined in a test section with rectangular cross section (10 X 40 mm). The working fluid is water at ambient temperature and pressure. The coarse particles are packed to a volume concentration of 55%. This is slightly smaller than the random loose packing of 57% [2], and can be attributed to the presence of the lateral walls which cause the coarse particles to pack less efficiently.

As the liquid mass flow rate is gradually increased up to a constant value, the fine particles steadily expand to a concentration value corresponding to the imposed fluid velocity. The fluid velocity is always kept lower than the incipient fluidization velocity for the coarse particles, which act as a fixed porous medium. The degree of agitation of the fine suspension becomes greater at high mass flow rates, but the interface with the clear liquid above always appears sharp.

The issue of the mobility of the fine particles is fundamental in these experiments. Cumberland and Crawford [3] showed that, when mono-size spheres are arranged in a lattice configuration, there is a certain diameter ratio for a small sphere which can just pass through the pore space. Such a diameter ratio (small/large) is termed the "critical ratio of entrance". For the tightest systematic packing, where coarse particles are arranged in a triangular layer structure, the theoretical ratio of entrance is 0.1548. Soppe [4] indicated that particles with diameter ratios up to 0.15 can percolate through the sediments of a random loose packed bed. To ensure a free movement of the fine particles in the pore space of the coarse bed we observe that a size ratio smaller than 0.1 is required. For diameter ratios bigger than 0.1, the fine particle do not freely percolate, but agglomerate in clusters preventing a homogeneous and continuous fluidization.

The results obtained when the fines are fluidized within the bed of coarse particles are presented in the same manner as used by Richardson and Zaki [5] for fluidization of a single species. The authors found that the logarithm of the liquid superficial velocity J_l scales linearly with the logarithm of the liquid volume fraction, according to the form:

$$\log j_l = n\log(1-v) + \log U_i, \tag{1}$$

where n is the slope of the curve and $\log U_i$ is the intercept on the y-axis corresponding to a value of v equal to zero (infinite bed expansion). Combining these results and some dimensional analysis considerations, they correlated the coefficient n in terms of the Reynolds number Re_∞, based on the settling velocity U_∞ of a particle in an infinite stationary liquid and on the particle diameter, and the ratio between the particle diameter d, and the pipe diameter D. For $1<Re_\infty<200$, range of interest for the particles of the present study, the correlation proposed by Richardson and Zaki is:

$$n = \left(4.45 + 18\frac{d}{D}\right) Re_\infty^{-0.1}. \tag{2}$$

Richardson and Zaki also compared the values of U_i with those for the terminal velocity U_∞, and they arrived at the following empirical correlation:

$$\log U_\infty = \log U_i + \frac{d}{D}, \tag{3}$$

which encompasses wall effects. The difference between U_∞ and U_i is attributed to the velocity gradient created near the wall. This effect becomes important when the size of the particles is comparable to the dimensions of the pipe.

This same framework is now extended to the fluidization conditions within the fixed coarse bed. Fig. 1 shows some of the experimental data, obtained when 0.2 and 0.4 mm particles are fluidized alone and within a bed of coarse particles (3 and 4 mm). For the data in the presence of the coarse bed, the liquid superficial velocity and the fine particle concentration v are defined with respect to the interstitial space of the coarse medium.

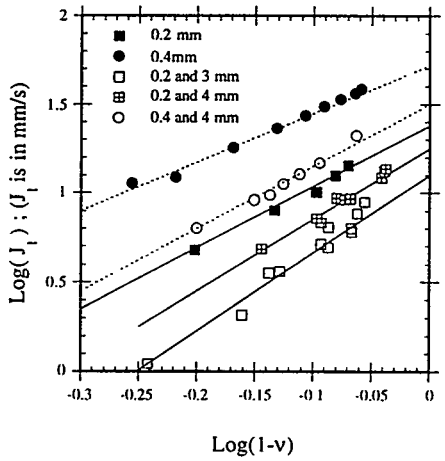

Fig. 1: fluidization of bi-disperse bed. Experimental results

In this representation also the data obtained with the coarse medium fall along straight lines, so that an expression of the type of eq. 1 is a natural choice to correlate the results. Nevertheless, the slope and the y-intercept of these lines are significantly dependent on the size of the fine and the coarse particles. Namely, the y-intercept decreases and the slope of the lines increases, as the particle size ratio (d/d_c) increases. Figs. 2 and 3 show the ratios of the U_i values and of the n parameters over the corresponding values obtained for fine particles fluidized alone (U_∞ and n_0), as a function of the particle size ratio (d/d_c).

In comparing fluidization with and without coarse medium, the principal difference is in the geometry of the fluidized region owing to the presence of the coarse bed. It is therefore proposed that the fluidization parameters U_i and n can be computed with an effective lengthscale that represents the size of the passages formed by the coarse particle bed and its meanderous character. The simplest and most natural choice is the hydraulic diameter derived from the volume and the wetted surface of the coarse pore region. This diameter can be easily related to the coarse concentration v_c and to the coarse particle diameter d_c in the following way:

$$D = \frac{4 x Coarse Pore Volume}{Wet Surface of Coarse Medium} = \frac{2(1 - v_c) d_c}{3 v_c}. \tag{4}$$

When this effective diameter is used, eq. 3 is capable of predicting the values of the correlating parameter U_i, and the related results are plotted with a continuous line in fig. 2. For eq. 2, the introduction of the diameter defined in eq. 4 captures the trend of the

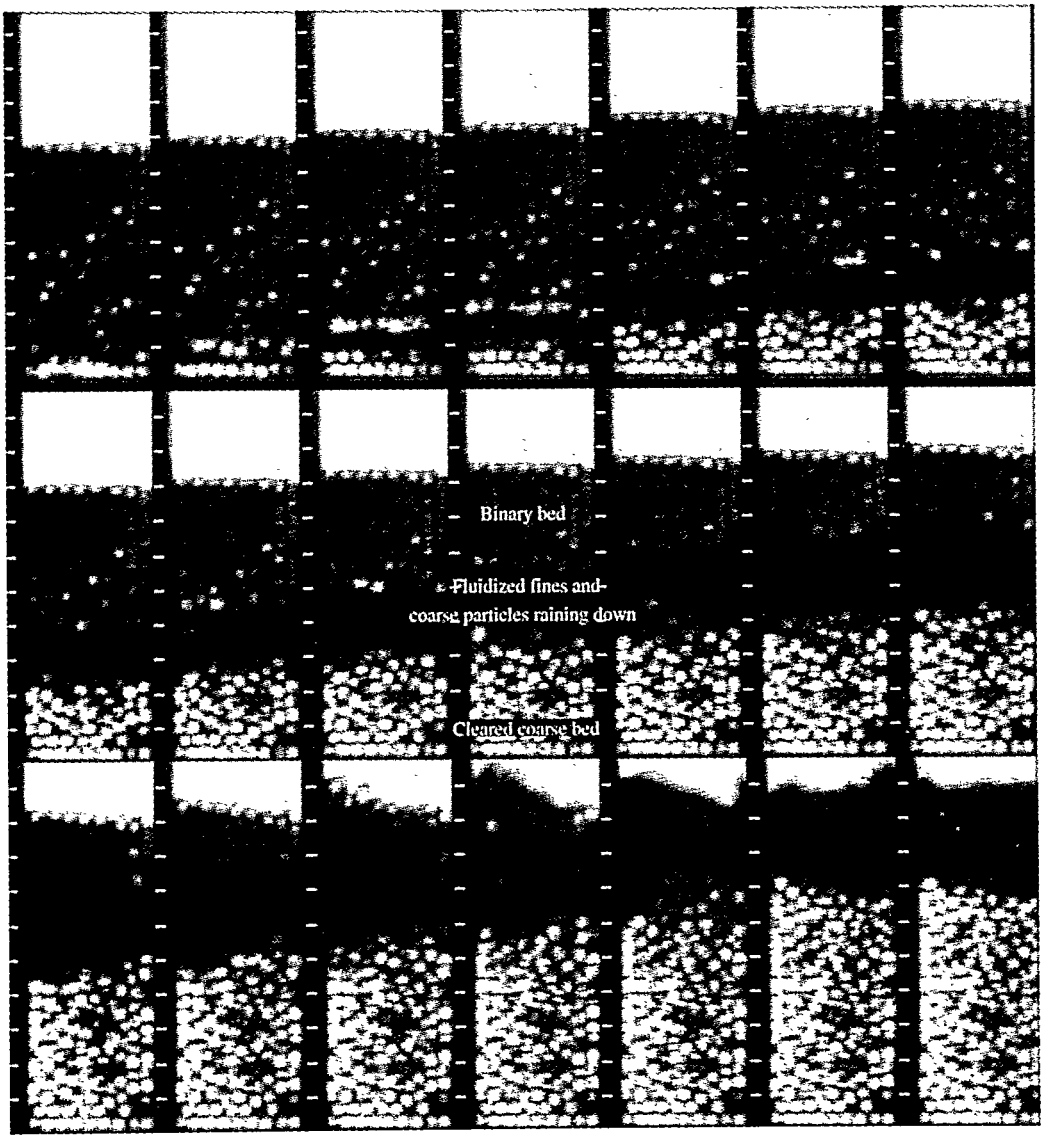

Fig. 4: image sequence of a binary bed impulsively fluidized in a rectangular test section. The fine particles are 0.2 mm black coated glass spheres. The coarse particles are 4 mm transparent glass spheres. Frames are spaced by $1/6^{th}$ of a second. The distance between the white scale markers on the left of each frame is 10 mm. The imposed superficial liquid velocity is 10 mm/s. The bed at first is lifted and the bottom layers of coarse particles start to rain down. An upward moving coarse particle free region is formed. In this region the fines are fluidized. When the binary bed reaches a critical thickness, in this case approximately three coarse particle diameters, an instability occurs, and the fines break through the plug. In the final condition the fines are fluidized on top of the cleared coarse bed.

experimental data, but does not match the values. The same expression is then maintained, but one of the experimental coefficients is modified according to our measurements. The following correlation is proposed:

$$n = (4.45 + 5.74\frac{d}{D}) Re_{\infty}^{-0.1}, \qquad (5)$$

This correlation is plotted in fig. 3. The discussed results represent an extension of the general correlations for vertical straight walled fluidized beds. Despite the complex distribution of the flow across the porous medium, the introduction of the hydraulic diameter for the coarse bed is sufficient to predict the fluidization conditions.

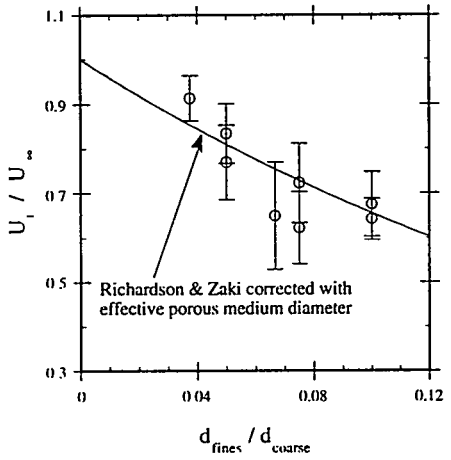

Fig. 2: steady fluidization of bi-disperse bed. Ui correlating parameter.

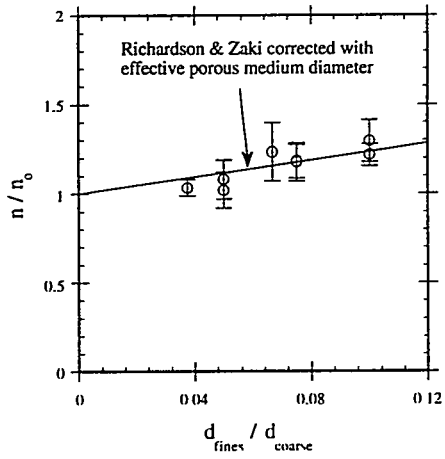

Fig. 3: steady fluidization of bi-disperse bed. n correlating parameter.

IMPULSIVE FLUIDIZATION OF BI-DISPERSE PARTICULATE BEDS

The unsteady nature of these tests adds a level of complexity to the steady case discussed in the previous section. The phenomena observed under impulsive fluidization show features that are significantly different and unexpected on the basis of the understanding of the steady behavior.

The experiments are performed with a uniformly mixed bed of coarse and fine particles. Fines of 0.2 mm with coarse particles of 2, 3 and 4 mm are used. The particles are placed in a rectangular test section, and the fines fill the void of the coarse medium. From rest, an upward liquid flow rate is suddenly increased to a constant value by means of a positive displacement device. Image analysis tools are chosen to extract species concentration and velocity measurements.

Fig. 4 is a sequence of video images spaced by 1/6th of a second which clearly show the details of the events. The fine particles are dark and the coarse are transparent. Upon

injection of the working fluid, the mixture of fines and coarse starts to be dragged upward as a plug and little separation occurs. The lower layers of this plug precipitate due to the fact that the liquid velocity is always smaller than the coarse particle fluidization velocity. The upward motion of the plug is followed by a wave-like progression of a region where segregation occurs between the heavy settling particles and the light particles kept in suspension. The formation of this void is essential for segregation to occur. The net result is the accumulation of a cleared coarse bed at the bottom of the test section while the plug is still being dragged upward. When the depletion of the plug is such that only a few layers of coarse are left, the process reveals the sudden nature of the final separation with the fines breaking through in an apparently unstable manner. In the final conditions the fines are fluidized on top of the coarse bed which is sitting at the bottom of the test section.

Measurements of fine concentration left in the coarse bed after the segregation process show that removal is directly related to the liquid flow rate. Fig. 5 shows the removal fraction (volume of fines segregated per initial volume of fines in the bed) as a function of the liquid superficial velocity J_l. For values of J_l close to the falling terminal velocity of the fines the final separation is almost complete. It is proposed that in these conditions the fine particles released at the lower interface of the plug are kept fully suspended while the coarse are settling. If the liquid velocity is lower than the particle terminal velocity, the fines partially settle and a fraction of them is trapped and entrained again in the coarse layers accumulating at the bottom.

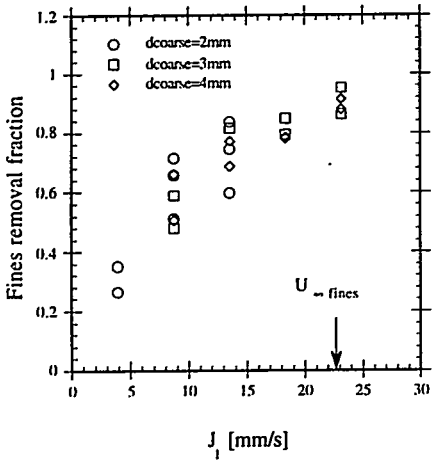

Fig. 5: final removal fraction of fine particles as a result of impulsive fluidization of bi-disperse system.

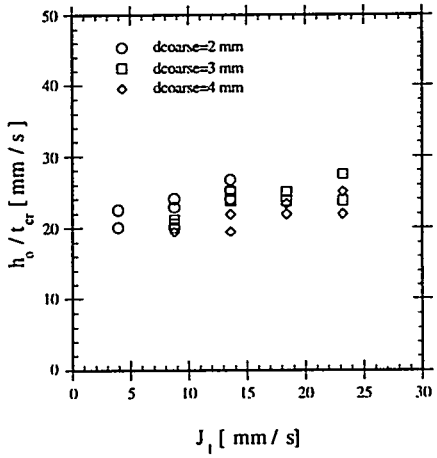

Fig. 6: bed height-segregation time relationship for impulsive fluidization .

In relation to the design of a crushing machine it is desired to achieve a high and fast removal of fines from the coarse bed. The effect of increasing liquid flow rate on the time required to obtain segregation is also considered in our experiments. It is found that the segregation time is essentially proportional to the initial height h_o of the bed. In fig. 6 it is shown that the ratio between the initial bed height and the time required to segregation is constant with J_l. This behavior is explained observing that higher liquid flow rates have the

only effect of raising the plug at a proportionally higher speed. For this reason the depletion velocity relative to the upward moving plug depends on the characteristics of the settling particles and the relative velocity with the fluid, but not on the liquid flow rate as measured in a fixed reference system. In a reference frame traveling with the plug the wave motion associated with the erosion of the bed is seen to progress at a constant speed.

The net result is that high liquid flow rates do enhance particle segregation, but do not significantly alter the speed of the process. For elevated mass flow rates the final segregation occurs with a higher rise of the particle plug. This could be a problem when design considerations require to confine the bed inside the machine.

The final optimization of the machine parameters and working conditions will have to combine these and more specific observations in a unified framework of material transport and fracture analysis.

CONCLUSIONS

Fluidization of binary particle systems is considered in steady and unsteady conditions.

When fine particles are fluidized within a fixed coarse bed, it is shown that the results can be predicted by means of an extension of the general correlations (2) and (3) proposed by Richardson and Zaki, and developed for mono-disperse particles fluidized in vertical pipes. The extension of such general relationships is obtained with the correction of one of the empirical coefficients proposed by Richardson and Zaki, and the introduction of the hydraulic diameter for the pipe. This diameter represents an effective size of the passages formed by the coarse particle bed and can be related to the coarse bed concentration and coarse particle diameter (eq. 4).

In the unsteady conditions, when the bed of fine and coarse particles is impulsively fluidized, it is shown that complete segregation between the two species can be achieved, provided that the liquid velocity is higher than the terminal velocity of the small particles. For lower liquid velocity values, segregation is still obtained but with a partial removal of fine particles. The velocity of the segregation process is independent of the height of the bed or the liquid flow rate.

While these measurements were conducted in simplified conditions, the fundamental nature of the results is of direst interest to a number of particulate processes and machinery.

ACKNOWLEDGMENT

This work was supported and made possible by the U.S. Department of Energy, under grant number DE-FG02-85ERI 13331.

LIST OF SYMBOLS

D:	pipe diameter or the equivalent pipe diameter defined in (4)
d:	fluidized particle diameter
d_c:	coarse particle diameter
h_o:	initial bed height
J_l:	liquid superficial velocity or liquid gross section velocity
n :	experimental coefficient defined in (2)
Re_∞:	Reynolds number based on particle diameter and settling velocity
t_{cr}:	time required to obtain final segregation
U_i :	antilog of the $\log J_l$ intercept axis at $v=0$
U_∞:	terminal or settling velocity of a single particle in an infinite liquid
v :	fluidized particle volume concentration
v_c:	coarse particle volume concentration

REFERENCES

1. Committee on Comminution and Energy Consumption, National Advisory Board, National Academy of Science. Reprint No. NMAB-364, May, 1981.

2. McGeary, R. K. 1961. *Mechanical Packing of Spherical Particles.* J. Am. Ceram. Soc., pp.513-522.

3. Cumberland, D.J. & Crawford, R.J. 1987. *The Packing of Particles.* Elsevier, pp. 45-47 and 59-61.

4. Soppe, W. 1990. *Computer Simulation of Random Packings of Hard Spheres.* Powder Technology, 62, pp.189-196.

5. Richardson, J.F. & Zaki, W.N. 1954. *Sedimentation and Fluidisation.* Trans. Inst.Chem. Engrs., vol.32, pp35-53.

EFFECT OF CARRIER GAS PRESSURE ON CONDENSATION IN A SUPERSONIC NOZZLE

G. Wilemski, B.E. Wyslouzil, M. Gauthier, and M.B. Frish
Physical Sciences Inc.
Andover MA 01810

ABSTRACT

We performed supersonic nozzle experiments with a fixed water or ethanol vapor pressure and varying amounts of nitrogen to test the hypothesis that carrier gas pressure affects the onset of condensation. Such an effect might occur if non-isothermal nucleation were important under conditions of excess carrier gas in the atmospheric pressure range, as has been suggested by Ford and Clement. Although we observed a small increase in the condensation onset temperature as the stagnation pressure was reduced from 3 to 0.5 atm, we cannot attribute these changes to any non-isothermal effects. To theoretically simulate the observed behavior, we performed calculations of nucleation and droplet growth in the nozzle that took into account the change in nozzle shape with carrier gas pressure due to boundary layer effects and the heat capacity of the flowing gas. We neglected energy transfer limitations in calculating the nucleation rates. The trend of the calculated results matched that of the experimental results very well. Thus, heat capacity and boundary layer effects are sufficient to explain the experimental onset behavior without invoking energy transfer limited nucleation. Beyond the onset location, the calculations overpredicted the rate of water condensation. Thus, inefficient cooling of larger, growing droplets may be influencing droplet growth rates. Our conclusions about the rate of nucleation are consistent with those obtained recently using an expansion cloud chamber, but are at odds with results from thermal diffusion cloud chamber measurements.

1. INTRODUCTION

The condensation of rapidly cooled vapor mixtures has been under investigation for over 50 years, and a considerable body of information has been amassed. [1,2] One of the most important concerns is to understand how and why the observed onset of condensation varies with different experimental conditions. The onset of condensation is the point in the expanding flow where the density, pressure, and temperature deviate significantly from the isentropic values. Aside from the enormously difficult theoretical task of predicting the onset of condensation from well-founded physical principles, there remain perplexing differences in onset conditions measured by different investigators that are too large to be accounted for by experimental errors. While some of these differences can surely be explained in terms of the non-equilibrium conditions developed in extremely rapid molecular beam and free jet expansions compared to the much gentler expansions found in Laval nozzles and shock tubes, many experimental results found with these latter devices also show unexplained differences in the onset temperature of condensation. Examples can be readily cited for the condensation of water [3], argon [4], and nitrogen [5].

Our recent experiments explore the effect of carrier gas pressure on the onset of condensation in the atmospheric pressure range. This factor has not been systematically varied before, but it can qualitatively account for a shift in onset temperature with carrier gas pressure. In principle, larger nucleation and growth rates (and higher onset temperatures) are achievable at higher carrier gas pressures because "hot" clusters can be more rapidly thermalized than at low pressures. The latent heat of condensation significantly raises the internal energy of a cluster formed by monomer addition. Until this excess energy is removed via gas-cluster collisions, the cluster is prone to decay by re-emitting a monomer. Barschdorff [3] previously observed a change in onset temperature due to this effect for high mass fractions of condensible vapor. Recently, Ford and Clement [6] suggested that a

similar effect on nucleation rates might be observable under conditions of excess carrier gas at about 1 atm. The experimental evidence on this subject is confusing. In diffusion cloud chamber experiments, Katz et al. found a decrease in nucleation rate of four to five orders of magnitude with increases of carrier gas pressure from 100 to 2000 Torr [7]. An opposite, but smaller, trend was observed in flow diffusion chamber experiments by Anisimov and Vershinin [8,9]. Recently, Wagener, Strey, and Viisanen, [10] using an expansion cloud chamber, reported no intrinsic effect of carrier gas pressure on the nucleation process.

The goal of our current work [11] is to determine if a reduction in carrier gas pressure delays condensation onset to a lower temperature in the nozzle which would be caused by strong non-isothermal nucleation effects. In our experiments, we have not observed a significant variation in the onset of condensation (with a fixed low initial concentration of water or ethanol vapor) accompanying a decrease in the carrier gas pressure. Thus, our results provide evidence that non-isothermal nucleation effects are unimportant for excess carrier gas in the atmospheric pressure range even at the high nucleation rates found in nozzles.

2. EXPERIMENTAL APPARATUS AND DATA ANALYSIS

Our experiments are done with an intermittent, low Mach number, supersonic Laval nozzle that is equipped to do spatially-resolved light scattering and Mach-Zender interferometry [12,13]. The two-dimensional nozzle, with a 0.5 x 1.7 cm^2 throat, is defined by two carefully machined aluminum blocks enclosed between two parallel pyrex glass walls. The 7.27 cm long supersonic portion consists of straight, diverging walls with an exit-to-throat area ratio of 1.36 that yields a maximum Mach number of 1.72 for a perfect diatomic gas. During steady supersonic flow periods of several hundred milliseconds, one-dimensional temperature and pressure gradients are established in the nozzle. Typical cooling rates are about 0.6 K/μs. Temperatures between 225 and 260 K are achieved in the condensation zone downstream of the nozzle throat. Condensible vapor is controllably mixed with the nitrogen carrier gas in a pressurized saturator and fed directly into a large supply plenum. The interferometry data yield a relative density profile in the nozzle. Pressure measurements made in the supply plenum and through a pressure tap at the x=0 cm point in the nozzle fix the absolute value of the density ratio. The deviation from isentropic flow caused by latent heat release, when sufficiently large, can be detected with the interferometer by comparing density ratio profiles obtained under conditions of dry flow to those obtained with condensation. The temperature profile of the expanding/condensing flow is obtained by integrating the diabatic gasdynamics equations using the measured dry and wet density profiles as input data, following a procedure similar to that of Wegener and Pouring [14].

3. EXPERIMENTAL RESULTS and DISCUSSION

Experiments at constant stagnation pressure with varying condensible vapor pressure confirm that our supersonic nozzle results are consistent with those of other workers generated using a variety of experimental techniques. The results for ethanol are shown in Figure 1, where they are compared with those of Wegener, Clumpner, and Wu [15] and those of Dawson et al. [16] Of greater interest are the results unique to the current work, i.e., the results of experiments in which the initial pressure of the condensible species was constant but the pressure of the carrier gas was varied significantly. Figure 2 shows raw wet and dry gas density data measured at total stagnation pressures of 0.5 and 3 atm. One

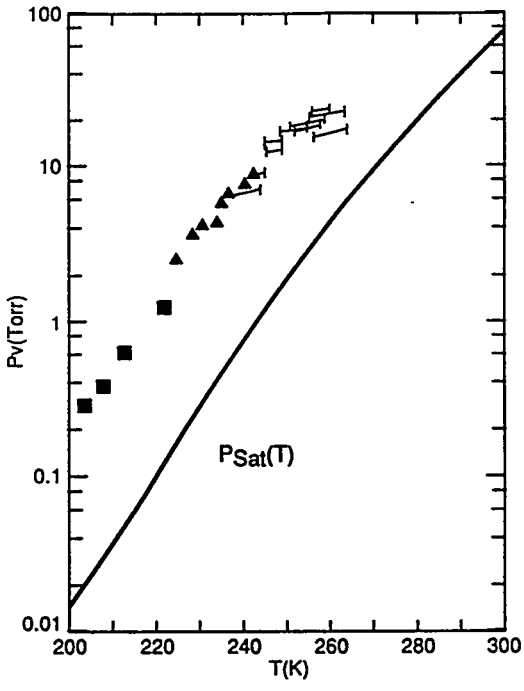

Figure 1. Onset of Ethanol Condensation. ▲, present work; ■, Wegener et al. (Ref. 15). ⊢⊣, Dawson et al. (Ref. 16).

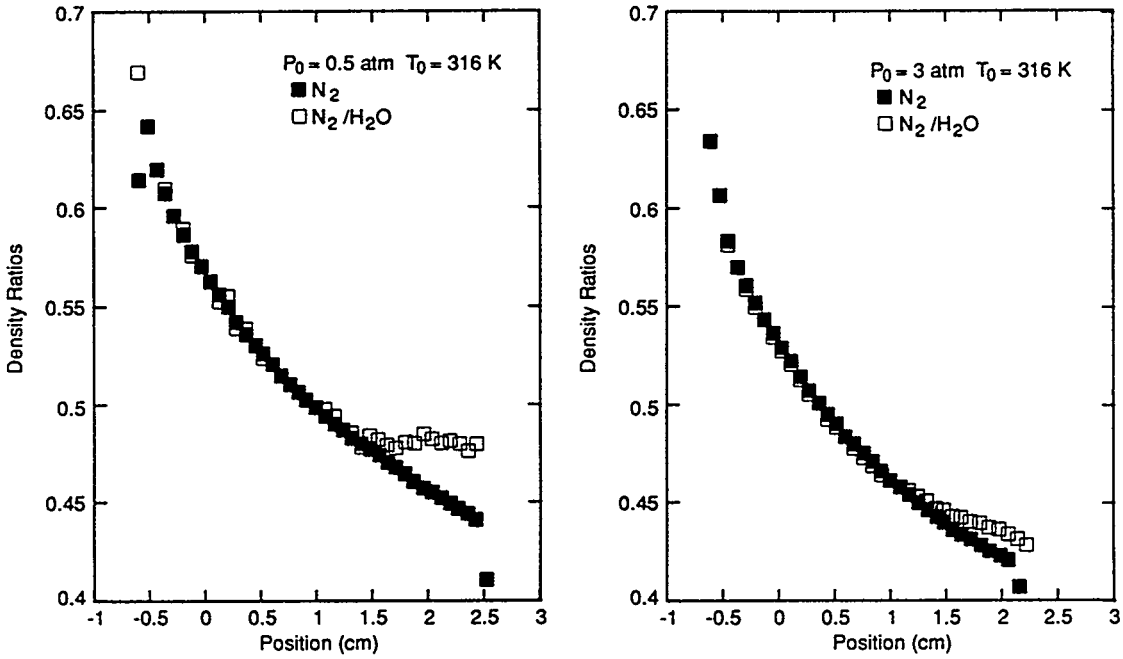

Figure 2. Measured Density Ratios in the Supersonic Expansion of 17.2 Torr Water Vapor at Two Different Carrier Gas Pressures

difficulty in working at low pressure is the poorer quality of the interferograms produced. Despite this it is clear that the location at which the dry and wet curves deviate is not significantly different.

Temperature profiles obtained by integrating the diabatic gasdynamics equations are shown in Figure 3. The vertical displacement of the results is due to the increase in the boundary layer thickness at the nozzle walls with a six-fold decrease in pressure. In effect the nozzle shape changes slightly, giving rise to a gentler expansion at low pressure. In the low pressure case, we also note the stronger departure of the wet temperature profile from the isentrope as well as the higher peak temperature. These are consequences of the reduced heat capacity of the lower pressure gas, since condensation adds roughly the same amount of heat to each flowing gas stream. For the experimental results of Figures 2 and 3, onset occurred between x=1 and 1.5 cm.

Figure 4 shows the experimental onset temperatures versus total stagnation pressure. Theoretical onset temperatures are also plotted. These were calculated using classical isothermal nucleation theory, with the integral method of Oswatitsch [1] and the measured effective area ratios at each pressure as explained in Section 4. Changing the nucleation rate by a factor of ten in the modeling results in a 3 K shift in the onset temperature. Thus large changes (>100X) in the experimental nucleation rate due to changes in carrier gas pressure should be readily observed. Based on the results of Figure 4 we conclude that the small variation in onset temperature is readily explained by classical isothermal nucleation theory and the fluid mechanics of the nozzle flow. Thus, strong non-isothermal nucleation effects are not apparent in our results despite onset pressures that are generally subatmospheric (0.2 to 1 atm). Our recent experimental results for using ethanol as the condensible species show the same trend as in Figure 4.

4. THEORETICAL MODELING OF CONDENSATION

To gain more insight, theoretical calculations of condensation in the nozzle were performed. Two types of models were used: a discrete-sectional (DS) model and

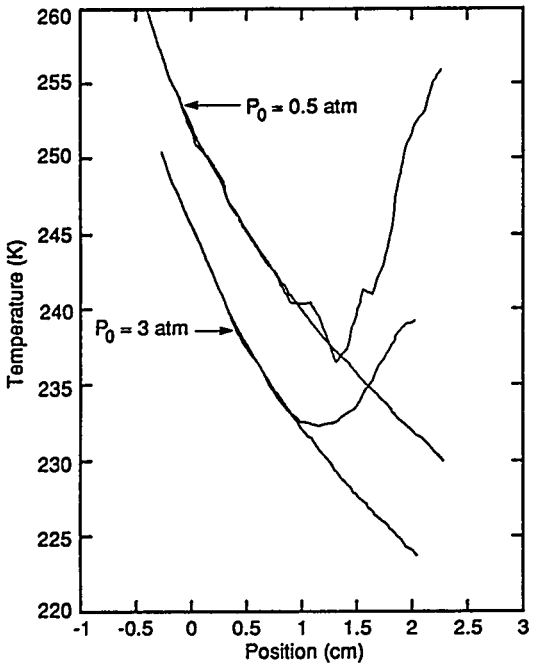

Figure 3. Integrated Dry and Wet Temperature Profiles for Water Condensation Experiments Corresponding to the Measured Density Profiles in Figure 2.

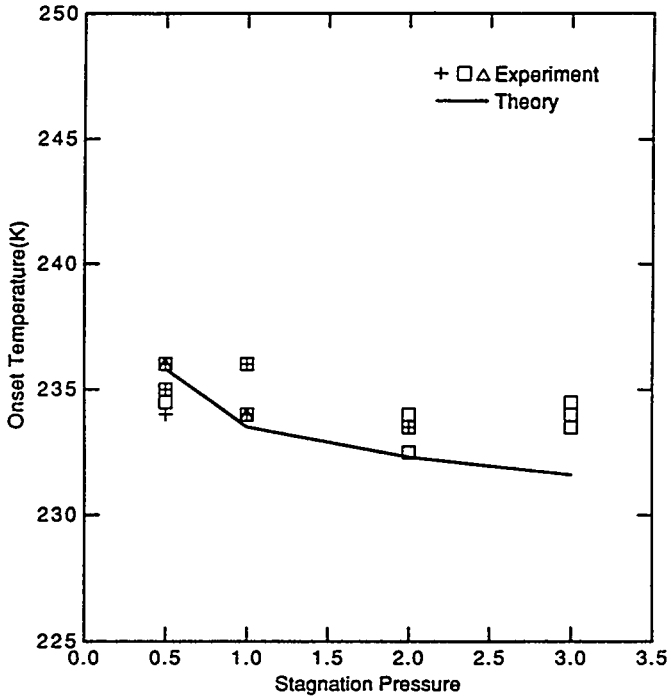

Figure 4. Variation of the Water Condensation Onset Temperature with the Total Stagnation Pressure

an integral steady state (ISS) model first used by Oswatitsch [1]. These models simulate the nucleation and growth of particles containing up to 10^7 molecules (40 to 60 nm radius) and include the effects of heat addition to the flow through the diabatic gasdynamics equations [2]. Both models are based on the classical kinetic model of cluster formation which considers cluster size to change only by monomer condensation and evaporation [17]. The simpler ISS method uses the steady state nucleation rate J to compute the number density ΔN of new particles formed at each point x in the expansion from the conservation law, $\Delta N = (J/u)\Delta x$; u is the local flow velocity. With an appropriate droplet growth law the condensate mass fraction can be calculated versus x, and from this the change in flow properties can be obtained by integrating the diabatic flow equations. This approach has been used extensively for simulating condensation in nozzles [2]. In these calculations, the classical isothermal steady state rate expression, J_{cl}, was used for J. Following conventional practice, a multiplicative adjustment factor Γ was used to bring the calculated and measured values of the onset temperature into agreement. Thus J is expressed as $J=\Gamma J_{cl}$. In general, Γ varies with experimental conditions, but for a given expansion it is a temperature independent constant.

The DS model solves a coupled set of kinetics equations for the rate of change, R_i, in the number density of clusters with i monomers (i-mers), N_i. The rate of change due to monomer addition and subtraction is $R_i=I_{i-1}-I_i$, where $I_i=\beta_i N_1 N_i - E_{i+1}N_{i+1}$. Here β_i is the rate coefficient for adding a monomer to an i-mer, and E_i is the evaporation rate of an i-mer. Standard forms from classical nucleation theory [17] are used for β_i and E_i. The spatial evolution of the cluster densities is governed by steady-state conservation relations that superimpose the effects of the expansion with the above rate processes: $d(N_i/\rho)/dx=R_i/(u\rho)$; ρ is the flow density. This coupled set of first order non-linear rate equations is solved subject to monomer conservation. To keep the problem computationally tractable, only the first 1000 cluster sizes were treated discretely. All of the larger sizes were treated using a binning procedure in which each successive decade was subdivided into n bins, with the bins in each decade ten times larger than the bins in the preceding decade. The principal aim of this exercise was accuracy, not

efficiency. By working in number space and realizing that the cluster size distribution varies linearly over modest increases in cluster size, this approach yields essentially exact results. The results shown here were obtained using 900 bins per decade. The equations were solved using a simple, hybrid implicit predictor-corrector scheme with a fixed step size chosen to give stable results. Given the measured area ratio profile for our nozzle, the local flow temperature, density, and pressure were continuously adjusted by solving the gasdynamics equations for diabatic flow, thereby accounting for heat addition to the flow from condensation.

In Figure 5a the size distributions computed from the DS model show how the droplet distribution evolves from a broad, monotonically decaying function of size at condensation onset into a broad, roughly log-normal distribution of growing droplets accompanied by a molecular vapor consisting mainly of monomers, dimers, and very small i-mers as condensation nears completion. Figure 5b displays the same DS results as a function of particle radius and compares them with ISS model results. The ISS method produces results very close to those of the DS model provided that both the steady state nucleation rate expression and droplet growth law used are consistent with the forms of $ß_i$ and E_i used in the DS model. The ISS model results in Figure 5b. were obtained using the quasi-steady isothermal droplet growth law including evaporation, and droplet growth was started precisely at the critical size. The two particle size distributions at onset, x=-0.2, are in good agreement, with the exact DS results giving a slightly broader distribution. Onset is the point in the nozzle where the effects of condensation are first evident. These theoretical results indicate that at onset most of the condensed mass is already present in very large particles and that substantial droplet growth has already occurred. The latter observations contrast with the conventional view, developed for low temperature ethanol condensation, that at onset most of the condensed mass exists as a cloud of tiny (0.5 nm) near-critical nuclei with droplet growth contributing substantially only after the peak nucleation zone [15].

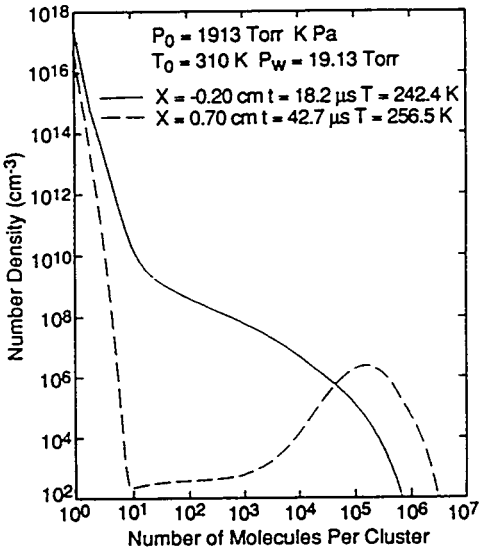

(a) Theoretical water cluster size distributions for water condensation in our supersonic nozzle at the listed water vapor stagnation conditions. The two positions in the nozzle correspond, respectively, to the following percentages of condensed water: 1.7% (onset for this calculation), and 80.4%. The flow time from the throat at x=-0.86 cm is also listed.

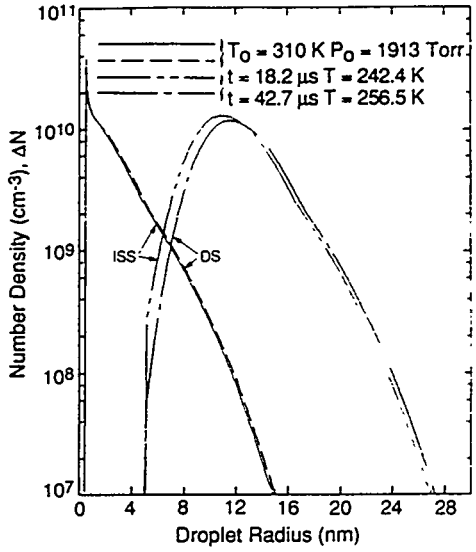

(b) Comparison of particle size distribution calculated using the discrete-sectional (DS) cluster kinetics model and an integral steady state (ISS) model with a quasi-steady isothermal droplet growth law including evaporation.

Figure 5. Calculated Water Cluster Size Distribution

As opposed to the above water results, ethanol condensation calculations for the conditions used by Wegener et al. [15] yield results supporting the picture of decoupled nucleation and growth. These results are shown in Figure 6a. The size distribution at onset is very sharp, critically-sized particles dominate, and most of the mass lies in the smallest sizes. It should be noted this behavior is a consequence of the exceedingly high nucleation rates achieved in the experiemnts of Wegener et al. [15]. In calculations simulating our ethanol condensation experiments, we observe a transition from this decoupled behavior to a regime in which nucleation and droplet growth are equally important as for the case of water condensation. Figure 6a also shows the very broad ethanol size distribution computed for one set of our conditions. Figure 6b compares cumulative mass distribution curves illustrating this transition. The sharpest distribution corresponds to the conditions of Wegener et al.; the other two curves span the temperature range covered by our experiments. We conclude that the magnitude of nucleation rate achievable under different conditions has an major effect on the relative importance of nucleation and droplet growth at onset.

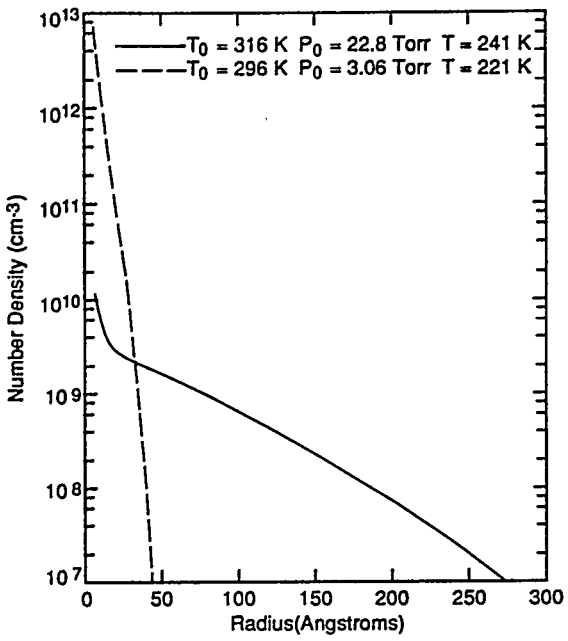

(a) Ethanol droplet size distributions at condensation onset for low temperature conditions used by Wegener et al. (Ref. 15), – – –, and higher temperature conditions of the present work, ——.

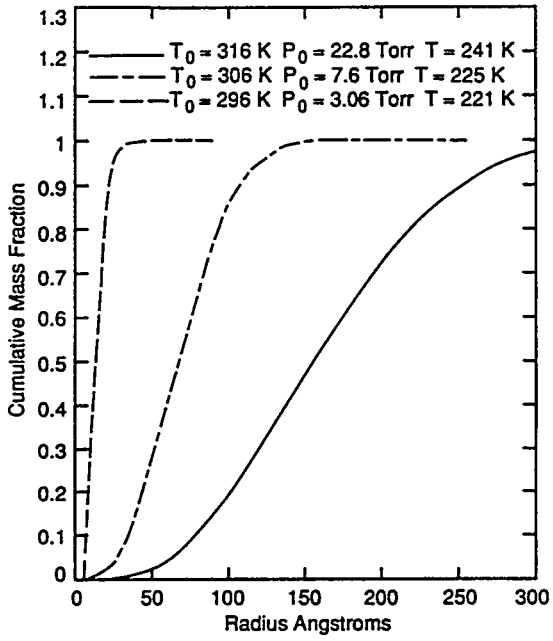

(b) Cumulative mass distributions at condensation onset for low, – – –, intermediate, – – – , and high temperature conditions, ——.

Figure 6. Characteristics of Ethanol Droplet Distributions for Different Condensation Conditions

ACKNOWLEDGMENT

This work was supported by the United States Department of Energy, Division of Engineering and Geosciences, Office of Basic Energy Sciences, under Contract No. DE-AC02-84ER13154 and Grant No. DE-FG02-92ER14257.

REFERENCES

1. K. Oswatitsch, Kondensationserscheinungen in Überschalldusen, *Z. Angew. Math. Mech.*, 22, 1 (1942).

2. P.P. Wegener and B.J.C. Wu, "Gasdynamics and Homogeneous Nucleation," *Adv. Colloid. Interface Sci.* 7, 325 (1977).

3. D. Barschdorff, D., "Carrier Gas Effects on Homogeneous Nucleation of Water Vapor in a Shock Tube," *Phys. Fluids* 18, 529 (1975).

4. J. Steinwandel and T. Buchholz, "Homogeneous Condensation of Argon: An Experimental Study Using the Nozzle Flow of a Cryogenic Ludwieg Tube," *Aerosol Sci. and Tech.* 3, 71 (1984).

5. J. Steinwandel, "Homogeneous Condensation of Nitrogen in the Expansion Wave of a Cryogenic Shock Tube," *Ber. Bunsenges. Phys. Chem.* 89, 481 (1985).

6. I.J. Ford and C.F. Clement, "The Effects of Temperature Fluctuations in Homogeneous Nucleation Theory," *J. Phys. A* 22, 4007 (1989).

7. J.L. Katz, C.-H. Hung, and M. Krasnopoler, The Homogeneous Nucleation of Nonane. In *Atmospheric Aerosols and Nucleation*, Vol. 309 (Lecture Notes in Physics), P.E. Wagner and G. Vali (Eds.), Springer-Verlag, Berlin, 356-359; J. L. Katz, J. A. Fisk, and V. Chakarov, 1992: The Accuracy of Nucleation Theory, *In Nucleation and Atmospheric Aerosols*, N. Fukuta and P. E. Wagner (Eds.), Deepak, Hampton VA, (1988) pp. 11-18.

8. M.P. Anisimov and S.N. Vershinen, *J. Aerosol Sci.* 21, 511 (1990).

9. M.P. Anisimov and S.N. Vershinen, *J. Aerosol Sci.* 21, 515 (1990).

10. P.E. Wagner, R. Strey, and Y. Viisanen, "The Effect of Carrier Gas Pressure on Homogeneous Nucleation Rates in Supersaturated Vapors," *In Nucleation and Atmospheric Aerosols*, N. Fukuta and P. E. Wagner (Eds.), Deepak, Hampton VA, (1992) pp. 27-29.

11. G. Wilemski, B.E. Wyslouzil, M. Gauthier, and M.B. Frish, "Effect of Carrier Gas Pressure on Water Condensation in a Supersonic Nozzle," *In Nucleation and Atmospheric Aerosols*, N. Fukuta and P. E. Wagner (Eds.), Deepak, Hampton VA, (1992) pp. 23-26.

12. M.B. Frish and G. Wilemski, "Optical Studies of Condensation Dynamics in a Supersonic Nozzle," In *Atmospheric Aerosols and Nucleation*, Vol. 309 (Lecture Notes in Physics), P.E. Wagner and G. Vali (Eds.), Springer-Verlag, Berlin, 527-530 (1988).

13. M.B. Frish and G. Wilemski, "Experimental and Theoretical Studies of Condensation Dynamics in a Supersonic Nozzle," In *Proceedings of the Eighth Symposium on Energy Engineering Sciences*, Argonne, IL, May 1990 (NTIS CONF-9005183) (1990) p. 137.

14. P.P. Wegener and A. A. Pouring, "Experiments on Condensation of Water Vapor by Homogeneous Nucleation in Nozzles," *Phys. Fluids* 7, 352 (1964).

15. P.P. Wegener, J.A. Clumpner, and B.J.C. Wu, "Homogeneous Nucleation and Growth of Ethanol Drops in Supersonic Flow," *Phys. Fluids* 15, 1869 (1972).

16. D.B. Dawson, E.J. Willson, P.G. Hill, and K.C. Russell, *J. Chem. Phys.* 51, 5389 (1969).

17. F.F. Abraham, *Homogeneous Nucleation Theory*, Academic, New York (1974).

DEVELOPMENT OF A DUAL-SINKER DENSIMETER FOR HIGH-ACCURACY FLUID P-V-T MEASUREMENTS[1]

Mark O. McLinden and Nolan V. Frederick[2]
Thermophysics Division
National Institute of Standards and Technology
Boulder, Colorado 80303, USA

ABSTRACT

A dual-sinker densimeter to very accurately measure the pressure-volume-temperature (P-V-T) properties of fluids over a temperature range of 80 K to 520 K and at pressures up to 35 MPa is in the final stages of development at NIST. The density of a fluid is determined by measuring the difference in the buoyancy forces experienced by two sinkers of identical mass, surface area, and surface material, but very different volumes. The buoyancy forces on the sinkers are transmitted to a semi-microbalance by means of a magnetic suspension coupling. This paper reviews the principle of the measurement and describes the overall design of the system.

INTRODUCTION

The pressure-volume-temperature (P-V-T) properties of fluids are the key thermophysical property data needed for the development of accurate equations of state required to predict the efficiency of working fluids, to assure equity in the domestic and international trade of chemicals, fuels, and related fluids, and to enable accurate design and efficient control of chemical process equipment. The Thermophysics Division of NIST has extensive experience and capabilities in P-V-T measurements. The existing capabilities need to be upgraded to respond to the increased accuracy demands of custody transfer and model development applications. The need for accurate, but rapidly determined, properties of alternatives to the CFC refrigerants and of other new working fluids dictates a highly automated apparatus.

In view of these needs, we are developing a new apparatus which will complement the existing PVT apparatus, cover wide ranges of temperature, pressure, and density, and, most importantly, extend our accuracy capabilities by nearly an order of magnitude. The wide temperature and pressure capabilities of the new apparatus will be of particular value for the alternative refrigerants, fluids for which low temperature, and also high pressure, data are scarce.

MEASUREMENT PRINCIPLE

The apparatus we are developing is a relatively new type of device for measuring fluid P-V-T properties, termed a dual-sinker densimeter, which has been pioneered by Kleinrahm and Wagner [1]. In this device, two sinkers of identical mass, surface area, and surface material, but very different volumes, are weighed separately with an analytical balance while immersed in a fluid of unknown density. The difference in buoyancy forces on the two sinkers yields the fluid density ρ:

$$\rho = \frac{(\Delta F / g) - \Delta m}{\Delta V}, \tag{1}$$

---

[1]Contribution of the National Institute of Standards and Technology, not subject to copyright.
[2]Rocky Mountain Electron Video, Inc., Boulder, Colorado.

where ΔF is the difference in the net force on the sinkers, g is the local acceleration of gravity, ΔV is the difference in sinker volumes, and Δm is the difference in the masses of the two sinkers (this quantity will be small, but it would be very difficult to fabricate two sinkers of absolutely identical mass). By means of internal electronics and calibration weights, the balance converts the quantity (F/g) to a reading directly in grams, so the local acceleration of gravity need not be known. The sinkers are suspended from the balance via a magnetic suspension coupling which isolates the balance from the high pressure measuring cell. The main advantage of the dual-sinker method is that surface tension effects on the suspension wire, adsorption onto the surface of the sinkers, and other effects which reduce the accuracy of most buoyancy techniques cancel. Because of this cancelling effect, this method is particularly well suited for measurements at saturation. A further advantage of the method is that the measurement yields the fluid density directly, without the need for calibration fluids. The uncertainties in the measured density are expected to vary from 0.01% for liquids ($\rho \approx$ 1 g/cm^3) to approximately 0.1% for low density vapors ($\rho \approx 0.01$ g/cm^3). These accuracies should be routinely achievable over wide ranges of temperature and pressure. The apparatus is most suited for single-phase and saturation measurements on pure components, but will also be suitable for single-phase measurements on mixtures.

The new apparatus is modeled after the Kleinrahm and Wagner device in a very general way, but incorporates a number of changes to yield what we expect will become the new state of the art for wide-range P-V-T measurements. This apparatus will operate at temperatures from 520 K down to 80 K (and as low as 30 K with liquid neon cooling) with pressures up to 35 MPa. The control of the apparatus and the measurement process will be entirely automatic; only the fluid handling operations, such as charging the cell, will be done manually.

EXPERIMENTAL APPARATUS

Overall Layout

The apparatus consists of the following key components:

- the two sinkers which together with a semi-microbalance and a mechanism to pick up each sinker constitute the density measuring system,
- a pressure vessel which contains the fluid of interest,
- a magnetic suspension coupling which transmits the net force on the sinkers from the pressure vessel to the balance,
- pressure and temperature measuring instruments,
- a thermostat system incorporating liquid nitrogen cooling and electrical heating,
- a personal computer which controls the entire system and records the measurement data, and
- auxiliary systems such as fluid charging and vent manifolds and a vacuum system.

The overall layout of the first five of these components is shown in Figure 1. The assembly depicted in this figure is supported on a sturdy aluminum frame which incorporates vibration isolation. An instrument rack, the vacuum system, and a Dewar of liquid nitrogen for the cooling system are adjacent to the main instrument.

Sinkers and Sinker Changing Mechanism

Two well-characterized sinkers constitute the heart of the density measuring system. The prime requirement is that the sinkers be of very different densities. The low density sinker must, of course, be more dense than the densest fluid that will be measured (otherwise it would become a float). These densities must, furthermore, be well known over the full temperature range of interest. The volumes of the sinkers at room temperature can be determined to a few tens of parts per million (0.001 %) by weighing in water [2]. The sinker volumes (or densities) at other temperatures are computed from the thermal expansivity of the material.

Our design employs a low density sinker of single-crystal silicon. The density of silicon (ρ = 2.33 g/cm^3 at 20 °C) is nearly optimal; it is higher than almost all of the fluids of interest (e.g. many of the refrigerants have liquid densities from 1.0 to 1.8 g/cm^3), and only a few fluids (e.g. xenon, bromine) have higher densities. The density and thermal expansion coefficient of single-crystal silicon are known extremely

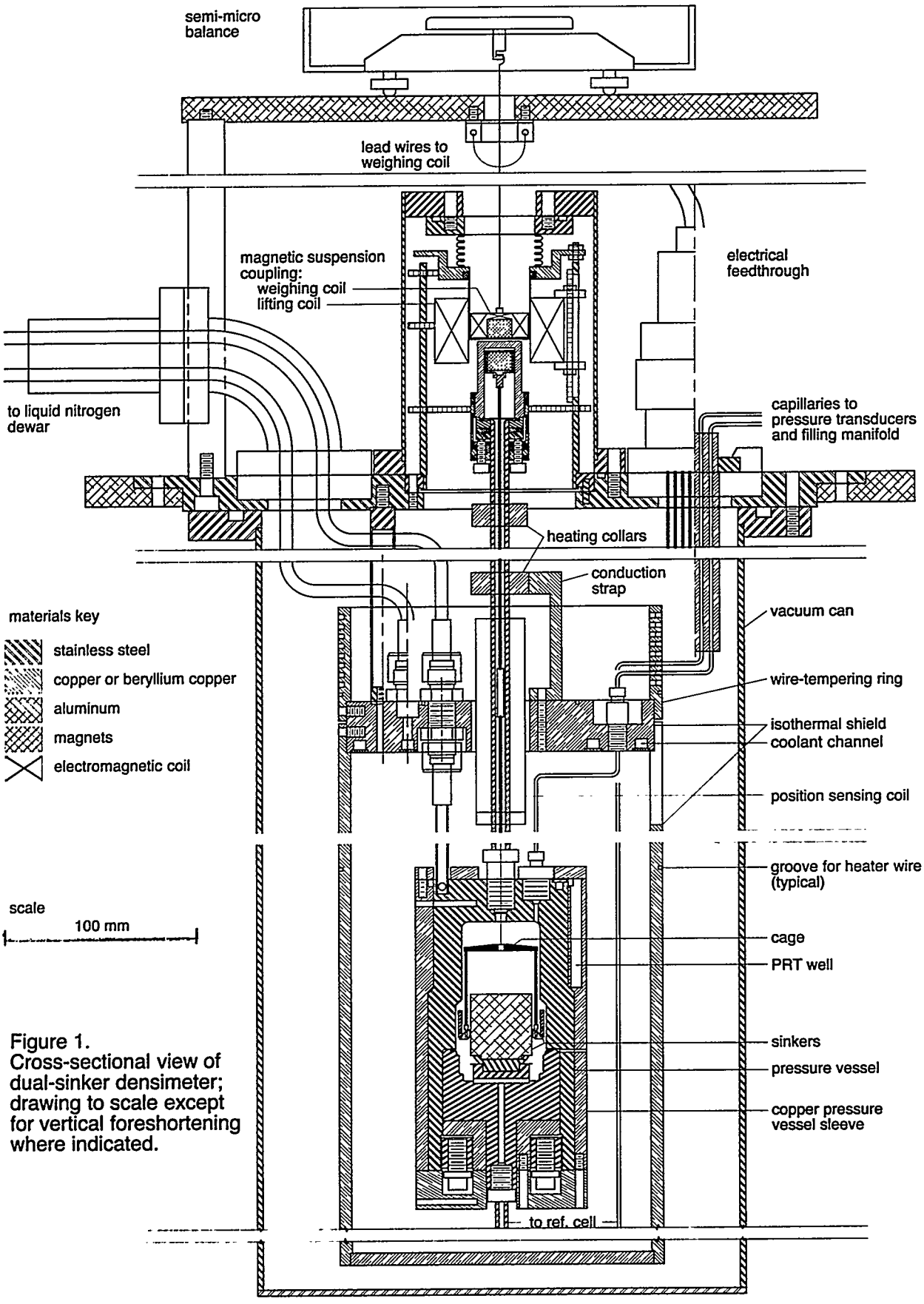

Figure 1.
Cross-sectional view of dual-sinker densimeter; drawing to scale except for vertical foreshortening where indicated.

well [3,4], and since single crystals of ultra-high purity are readily available, the literature values for density and thermal expansion coefficient can be applied to our specimen with negligible loss of accuracy. The silicon sinker is essentially a right circular cylinder; this shape gives close to the minimum surface area-to-volume ratio. The sinker has a diameter of 31.70 mm and an overall height of 33.56 mm. Its nominal mass is 60 g. A small (1.9 mm high by 22.9 mm diameter) protrusion on the bottom of the cylinder serves to center the sinker when it is lowered onto its support pedestal.

The high density sinker is tantalum. Tantalum is a dense metal (ρ = 16.6 g/cm^3 at 20 °C) and is very corrosion resistant. Some of the precious metals, such as platinum and gold, have higher densities but are very soft and present fabrication difficulties, and while they are very corrosion resistant they can catalyze the decomposition of some fluids. In any event, the density of tantalum is high enough to give a large volume difference between the sinkers; there would be little added benefit in using a higher density material. To satisfy the requirement of equal surface areas, the tantalum sinker is in the shape of a ring with an inner diameter of 40.94 mm, outer diameter of 44.20 mm and height of 16.63 mm; its nominal mass is also 60 g. Placing the ring concentric with the silicon sinker achieves at least two benefits: (1) both sinkers are at the same height in the cell, minimizing the effects of any vertical density gradients that might be present in the fluid, and (2) a novel mechanism for picking up and weighing the cylinder and ring is possible, as described below. The volume of the tantalum sinker at room temperature will be determined by hydrostatic weighing. For metals, the coefficient of thermal expansion depends on the heat treatment, exact alloy composition, etc. Fortunately, since the tantalum sinker has a much smaller volume than the silicon sinker, the thermal expansion coefficient of tantalum does not need to be known as accurately as for silicon.

Both sinkers will be coated with the same material to minimize surface adsorption effects. By having the same surface area and surface material for both sinkers, fluid should adsorb equally on the two sinkers, cancelling the effect. We are currently investigating both tantalum and silicon coatings.

To pick up and weigh each sinker, a novel sinker changing mechanism has been developed. The sinkers are picked up by a "cage" consisting of two stainless steel rings connected by three stainless steel posts; the bottom ring contains three small "feet" which can pivot to pick up one sinker or the other. The mechanism and weighing sequence is depicted in a cross-sectional view in Figure 2. In the "reset" position, both sinkers rest on a pedestal. The cage is at its lowest position with the feet pivoted inward by a ledge machined into the bottom of the pressure vessel. The cage is raised (by the magnetic suspension coupling, described below) to

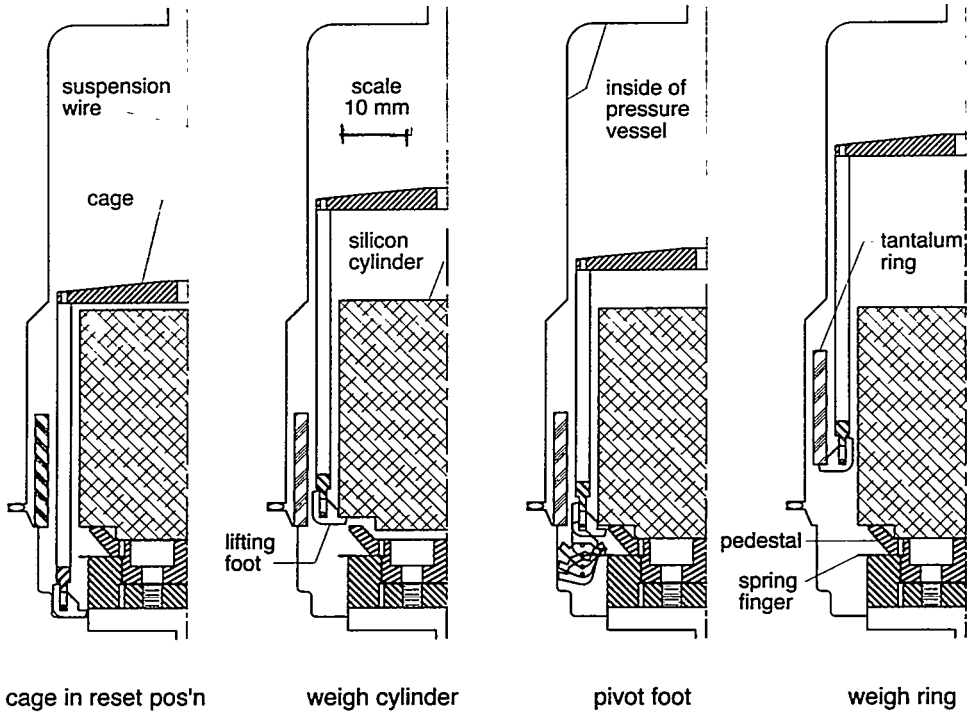

Figure 2. Detail of the sinker changing mechanism showing the four steps in a weighing sequence.

pick up the silicon sinker. As the cage is raised, the feet "pass through" a set of spring "fingers" arranged radially in a rosette pattern. (This finger rosette was produced by photo-etching stainless steel shim stock.) The spring fingers are quite flexible in the upward direction, and the cage feet pass through easily. After the cylinder is weighed, it is lowered back down onto its pedestal; tapered ledges on the pedestal serve to center it. As the cage is lowered further, the feet contact the spring fingers, and the feet pivot outward. This motion is guaranteed by three factors: (1) the feet pivot easily on highly polished axles, (2) the fingers are somewhat more resistant to downward bending than to upward bending, and (3) the center of gravity of a foot lies above the axle with the result that the feet have two stable positions. The process of pivoting the feet, with the feet shown in several intermediate positions, is depicted in the third panel of Figure 2. The cage is again raised, but this time the feet are facing outward and the tantalum ring is picked up for weighing. The cycle is completed when the cage is lowered to the reset position.

Magnetic Suspension Coupling

The magnetic suspension coupling transmits the gravity and buoyancy forces on the sinkers to the balance. The central elements of the coupling are two samarium-cobalt magnets, one on each side of a nonmagnetic pressure separating wall. The top magnet and a small control electromagnet (termed the "weighing coil") are hung from the balance, see Figure 1. The bottom magnet (from which the sinkers hang) is held in stable suspension with respect to the top magnet by means of a feedback control circuit making fine adjustments in the control electromagnet current. All the lifting force during sinker weighings comes from the mutual attraction of the two permanent magnets. Currents in the control electromagnet are very small ($< 1\ \mu A$) and are entirely for control, permitting the use of extremely fine wires as electrical leads to the weighing coil.

A larger electromagnet, not hung from the balance, is used to lift the lower magnet into the range of the weighing coil. This large "lifting coil" is able to lift the cage and sinkers over a fairly large range of vertical positions and makes possible the sinker changing mechanism described above. During sinker weighings, control is switched to the weighing coil, and the current in the lifting electromagnet is zero. A further advantage of a separate lifting coil is that the large (up to 8 A) currents necessary to lift the sinkers from the reset position do not heat the weighing coil. This avoids the destabilizing effect of convection currents rising off a warm weighing coil.

The coupling is located approximately 375 mm above the sinkers. The connection between the bottom magnet of the coupling and the cage consists of several elements. A stainless steel rod 0.76 mm in diameter and 200 mm long rigidly connects the magnet and a ferrite core which moves within the coil of a linear variable differential transformer (LVDT) which provides position information to the feedback circuit. (The ferrite is encased in a short length of thin-walled stainless steel tubing to avoid any possible incompatibilities with the test fluids.) Another length of 0.76 mm diameter stainless steel rod connects the ferrite to a length of fine stainless steel wire at the top of the cage. This fine wire penetrates the liquid-vapor interface when making measurements on saturated-liquid samples; it is very fine (0.10 mm diameter) to minimize surface tension effects. (Wetting of the suspension wire is not necessarily a repeatable phenomenon, and, thus, it is desirable to minimize the absolute effect in addition to the cancelling effect of the two-sinker measuring principle.)

This considerable separation between the coupling and the sinkers is necessary for both the accuracy of the measurement and practical reasons. The ferrite core in the position-sensing coil and the (slightly magnetic) stainless steel pressure vessel must be located away from the magnetic coupling so as not to affect the weighings. It is also desirable to locate the coupling above the main vacuum enclosure to permit easier access. These benefits come at a cost: achieving the precise vertical alignment of the balance, coupling, sinkers, etc., which is critical for the accuracy of the weighings and the operation of the sinker changing mechanism, is a painstaking process. To maintain alignment, all critical elements of the apparatus are attached directly or indirectly to a massive stainless steel plate (381 mm diameter by 18.3 mm thick) attached to a sturdy aluminum frame.

The final element of the magnetic suspension coupling is the pressure-isolating wall. This isolates the balance from the test fluid (which may be at high pressure and/or extremes of temperature). This pressure-isolating wall is a small pressure vessel connected to the main pressure vessel by a length of 9.5 mm O.D. stainless steel tubing. The pressure-isolating wall is located between the two magnets of the magnetic suspension coupling and must, therefore, be made of an absolutely nonmagnetic material. After testing numerous "nonmagnetic" materials, including aluminum, stainless steel, copper, and titanium, we have fabricated this vessel of a beryllium-copper alloy.

Pressure Vessel and Thermostat

The pressure vessel comprising the measuring cell is of a fairly conventional design and is constructed of type 316L stainless steel. The pedestal for the sinkers is in the bottom "lid" of the pressure vessel. The lid is sealed by a copper gasket. A copper sleeve, shrink-fitted to the outside of the stainless steel vessel, serves to reduce temperature gradients to a few millikelvins (thousandths of a kelvin). Four separate openings in the top of the pressure vessel, machined to mate with commercial coned-and-threaded-type high pressure tube fittings, provide access for the suspension wire and fluid filling capillary as well as two spare openings. An opening in the bottom of the vessel will connect with a future "reference cell" described below; it also allows a cleaning solvent to be easily circulated through the vessel.

The primary element of the thermostat system consists of an isothermal shield which surrounds the pressure vessel. The entire assembly will be in vacuum for thermal insulation. The isothermal shield is constructed of copper and is maintained 1 K cooler than the measuring cell by a combination of electrical heating and liquid nitrogen flowing through cooling channels machined into the top plate of the shield. Heat conduction from ambient to the measuring cell is minimized by thermally anchoring all electrical leads, filling capillaries, etc. to the isothermal shield. The small (approximately 20 mW) heat leak from the cell to the shield is offset by electric heat to control the cell temperature to a few millikelvins. A separate liquid nitrogen cooling channel is machined into the top of the pressure vessel; this cooling circuit will be used only for quick cooling between runs and will not be used during actual measurements.

The small pressure vessel which is part of the magnetic suspension coupling will not be cooled because of practical difficulties. It will be maintained at room temperature or about 1 K above the main cell temperature, whichever is higher. A positive temperature gradient between the main cell and coupling is desirable to prevent convection and/or condensation. This temperature gradient is confined to a short length of the tube connecting the main cell and coupling. An upper heating collar is maintained at the temperature of the coupling. A lower collar is maintained at the temperature of the main cell by a combination of electrical heating and copper conduction straps connected to the isothermal shield. It is important to note that in the region of this temperature gradient, the connection between the magnetic coupling and the cage consists of a thin stainless steel rod of uniform diameter. The movement of an object of varying cross section in a temperature (and, thus, density) gradient would affect the buoyancy forces detected by the balance and cause errors in the measured fluid density. For this reason, the position sensing coil, with its ferrite core, is located in an isothermal region maintained at the cell temperature.

A future feature of the apparatus will be a "reference cell" connected to the main measuring cell. For vapor-phase measurements near saturation, the pressure in the measuring cell will be set by the vapor pressure of a small volume of liquid in the reference cell. By independently controlling the temperature of the reference cell, saturated vapor conditions can be closely approached in the measuring cell without gross condensation of fluid onto the sinkers. The effects of the significant surface adsorption which is often unavoidable at conditions very close to saturated vapor are minimized by the equal surface area and surface material of the sinkers.

Instrumentation

The first two elements of the density-measuring system, the sinkers and magnetic suspension coupling, are described above. The other major element consists of a semi-microbalance with a resolution of 10 μg and a stated accuracy of 30 μg over a weighing range of 205 g. An additional feature of this balance which makes it well suited to this apparatus is an automatic calibration mode which can be triggered by a signal from the control computer.

The primary temperature measuring element is a reference-quality, 25 Ω capsule-type platinum resistance thermometer inserted into the copper sleeve of the measuring cell. The resistance of the thermometer is measured in a 4-wire resistance circuit by a dedicated precision voltmeter. Two calibrated standard resistors (10 Ω and 100 Ω) are also measured by the voltmeter. Other temperatures that must be known accurately (such as the temperature of the isothermal shield) are measured relative to the standard PRT by five-junction copper-constantan thermopiles. Two additional thermopiles measure the temperature differences between the top and bottom of the measuring cell and the top and bottom of the isothermal shield; these temperature differences are used to check for approach to equilibrium conditions upon a change in the temperature set point. Several inexpensive 100 Ω PRTs are used to monitor additional temperatures in the system. The thermopiles and 100 Ω PRTs are measured with a nanovolt-level scanner connected to a nanovoltmeter .

Pressures are measured by three vibrating-quartz-crystal pressure transducers having ranges of 0–0.20 MPa, 0–2.8 MPa, and 0–41 MPa. The full range of pressures can be measured within the optimum range of at least one of the transducers. The pressure transducers are located approximately 375 mm above the measuring cell resulting in a fluid head that can be significant under some conditions. To permit accurate correction for this effect, most of the capillary connecting the measuring cell with the transducers is maintained at either ambient temperature or the cell temperature. The temperature gradient between the cell and ambient temperatures is restricted to a horizontal section of the capillary inside the vacuum enclosure; this section does not contribute to the fluid head effect and thus the density gradients resulting from the temperature gradient in this section do not affect the accuracy of the fluid head correction.

The entire system is controlled and all data is collected by a microcomputer. The balance and pressure transducers are read over RS-232 (serial) ports. The interface for the magnetic suspension coupling control circuit is a combination analog/digital I/O board installed in the computer. The remainder of the instrumentation is controlled over an IEEE-488 bus.

Auxiliary Systems

The densimeter also requires several auxiliary systems. A vacuum system consisting of a mechanical roughing pump and high vacuum diffusion pump maintains the insulating vacuum within the thermostat as well as allowing evacuation of the measuring cell. A valve manifold allows charging of test fluids into the measuring cell, connection of one or more of the pressure transducers to the cell, and discharge of samples to the building vent system. A hydraulically actuated, diaphragm-type compressor is connected to the manifold to compress liquid samples up to the maximum working pressure of 35 MPa. The heaters on the isothermal shield, measuring cell, etc. are supplied by 2, 4-channel DC power supplies controlled over the IEEE-488 bus. Finally, a 160 L Dewar of liquid nitrogen supplies the cooling system.

CONCLUDING REMARKS

The apparatus is nearly complete. The various critical elements have been tested individually and are now being integrated and tested as a complete system. The final apparatus may differ slightly from the description given here.

ACKNOWLEDGEMENT

A project of this magnitude can be successful only with the input and accumulated experience of many individuals. We thus acknowledge the advice of, and enlightening conversations with, our colleagues at NIST: W.M. Haynes, G.C. Straty, J.W. Magee, R.A. Perkins, and J. Sandarusi. We express our sincere appreciation for the advice on construction details and skilled fabrication efforts of T. Waldorf and, especially, M. Rybowiak. This work was supported by the Division of Engineering and Geosciences, Office of Basic Energy Sciences, U.S. Department of Energy under contract DE-AI05-88ER13823 and NIST.

REFERENCES

[1] R. Kleinrahm and W. Wagner. Measurement and correlation of the equilibrium liquid and vapour densities and the vapour pressure along the coexistence curve of methane. *J. Chem. Thermodynamics* **18**, 739–760 (1986).

[2] H.A. Bowman, R.M. Schoonover, and M.W. Jones. Procedure for high precision density determinations by hydrostatic weighing. *J. Res. Nat. Bur. Stand.* **71C**, 179–198 (1979).

[3] R.S. Davis. Determination of silicon density to high precision using a submersible, servo-controlled balance. *Metrologia* **18**, 193–201 (1982).

[4] C.A. Swenson. Recommended values for the thermal expansivity of silicon from 0 to 1000 K. *J. Phys. Chem. Ref. Data* **12**, 179–182 (1983).